Diana Filipa Sousa Capela

Hemodynamic Parameters Extraction using Laser Speckle Effect

Dissertation presented to the University of Coimbra in order to complete the necessary requirements to obtain the Master's degree in Biomedical Engineering

September 2014

· U C ·

Universidade de Coimbra

• U C •

FCTUC FACULDADE DE CIÊNCIAS
E TECNOLOGIA
UNIVERSIDADE DE COIMBRA

Diana Filipa Sousa Capela

Hemodynamic Parameters Extraction using Laser Speckle Effect

Thesis presented for University of Coimbra in order to obtain the Master of Science Degree in Biomedical Engineering

Supervisors: Professor Ph.D. João Manuel Rendeiro Cardoso
MSc. Pedro Guilherme da Cunha Leitão Dias Vaz

Examination Committee

Chairperson:	Professor Ph.D. Francisco Gil
Supervisor:	Professor Ph.D. João Manuel Rendeiro Cardoso
Member of the Committee:	Professor Ph.D. Rui Bernardes

Coimbra, September 2014

This work was developed in collaboration with:

Faculty of Sciences and Tecnologies of
University of Coimbra

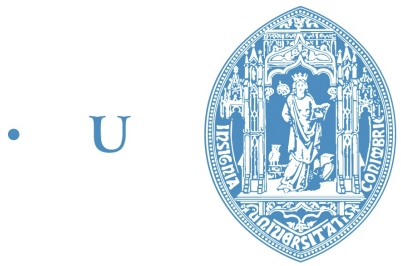

Electronics and Instrumentation Group

"Live as if you were to die tomorrow.
Learn as if you were to live forever."

MAHATMA GANDHI

Agradecimentos

Finalmente posso dizer: "Yes, I can!". Antes de mais devo manisfestar o meu agrado pela minha vida. Não sei ao certo a quem agradecer, todas as pessoas com quem me fui cruzando foram definindo o meu caminho. Mesmo sendo impossível expressar-me como desejaria, passo a agradecer às pessoas a quem consigo identificar o seu apoio, ajuda ou carinho na jornada deste ano:

Ao professor João Cardoso, sendo meu orientador, esteve sempre na vanguarda a direcionar o projeto para que esta investigação se desenvolva da melhor forma.

Aos professores e investigadores do GEI que permitiram a minha integração e fizeram deste local, um espaço agradável e com as condições necessárias para a elaboração da minha tese.

Ao incansável Pedro Vaz, que com a sua calma, dedicação e inteira disponibilidade, volto a frisar, inteira disponibilidade, sempre me apoiou, tirou dúvidas, e não deixou que alguma vez desmotivasse. Acima da amizade que demonstrou, cumpriu o seu papel de co-orientador na perfeição.

Às meninas e companheiras neste barco, foram 5 anos maravilhosos com quem partilhei tanto da minha vida. À Patrícia, a mais recente moradora lá de casa, acompanhou todos os meus passos durante este projeto dando sempre a força necessária. À Carolina, com quem partilhei um dos meus objetivos/sonhos de vida: fazer Erasmus em Itália. À Daniela, a grande companheira de guerra. À Sofia, que transmite sempre a sua serenidade. À Joana, à Mi, à Marta e à Sara que estiveram sempre por perto.

Aos amigos que me viram crescer e me fazem acreditar que sou capaz de tudo o que idealizo e coloco como objetivo na minha vida. Aos escuteirinhos e chefões do 1054 Monte Redondo, a quem dei muito do meu precioso tempo este ano, foram um recurso de força, liberdade, descontração e ânimo para cada semana que se passava.

Ao João, um agradecimento especial pelo apoio, força e motivação que me transmitiu, fazendo-me sentir capaz de tudo e que os limites não existem para mim. Agradeço também toda a sua disponibilidade para me ajudar.

À minha irmã e aos meus familiares, que procuram apoiar-me em tudo o que faço.

Aos pais, aos meus, aos melhores! Pelo amor, entrega e dedicação incansável. Pelos valores que me incutiram. Por abdicarem deles próprios para que eu possa ser quem sou. São a minha fonte incondicional de força e apoio.

O meu sincero obrigado! Diana Capela

Resumo

As doenças cardiovasculares são um flagelo em todo o mundo. Em Portugal, são a causa de morte de cerca de um terço da população. Havendo a necessidade de criar um método simples, rápido e fiável, capaz de monitorizar a micro e macrocirculação, foram desenvolvidas duas técnicas baseadas em imagens laser *speckle* (LSI) para a extração de parâmetros hemodinâmicos. A técnica de LSI tem a capacidade de adquirir imagens bidimensionais em tempo real. Na macrocirculação, foram adquiridas imagens de speckle de um fantoma que consiste em duas membranas de silicone, uma delas reproduz um movimento longitudinal em relação à outra. Os movimentos longitudinais pequenos são difíceis de identificar e segmentar. Para identificar as zonas em movimento foi calculada a entropia regional (RE) das imagens speckle. Estas foram segmentadas pela aplicação de um 'threshold' binrio fixo. O método mais apropriado aplica uma janela de 27 x 27 pixels. O melhor 'threshold' para a segmentação das imagens foi de 2.95. Os resultados obtidos foram muito satisfatórios, uma vez que se obteve uma precisão de 97% e um índice de MCC de 0.91 na validação do método. Este método foi aplicado em testes *in vivo*. Para a extração do valor de frequência cardíaca foi aplicado um filtro ao sinal obtido. A frequência cardíaca foi facilmente adquirida e os resultados foram muito próximos do esperado. Na microcirculação pretende-se obter a perfusão sanguínea a diferentes profundidades, para isso foram obtidas imagens de speckle de um fantoma de acrlico que mimetiza a passagem do sangue num vaso sanguíneo. Durante as aquisições foram usados um laser verde, um laser vermelho e um na região do infravermelho. Às imagens de speckle foram aplicados três métodos para obter o contraste (C) das imagens, um espacial (sLSCI), um temporal (tLSCI) e um espaciotemporal (stLSCI). Foram testados multiplos tempos de exposição (T) e diversas velocidades (V) de forma a obter a perfusão sanguínea. Os melhores resultados foram obtidos quando foi aplicado o método tLSCI. O laser verde apresentou um comportamento mais estável. Os resultados demonstram que quando T ou V aumentam, C diminui. Apesar de ser um método promissor, é incapaz de discriminar as diversas camadas numa única aquisição, para além disso a velocidade calculada é uma medida relativa e não um valor absoluto.

Abstract

The cardiovascular diseases are a serious issue worldwide. In Portugal, they are the cause of death of approximately one third of the population. Having the necessity to create a simple, quick and feasible method for micro and macrocirculation monitorization, two techniques based on laser images were developed, in order to extract hemodynamics parameters. The laser speckle imaging (LSI) has the ability to acquire images in real-time. In the macrocirculation, speckle images were acquired of a phantom which consists in two silicon membranes, one of which reproduces a longitudinal moving in relation of the other. The small longitudinal movements are difficult to identify and to segment. In order to identify the moving regions it was computed the regional entropy (RE) of speckle images. They were segmented by a threshold application. The most appropriate method to apply a windows size of 27 x 27 pixels. The best threshold for images segmentation was 2.95. The obtained results were very satisfactory, since an accuracy of 97% and a MCC index of 0.91 were acquired in validation method. This method was applied in *in vivo* tests. In order to extract the heart rate (HR), it was applied a filter in the obtained signal. The HR was easily obtained and the results were very close to the expected. In the microcirculation, it is intended to obtain the blood perfusion at different depths. For this purpose, the speckle images of the phantom were obtained. It is an acrylic phantom which mimics the blood passage in a blood vessel. During acquisitions, a green laser, a red laser and a infra-red laser were tested. In the speckle images were applied three methods to compute the contrast speckle (C): a spacial (sLSCI), a temporal (tLSCI) and a spatiotemporal (stLSCI) method. Multiple exposure time (T) and different velocities (V) were tested to obtain the blood perfusion. The best results were obtained when the tLSCI is applied. The green laser presents a behaviour more stable. The results prove than when T or V increase, the C decreases. Despite being a promising method, it is not able to discriminate the several layers in a single acquisition. Furthermore, the computed velocity is a relative measure and not an absolute value.

Contents

List of Tables **xvii**

List of Figures **xix**

List of Acronyms **xxi**

List of Symbols and Physics Constants **xxiii**

1 Introduction **1**
1.1 Motivation . . . 1
1.2 Goals . . . 2
1.3 Previous Work . . . 2
1.4 Main Project Team . . . 2
1.5 Thesis Structure . . . 3
1.6 Scientific Contributions . . . 3

2 Physiological Background **5**
2.1 Circulatory system . . . 5
2.2 Physical properties of the blood and hemodynamics . . . 6
2.3 Macrocirculation . . . 8
2.4 Microcirculation . . . 8
2.4.1 Capillaries . . . 9
2.4.2 Cutaneous microcirculation . . . 9
2.4.3 Microcirculation diseases . . . 11

3 State of the Art **13**
3.1 Optical Properties of the Tissue . . . 13
3.2 Cutaneous Macrocirculation Monitoring . . . 14
3.3 Cutaneous Microcirculation Monitoring . . . 14
3.4 Laser Doppler Flowmetry and Laser Doppler Imaging . . . 15
3.4.1 Advantages and Drawbacks . . . 16
3.4.2 Applications . . . 16
3.4.3 Commercial Devices . . . 17
3.5 OPS and SDF imaging . . . 17
3.6 Laser Speckle Contrast Imaging . . . 18
3.6.1 Historical Background . . . 19
3.6.2 Theoretical Background . . . 20
3.6.3 Practical Concepts . . . 23
3.6.4 Different Methods of Laser Speckle Contrast Imaging . . . 24

3.6.5 Advantages and Drawbacks . . . 26
3.6.6 Applications . . . 27

4 Prototype and Bench Tests **29**
4.1 Prototype Assembly . . . 29
4.1.1 Hardware . . . 29
4.1.2 Software . . . 32
4.2 Macrocirculation Set-up . . . 33
4.2.1 Bench Test . . . 33
4.2.2 *In vivo* . . . 35
4.3 Microcirculation Set-up . . . 36
4.3.1 Phantom Device . . . 36
4.3.2 Bench Assembly . . . 37

5 Data Processing **41**
5.1 Macrocirculation Data Processing . . . 41
5.1.1 Segmentation Algorithm . . . 41
5.1.2 *In vivo* Improvement . . . 45
5.2 Microcirculation Data Processing . . . 45
5.2.1 Video Segmentation . . . 46
5.2.2 Speckle Contrast Algorithms . . . 47

6 Results and Discussion **49**
6.1 Macrocirculation . . . 49
6.1.1 Bench Tests Results . . . 49
6.1.2 *In vivo* . . . 54
6.2 Microcirculation . . . 56

7 Conclusions **65**

Appendices **69**

A Microcirculation Test #3 **71**

B Microcirculation Test #4 **73**

Bibliography **85**

List of Tables

1.1 Project team members 3

4.1 Optical table and electrical properties of the lasers. 31

6.1 Results of the AUC of the 4 entropy computation methods. 51
6.2 Results of data-set validation for windows size 27 x 27 pixels and the threshold of 2.95. 53
6.3 Theoretical and obtained results of Heart Rate (HR). 55

List of Figures

2.1 Profile of key parameters along the cardiovascular system. 7
2.2 Capillary flow regulation. 9
2.3 Representation of the skin micro-anatomy. 10
2.4 Mortality due to diabetes. 11

3.1 A typical laser speckle pattern. 18
3.2 Single-exposure speckle photograph. 19
3.3 Set-up scheme of laser speckle imaging. 21
3.4 Theoretical relationship between speckle contrast and τ_c/T. 22
3.5 Schematic of the light flux in the tissue. 23
3.6 Schematic diagrams of LSCI methods. 25

4.1 Video camera Pixelink PL-B741EU. 30
4.2 Laser lights used in bench assembly. 31
4.3 Laser and beam expander. 32
4.4 Flow chart of the acquisition process. 33
4.5 Schematic diagram of the bench test set-up for macrocirculation. 34
4.6 *In vivo* tests 35
4.7 Acrylic phantom. 36
4.8 Bench assembly for microcirculation assessment. 37
4.9 Syringe Pump. 38

5.1 Block diagram of speckle segmentation algorithm. 42
5.2 Algorithm applied in tests *in vivo* for longitudinal motion. 45
5.3 Video segmentation process. 46
5.4 Scheme of script development for algorithms application. 47

6.1 Speckle images of the double membrane phantom. 50
6.2 Pre-procesing of the speckle images of the double membrane phantom. 51
6.3 Binary images of the scene. 52
6.4 ROC curves for best method identification. 53
6.5 Best threshold identification. 54
6.6 Signal and FT of the 3^{nd} *in-vivo* trial of the Subject #2. 55
6.7 Graphic results of microcirculation Test #3, C *vs* T. 57
6.8 Graphic results of microcirculation, Test #3, C *vs* V. 58
6.9 Graphic results of microcirculation Test #4, C *vs* T. 59
6.10 Graphic results of microcirculation Test #4, C *vs* T. 60
6.11 Graphic results of microcirculation Test #4, C *vs* V. 61
6.12 Graphic results of microcirculation Test #4, C *vs* T. 62

6.13 Graphic results of microcirculation Test #5, *C vs T*. 63

A.1 Microcirculation Test #3, *K vs T*. 71
A.2 Microcirculation Test #3, *K vs V*. 72

B.1 Microcirculation Test #4, *K* vs *T*. sLSCI method, 3 x 3 pixels. 73
B.2 Microcirculation Test #4, *K* vs *V*. sLSCI method, 3 x 3 pixels. 74
B.3 Microcirculation Test #4, *K* vs *T*. sLSCI method, 5 x 5 pixels. 75
B.4 Microcirculation Test #4, *K* vs *V*. sLSCI method, 5 x 5 pixels. 76
B.5 Microcirculation Test #4, *K* vs *T*. tLSCI method, 3 x 3 pixels. 77
B.6 Microcirculation Test #4, *K* vs *V*. tLSCI method, 3 x 3 pixels. 78
B.7 Microcirculation Test #4, *K* vs *T*. tLSCI method, 5 x 5 pixels. 79
B.8 Microcirculation Test #4, *K* vs *V*. tLSCI method, 5 x 5 pixels. 80
B.9 Microcirculation Test #4, *K* vs *T*. stLSCI method, 3 x 3 x 3 pixels. . . 81
B.10 Microcirculation Test #4, *K* vs *V*. stLSCI method, 3 x 3 x 3 pixels. . . 82
B.11 Microcirculation Test #4, *K* vs *T*. stLSCI method, 5 x 5 x 5 pixels. . . 83
B.12 Microcirculation Test #4, *K* vs *V*. stLSCI method, 5 x 5 x5 pixels. . . 84

List of Acronyms

$2D$	Two dimensions
$3D$	Three dimensions
A.U.	Arbitrary Units
AC	Accuracy
AUC	Area Under the ROC Curve
$AVAs$	Arteriovenous Anastomoses
bpm	Beats per Minute
CBF	Cerebral Blood Flow
CCD	Charge-Coupled Device
$CMOS$	Complementary Metal-Oxide Semi-conductor
FFT	Fast Fourier Transform
FT	Fourier Transform
FN	False-Negative
FP	False-Positive
fps	Fames per Second
HR	Heart Rate
HVS	High Voltage Source
IR	Infra-red
$LASCA$	Laser Speckle Contrast Analysis
$LASER$	Light Amplification by Stimulated Emission of Radiation
LD	Laser Doppler
LDF	Laser Doppler Flowmetry
LDI	Laser Doppler Imaging
LED	Light Emitting Diode
LS	Laser Speckle
$LSCI$	Laser Speckle Contrast Imaging
$LSFG$	Laser Speckle Flowgraphy
LSI	Laser Speckle Imaging
MCC	Matthews Correlation Coefficient
MPE	Maximum Permissible Exposure
$NIRS$	Near IR Spectroscopy
NPV	Negative Predictive Value
OPS	Orthogonal Polarization Spectral
$PAOD$	Peripheral Arterial Occlusive Disease
PPV	Positive Predictive Value
PZA	Piezoelectric Actuator
RE	Regional Entropy

RGB	Red Green Blue
ROC	Receiver Operating Characteristic
SDF	Side-stream Dark Field
SE	Sensibility
$sLSCI$	Spatial LSCI
SP	Specificity
$stLSCI$	Spatiotemporal LSCI
$tLSCI$	Temporal LSCI
TN	True-Negative
TP	True-Positive
USB	Universal Serial Bus
UV	Ultraviolet
VSG	Voltage Signal Generator

List of Symbols and Physical Constants

%	percent
α	angle
β	optical normalization coefficient
η	viscosity coefficient of the fluid
λ	wavelength
$\langle I \rangle$	mean intensity
Φ	blood flow
π	pi
σ	standard deviation of the intensity
τ_c	decorrelation time
ΔP	pressure variation
C	speckle contrast
C_{bin}	intensities distribution
C_{max}	maximum contrast
D	diameter of the entrance pupil
d	diameter of the speckle
$f\#$	F-number
i, j	position of the pixel in the frame
l	length of the vessel
M	magnification of the image system
P_{bin}	probabilities distribution
r	diameter of the vessel
T	exposure time
t	frame number
v_c	decorrelation velocity
V_{max}	maximum velocity
V_{pp}	peak-to-peak voltage
w	window size

Chapter 1

Introduction

The first chapter of this master thesis intends to present the motivation for the development of this work as well as its goals. It is also presented the team project colleagues and the previous work that contributed for the development of this project. At the end, the thesis structure and the published papers are presented.

1.1 Motivation

It is estimated that, in 2020, cardiovascular diseases will be the leading cause of death worldwide. In Europe, Portugal is the country with the higher rate of deaths due to cardiovascular diseases (23000 deaths per year). This can be easily justified by bad health habits. The majority of Portuguese are sedentary, 70 % has elevated cholesterol levels, 40 % has hypertension, 20 % are smokers and the diabetic population increases every day.[1]

Looking for this scourge, the research team of the Grupo de Electrónica e Instrumentação (GEI) has been developing techniques which allow an evaluation of the circulation changes at an early stage of cardiaovascular disease. The macro and microcirculation monitorizations provide useful information in the diagnosis and prevention of peripheral microvascular diseases and cardiac problems that arise and get worse with ageing.

These facts are the motivation for the development of methods that assess the macro and microcirculation, noting the need for non-invasive, reliable, simple, cheap and quick. For this purpose, it was thought to use laser speckle imaging (LSI) techniques for compute cardiac parameters.

1.2 Goals

Regarding the motivation, the main goal is to developed a methodology that allows the hemodinamic parameters extraction in macro and microcirculation. For this purpose, it was used techniques based on the laser speckle effect. Laser speckle images are obtained by the detection of the reflected photons in a surface. Thus, it is necessary an optical configuration of the necessary elements to acquire the speckle images pattern.

For the macrocirculation assessment, it is intended to achieve the subject heart rate. Before that, it is necessary perform bench tests using a phantom device which reproduces the longitudinal movement, characteristic of the distension of the blood vessels during the cycles of blood pulsation. The speckle images obtained must be processed in order to be segmented. The *in-vivo* acquisitions, the speckle images formed in the pulse, will be segmented according the best parameters defined in the bench tests, then an arterial pulse waveform will be extracted and the frequency of the signal, the heart rate, will be achieved.

For microcirculation assessment, it is necessary to obtain the blood perfusion in several depths, using several light wavelengths. For this purpose, it is need to use a phantom device which reproduces the blood transversal movement, as occurs in the microcirculation. Then it is intended to apply algorithms in order to obtain the speckle contrast. This will give important information about the particles moving. The velocity of them, may be achieve using a few calculus and approximations.

1.3 Previous Work

For the project performance it was necessary to refer to previous work developed in the GEI. The previous work developed by MSc Pedro Vaz was the base of this project performance.[2] The work developed by PhD Edite Figueiras was crucial in microcirculation, where was used the phantom device developed by her.[3] Furthermore, about macrocirculation, Tânia Pereira gave the theoretical necessary support.[4]

1.4 Main Project Team

The project team members are presented in the Table 1.1.

Table 1.1: Project team members

Team member	Area of research	Institution
PhD Professor Carlos Correia PhD Professor Luís Requicha PhD Professor João Cardoso	Scientific and technical supervisors	GEI-UC
PhD student Catarina Pereira PhD student Tânia Pereira PhD student Pedro Vaz MSc student Diana Capela MSc student Pâmela Borges	Hemodynamic parameters	GEI-UC
PhD Edite Figueiras	Hemodynamic parameters	Tampere University of Technologies

1.5 Thesis Structure

This thesis is composed by seven chapters. Chapter 2 presents the physiological background of the blood properties and of the macro and microcirculation. The state-of-the-art of the cutaneous macrocirculation and microcirculation monitoring is showed in Chapter 3. In the Chapter 4 it is presented the prototype assembly and macro and microcirculation set-ups. The algorithms for data processing are described in the Chapter 5. The results are showed and discussed in Chapter 6. Lastly, in Chapter 7 the conclusions are presented as well as the future work of this research.

1.6 Scientific Contributions

VAZ P., **CAPELA D.**, PEREIRA T., CORREIA C., REQUICHA FERREIRA L.F., HUMEAU-HEURTIER A., CARDOSO J., Use of laser speckle and entropy computation to segment images of diffuse objects with longitudinal motion. II International Conference on Applications of Optics and Photonics, 26-30 May, 2014, Aveiro (Portugal). Second place award of best student paper presentation.

Chapter 2

Physiological Background

In this chapter a brief approach about macro and microcirculation is made, as well as the blood physical properties and its hemodinamic.

2.1 Circulatory system

The role of the circulatory system is to maintain an appropriate environment in all the tissues, in order to provide optimal conditions for correct operation and survival of the cells.[5,6]

The circulation is responsible to carry blood all over the tissues of the body. The blood is the most important body fluid: it carries nutrients, gases and many molecules; it removes products produced by metabolism; it participates in homeostatic mechanisms, as a body temperature regulator, fluids maintenance, oxygen and nutrients delivery in several physiological states and; it prevents bleeding by blood clots formation.[5,7]

Blood vessels are organized into two closed circuits - systemic circulation and pulmonary circulation. Each circuit receives the blood, pumped by the heart. The left side of the heart pumps the blood for the systemic circulation (containing about 85% of the blood) and the right side pumps the blood for pulmonary circulation (containing about 10% of the blood). The remaining blood (5%) is contained in the heart chambers.[6,8]

Pulmonary circulation carries deoxygenated blood from the right ventricle to the alveolus where the blood expels the carbon dioxide to the air sacs and receives the oxygen.[8] In the systemic circulation the oxygenated blood is ejected into the aorta and flows through the systemic arteries. The aorta branches progressively into smaller

blood vessels up to the capillaries. When the blood reaches the capillaries, the gas exchange occurs, followed by nutrients delivery. After this process, the deoxygenated blood return to the heart through the vena cava. Prior to the vena cava, the blood flows into the venules and veins, with progressively larger diameters.[7,8]

While this circulation occurs, the microcirculation, *i.e.* the circulation of the blood into capillaries, does the diffusion and filtration of the blood that return the byproducts which are removed by the veins as a collecting system.[6] The blood that leaves the heart by the aorta is of a bright red colour because it is rich in oxygen, while flowing through capillaries, it loses some of the oxygen and pick up carbon dioxide, thus becoming darker.[8]

Blood vessels are organized as an arborisation, usually called arterial tree. The number of the vessels at a particular level of the arborisation increases enormously from a single artery (aorta) to many small arteries ($\sim 10^4$), arterioles ($\sim 10^7$), and finally capillaries ($\sim 10^{10}$).[6]

2.2 Physical properties of the blood and hemodynamics

It is possible to establish a relationship between the diameter of the vessels, the number of the vessels, the velocity of the blood, the cross-section vessel and the pressure applied in the system. The Figure 2.1 represents this relationship.

Since capillaries are the vessels with the smaller diameter, they need to be very numerous to achieve total cross-section (4500 - 6000 cm^2) larger than the cross-section of the remaining vessels. On the other hand, aorta and vena cava, which are at the beginning and ending of the arborisation, are the large vessels, their total cross-section is 3 - 5 cm^2 and 6 cm ^{2}, respectively.[6–8]

Regarding to the velocity, the blood flows into the capillaries with lower velocity when compared to larger vessels, which can be explained by the law of continuity. This principle applies the conservation of mass and, in our case, claims that the total volume flow of blood must be the same at any level of the arborisation, leading to an inversely proportion relation between the total cross-section of the vessels and the blood velocity.[6,8] As consequence, smaller vessels, which have a higher total cross section, have the lowest blood velocity, approximately, 0.1 cm/s.[10] The opposite occurs with the large vessels, where the velocity of the blood through vena cava and aorta reach 15 cm/s and 40 cm/s, respectively.[8]

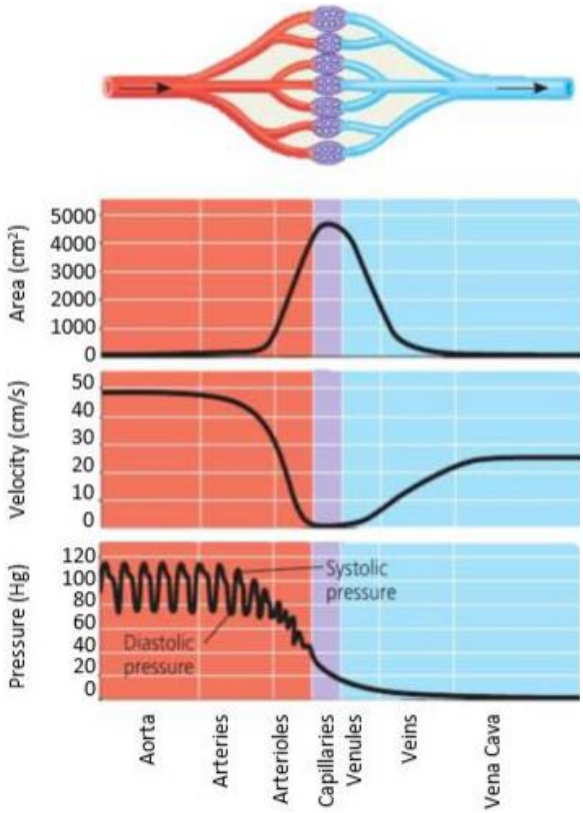

Figure 2.1: Profile of key parameters along the cardiovascular system. Top panel shows the branching of the cardiovascular system. Second panel shows the variation of the aggregate cross-sectional area of the all vessels at any level of the branching. Third panel shows how the average linear velocity of the blood varies along the arterial tree vessels. Bottom panel shows the pulse wave profile of the blood pressure. Adapted from McGraw-Hill High Education, available online.[9]

Concerning to the pressure, it is known that the blood flows from regions of higher pressure to regions of lower pressure.[8] When the blood flows through the arterial tree, the pressure inside the vessel is correlated with their cross-section. This means that, in central vessel like aorta, the pressure is higher (normally between 70 - 120 mmHg) than in the capillaries (normally $\sim$ 25 mmHg).[6,8]

The energy of the blood propulsion is given by the heart, which imposes a pressure gradient over the vessel length. In conditions of laminar flow, which occurs when a fluid flows in parallel layers, with no disruption between the layers, the Poiseuills law (Equation 2.1), relates pressure variation in a vessel, ΔP, and the blood flow, Φ.

$$\Phi = \frac{\pi r^4 \Delta P}{8\eta l}, \tag{2.1}$$

where r is the diameter of the vessel, l is the length of the vessel over which the pressure gradient exists and η is the viscosity coefficient of the fluid.[5,7] The blood flow

is described as a volume of blood that flows through a vessel (cross-section area) in a given time period.[7,8] With a simple observation of the Figure 2.1 we can say that the main factor that influences the velocity, in the arterial tree, is the vessel diameter.[5]

To maintain the metabolic requirement of the tissues, it is important to control the blood pressure. For this purpose, the blood pressure control system uses a negative feedback mechanism which makes the adjustment of several vessels physical properties, using vasodilatation and vasoconstriction chemical substances. This process is called auto-regulation.[7,8]

2.3 Macrocirculation

Cardiovascular diseases are a major concern in health systems of many developed countries. Thus, methods that allow its monitoring and the diagnostic of several diseases in patients are needed. Sometimes, associated to cardiovascular diseases, it happens an increase of the arteries walls stiffness. This stiffness increment begins in the early stage of the disease, hence, if this phase is observed with a non-invasive method, the probability of controlling diseases such as atherosclerosis is higher.

There are indicators to assess the cardiovascular system risk, such as the local pulse pressure, the pulse wave velocity and certain waveform characteristics. When the arteries stiffness increases it loses compliance, so the distension profile of the artery can be used to assess the risk of cardiovascular diseases.[4]

2.4 Microcirculation

The microcirculation comprises the blood circulation in smaller calibre vessels, where the diameter is lower than 100 μm. In other words, the microcirculation is the circulation in the capillaries, from arterioles (input) to venules (output).[3,11,12]

The main function of microcirculation is to allow the distribution of oxygen and nutrients to the cells, ensuring the maintenance of their functions.[3] For this purpose, when variations in the concentration of blood gases, hormones and physical factors, such as temperature and pressure, occurs, the microcirculation flow changes.[12]

The autonomous nervous system controls the blood flow changes. It allows to increase or decrease the microvascular perfusion, if more or less oxygen or other molecular substances are necessary.[5,12] Capillaries are very simple and are not able to carry

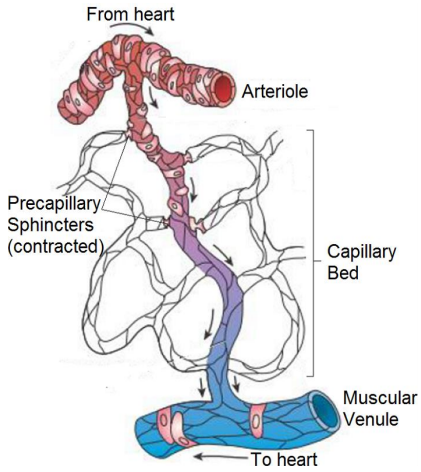

Figure 2.2: Capillary flow regulation. Arteriole, capillaries, and venule. Precapillary sphincters regulate the blood flow through capillary beds. Adapted from Tortora (2008).[8]

out vasoconstriction and vasodilatation. Therefore the capillary flow is regulated by relaxation and contraction of the pre-capillary sphincters, as illustrated in Figure 2.2.[11]

2.4.1 Capillaries

Capillaries are the most peripheral vessels of the arterial tree, they have diameters of 5 - 10 μm and connect the arterial outflow to the venous return. The red blood cells have a diameter of 8 μm. So, in order to cross the lumen of the capillaries, they fold upon themselves.[5,7,8]

These vessels have very thin walls, just a layer of endothelial cells fenestrated, making them highly permeable to water and other molecular substances diffusion. These characteristics ensure a fast exchange of flow, gases, nutrients, hormones, metabolites and cellular excretion products between the blood and the interstitial liquid. The exchange of many substances through endothelial cells occurs by diffusion or pinocytosis (transport of liquids or small particles across the plasma membrane).[7,8,11]

2.4.2 Cutaneous microcirculation

The skin is the largest organ of the body and its main role is to protect it against the external agents. However the skin has a very important function in the regulation of body temperature. It is 1 - 2 mm thick and it is organized by layers: epidermis, dermis and hypodermis, as it is illustrated in Figure 2.3.[8,11]

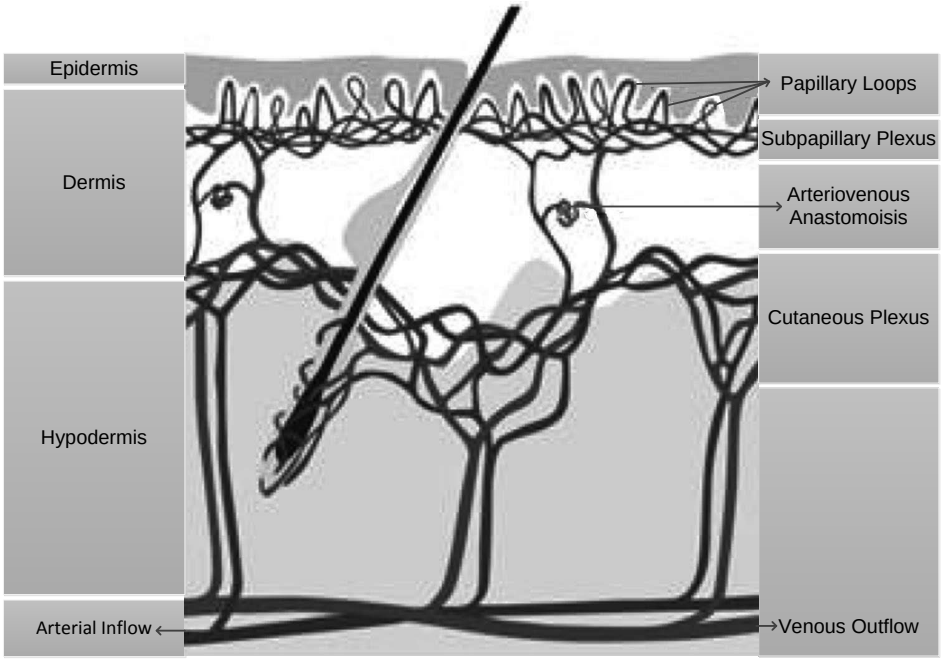

Figure 2.3: Artistic representation of the skin micro-anatomy.[12]

.

The most superficial skin layer is the epidermis, it has a thickness from 50 to 400 μm, and does not presents blood vessels. Concerning the optical properties of the skin, it is translucent to the light, especially to near-infrared radiation. Keratinocytes, producers of keratin, are the major constituent of the skin, followed by melanocytes which produce melanin. Melanin is the pigment which gives colour to the skin, it absorbs radiation between 200 - 800 nm, nonetheless the absorption coefficient increases with the decreasing of wavelength.[8,12]

Dermis is located below the epidermis and it is composed of a strong connective tissue, containing collagen, elastic fibres and the microvascular network. Based on its tissue structure, the dermis is divided into a supercial subpapillary plexus, which is located at a depth of 400 - 500 μm from the surface, and a deep cutaneous plexus which is located at about 1.9 mm from the surface. In the dermis papillary, the capillaries are arranged in loops.[8,12]

Blood flows through the skin, some of which may shunt through arteriovenous anastomoses (AVAs). AVAs are vessels which are a direct connection between arterioles and venules, without a capillary connection.[7] AVAs provide alternatives routes for blood to reach in all parts of the boody.[8] They have the ability to rapidly change the blood flow in order to feed or to drain the capillary network. In the skin, the AVAs are located on dermis layer and they have the additional role of body temperature regulation. When the body is exposed to high temperatures, the AVAs receive the blood

flow in order prevent it to reach the surface. In a situation of low body temperature, AVAs receive less blood, once the superficial layer needs to warm up.[3,6]

The subpapillary plexus is connected to the cutaneous plexus by networks of ascending arterioles and descending venules, which form the cutaneous plexus. In some areas such as the fingers, nose, lips and ears, the AVAs can be found between the two referred plexus.[12]

Hypodermis is the deepest layer, it is organised by arteries and veins of small diameter.[12] In the cutaneous microcirculation, 90% of the blood is in larger vessels, the thermoregulatory layer. The remaining, 10%, are present in the nutritional layer, the most superficial layer.[8,13]

2.4.3 Microcirculation diseases

A microcirculatory dysfunction is characterized by abnormal changes in vessel diameter or alterations of microvascular blood flow. Sometimes the microcirculation loses its capacity of autoregulation, which is characterized by a hyperperfusion, hypoperfusion or complete absence of blood flow.[5,14] These disorders can represent a pathological picture of diseases like:[5,15]

Raynauds phenomenon - after an exposure to extreme cold or emotional stress the fingers and toes become ischemic. This reaction occurs due to excessive sympathetic stimulation of the smooth muscle in the digital arterioles. As a response, the vasoconstriction occurs, which greatly reduces blood flow. Many patients with Raynauds phenomenon have low blood pressure.[8]

Diabetes - the production of insulin by the pancreas is not enough or the cells do not respond to the insulin produced. The long-time complications, such as the atherosclerosis, are mainly in microvasculature where the vessels calibre is reduced.

Figure 2.4: Proportion of deaths due to diabetes in people under 60 years of age in 2013 (Source: *IDF Diabetes Atlas Sixth Edition, International Diabetes Federation 2013*).[16]

The blood flow in the thermoregulation increases abnormally and the nutritional flow becomes insufficient during high flow demand.[3,12] According to the International Diabetes Federation, in 2013, 28.2% of the European population under 60 years died due to diabetes, see Figure 2.4.[16]

Peripheral Arterial Occlusive Disease (PAOD) - large blood vessels of PAOD patients are stenotic, which means that the narrow, reducing the blood flow toward the distal parts of extremities, mainly due to the presence of atherosclerosis. The insufficient microcirculation causes ulcers and skin necrosis in fingers and toes.[12]

Chapter 3

State of the Art

The importance of microcirculation assessment was first described by Cutler in 1929. Ever since that moment, the investigation developed many methods and instruments in order to monitoring the blood flow.[17] The skin is the most exposed organ in the body, so it is used as a way to evaluate the microcirculation through non-invasive optical techniques. These techniques allow the measurement of the perfusion of blood.

In this section several optical methods used to assess the microcirculation are described, such as the Laser Doppler Flowmetry (LDF), the Laser Doppler Imaging (LDI) and Laser Speckle Imaging (LSI).

3.1 Optical Properties of the Tissue

The biological tissues are not homogeneous and in the case of the skin, it is composed essentially of water but also keratin, blood vessels, nervous termination, adipose cells, among others.[18]

The skin has a refractive index of 1.55, therefore, part of the light that goes towards the tissue is reflected in the air-tissue interface. The remaining light penetrates the skin, where it is scattered and absorbed. The ability of light to penetrate tissues depends on its attenuation coefficient which is related with its components. So, the composition defines the quantity of scattered and absorbed light.[18,19]

In the skin, at ultraviolet (UV) and infrared (IR) wavelengths, the light is absorbed by the water and a few cells. At low wavelengths, such as green and yellow ($\approx$ 490 - 600 nm), the light penetrates from 0.5 - 2.5 mm. For wavelengths smaller than 520 nm the penetration diminishes exponentially. In near IR and IR (600 - 1600 nm) the

photons penetrate in the skin very well, up to 10 mm, hence this range of wavelengths is very used as 'diagnostic window' for deeper assessments.[18–20]

3.2 Cutaneous Macrocirculation Monitoring

Laser Doppler (LD) effect (explained in 3.4) can be used to assess macrovascular features. LD is a method used to obtain the waveform profile from the carotid artery, which is an elastic artery and it is close to the heart. Tânia Pereira, from University of Coimbra, constructed a device to assess the macrocirculation in the carotid artery in order to be simple, inexpensive and to use an signal processing tool with high accuracy to extract clinical relevant parameters. The optical probe uses a laser diode which emits and detects the photons. When the emitted light reaches moving surface, it is reflected with a different frequency according to the speed of the surface. If the analysed sample is an artery, the light frequency changes transduce the arterial distension wave. when the reflected frequency shifted light reenters the laser cavity, it mixes with the original frequency light, thus creating a beat wave.[4]

Vânia Almeida developed another method for macrovascular assessment: a piezoelectric probe. When the probe is placed in the skin surface, upon the carotid artery, it is subjected to a mechanic pressure from the artery distension and responds with an high sensibility, converting the mechanical signal to an electrical signal.[21,22]

3.3 Cutaneous Microcirculation Monitoring

There are evidences that prove that the microcirculation dysfunction increases with age. To understand the impact of a pathology on the circulatory network, studies have been done.[23] When there is a dysfunction the circulatory system is affected.[24] Thus, when assessing the peripheral microcirculation, such as the cutaneous microcirculation, we can detect changes, making a diagnosis.[15]

Moreover, in other cases, the skin microvasculature is specifically affected, such as in systemic sclerosis, burns or wounds. Since the skin microvascular function is changed, the assessment of the microcirculation could be used to assess the severity of the lesions and the recuperation.[15]

The 3D microcirculatory network is very complex and has many functions, such as nutritional and termoregulation, thus is not easy to assess them, as it is in macrocirculation. However, methods to monitor the cutaneous microcirculation have gain major

attention of investigators. The diagnosis based on optical properties has increased too, mainly due to the availability of optical technology.[3,18] Optical techniques for the assessment of physiological parameters are very attractive because they provide simple, non-invasive and continuous physiological monitoring, as desired.[18]

The optical methods, such as Laser Doppler Flowmetry, Laser Doppler Imaging, Near IR Spectroscopy (NIRS), Orthogonal Polarization Spectral imaging (OPS) and Side-stream Dark Field imaging (SDF) are been used as methods for the non-invasive exploration of cutaneous microcirculation.[3,15,18]

LDF, LDI and LSI technique are the best known optical techniques for diagnosis of cutaneous microcirculation. It is important to state that several of these methods are not able to discriminate the assessment depth, or the type of the vessels.[25] This is one of the limitation of using light as the carrier of information for biomedical applications.

3.4 Laser Doppler Flowmetry and Laser Doppler Imaging

As the name states, Laser Doppler Flowmetry and Laser Doppler Imaging use the Doppler effect in order to measure the microcirculation flow. According to the Doppler effect when the photons hit scatters (red cells), they reflect the photons with a frequency different from the original. The scatters relative velocity influences the change of frequency. Thereby, it is possible to determine the velocity of the blood flow using the Doppler effect.[3]

The first studies with an implementation of the LDF technique were developed in the 1970s.[26] Since that, many reports were published in order to improve the method. In the 1980s, the first fluxometer was developed by Jones and Mayou.[27] LDF can be an invasive or non-invasive technique, which allows the blood flow monitorization in a single point and in real-time. Since LDF records a single point of the sample, it is only representative of that point, which may not be a general overview of the entire tissue.[3]

In this technique a coherent light beam (laser) illuminates the biological tissue through an optical fibre probe. In the tissue, the photons are absorbed, reflected, transmitted or scattered. The Doppler effect occurs when the photons are scattered by the red cells which produces the frequency shift. Then, these photons and the photons that are reflected by the static particles are guided by an optical fibre (the same or another) and are detected in photodetectors. Finally the optical power is converted in an electrical signal in order to be processed.[3,28] Usually the LDF uses laser diodes with

a wavelength of the 780 nm (IR) because, in this frequency, the photons can penetrate the skin independently of the melanin levels.[15]

In 1991, Essex and Byrne introduced the LDI, in order to study a larger area, a 2D image, instead of a single point, as in LDF.[29] In this method the 2D image of the blood perfusion of the skin area is registered by a scanning mechanism. The laser light is guided to the biological tissue using a moving mirror and the scattered photons are guided to the photodetector, using the same mirror.[3,11,15]

With the propose of improving the existing methods, Edite Figueiras developed two new probes based on LDF that use three different wavelengths. This allows to discriminate three distinct depths of the microcirculation flow.[3,25,28]

3.4.1 Advantages and Drawbacks

LDF, besides being an invasive or non-invasive method, has a high sensitivity and responsivity to local blood perfusion. LDF is versatil, simple, easy to use and can perform measurements in real-time. However, the results of the blood flow and hemoglobin concentration are given in arbitrary units and not in absolute values. Thus, it is not used in healthcare service very often. Other problem is the lack of standardization of the method, resulting in different outcomes of blood flow when the same area is under study with different instruments.[3,11,15,18,28]

The main limitation of this method is the uncertainty of the assessment depth. This leads to some ambiguity in the interpretation of the results. It is not possible to determinate the light dispersed in superficial or deep layers (nutritive and thermoregulatory layers respectively).[18]

LDI has the advantage of recording the spatial variations of the blood flow, however the time that is needed to scan a large area is too high to capture fast variations.[11,18]

3.4.2 Applications

The LDF and LDI have several applications in health care, such as: plastic surgery;[18] gastrointestinal surgery;[18] dermatology;[11] skin blood flow studies;[15] burn assessment[29] and rheumatology.[11]

In many cases, real-time monitorization is necessary. As the LDI needs few minutes, 1 to 5 minutes, to digitalize the image, it can not respond to this situation, for this reason LDI is not viable yet.[11]

3.4.3 Commercial Devices

There are many types of equipment to measure blood perfusion. The fluxometers technique and instrumentation depend of the tissue region where the flux is measured.[26] Some of these instruments present color-coded images of microcirculatory flow patterns, providing temporal and spatial information.[18]

PeriFlux (Parimed®, Sweden)is a wide used LDF. This instrument is able to evaluate the microcirculation blood flow in real-time and it can be an invasive or non-invasive method. The signals obtained are about perfusion, concentration of hemoglobin, temperature and velocity.[3,30]

OxyLab LDF and OxyFlo (Discovery Technology International, Florida) are two LDF instruments. They have incorporated a recently digital signal processing system, setting new standards for reliability and robustness.[31]

3.5 Orthogonal Polarization Spectral and Side-stream Dark Field imaging

Orthogonal Polarization Spectral (OPS) and Side-stream Dark Field imaging (SDF) are similar techniques. In OPS the tissue is illuminated with linearly polarized green light and the scattered photons create the contrast image. The photons of interest are those that are scattered by the deeper layers of the tissue. SDF is an improvement of the OPS technique, the illumination is provided by LEDs, concentrically placed around a central light (green laser). The green light is scattered by the deeper layers of the tissue while it is absorbed by hemoglobin, providing an image in which red blood cells appear as dark moving spots contrary a white/greyish background.[15,32]

The images obtained are only semi-quantitative, determining the perfused capillary density and the flow heterogeneity between different areas. The semi-quantitative assessment of the skin blood flow is not fully automatized yet.[15]

The pionners in the OPS imaging, in 1991, were from Philadelphia.[32] Now, Rytometrics in Philadelphia and Affymetrix in Japan commercialize the CytoScan, that perform the OPS-SDF imaging.[33]

OPS and FDS imaging have been used during surgery to assess the blood flow of several organs, such as the brain, the kidney or the liver. However the sublingual region is the most studied site. Although the main application of the two techniques

is in critical care medicine, these methods are used on lower limb skin to evaluate the microcirculation in chronic venous insufficiency or in burn wounds.[15]

These techniques are relatively inexpensive, portable and have a great image resolution. Nevertheless they have limitations, the external agents cause the image blurring and, in these techniques, affect the results. In SDF imaging this is attenuated. The melanin degree is a limitation because it absorbs light at a similar wavelengths to hemoglobin.[15]

3.6 Laser Speckle Contrast Imaging

The microcirculation assessment based on optical technologies has been developed for a long time. In the last decades, the laser speckle contrast imaging (LSCI) techniques reached the attention of researchers. This method is non-invasive and allows the achievement of real-time microcirculation images.

Laser speckle imaging (LSI) is the technique used to obtain the speckle pattern images. When a coherent light interacts with a rough surface is created a laser speckle (LS) pattern, black and white granules, which reflects the dynamics and structural properties of the surface. In Figure 3.1 it is possible to observe an example of a typical LS pattern.

In the literature, the technique of using speckle patterns to extract medical information, is also described as LSCI[35–37] or laser speckle contrast analysis (LASCA).[38–40] The acronym LSI is also used to describe a method that calculates the speckle image contrast.[41,42] In this paper LSI is referred to a technique that creates the speckle pattern in a sample to extract biomedical information. LSCI is used to describe the processing methods that are based in contrast analysis of the images acquired with

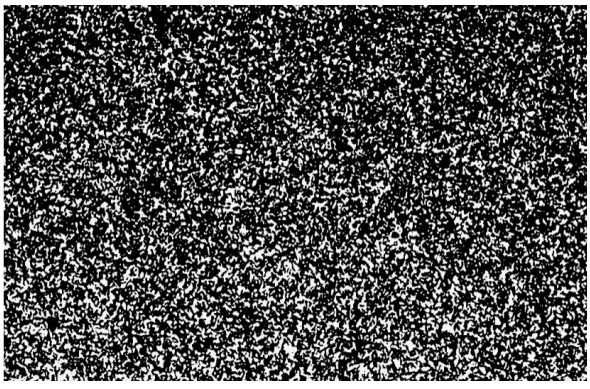

Figure 3.1: A typical laser speckle pattern. Adapted from Briers *et al.* (2001).[34]

LSI.

3.6.1 Historical Background

In the 1960s the theory of the LSCI was described for the first time by Goodman. He explained the temporal statistics of the speckle fluctuations, this is the way to obtain the result of the contrast imaging.[43] In the next decade, 1970s, Stern observed the speckle pattern spatial variations along time, called 'time-varying speckle'. He was the first that recognized the applicability of LS principle in the blood flow assessment, since the speckle change occurs when the blood red cells move through the capillaries.[44,45]

Fercher and Briers, in the 1980s, introduced the concept of speckle contrast to measure the blood flow. The contrast reduction happens due to the blurring effect that occurs during acquisition when the scatters are moving. Thus in regions where the particles move the contrast of the speckle pattern image decrease. They implemented this principle in photographic techniques in order to map the retinal blood flow.[46] This technique is known as 'single-exposure speckle photography'. It consists of taking a photography of the area under study using an exposure time which must be long enough to allow the speckle pattern fluctuations, in order to blur the image in the moving scatters zone.[42,47,48] In order to enhance the image quality, an spatial high-pass filter was used to convert contrast variations to intensity variations. This simple method was able to produce a blood velocity map of the retina. In the Figure 3.2, it is possible to observe the output of this technique.[47]

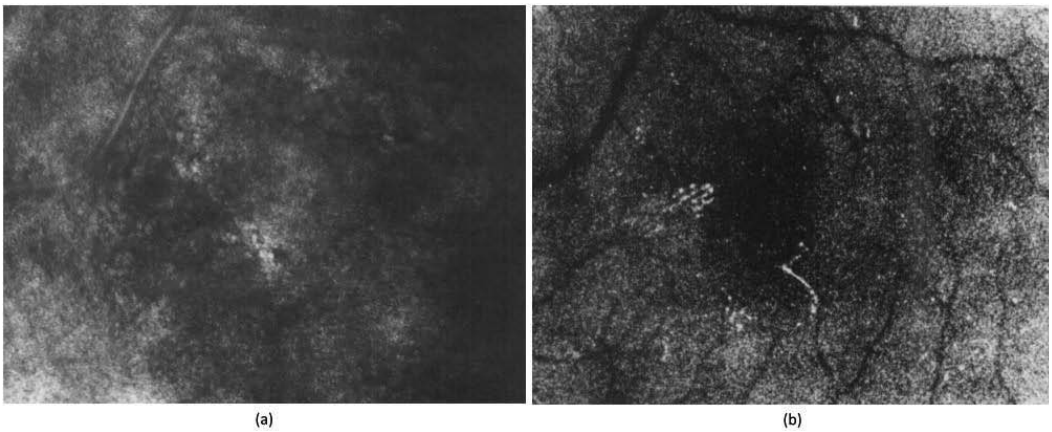

Figure 3.2: Single-exposure speckle photography of the human retina *in vivo* ($50mW$ helium-neon laser, Kodak 2415 film, 16.7 ms exposure time; maximum retinal irradiance $< 2mW/mm^2$. (a) Raw image of part of the retina. (b) Image spatially filtered by a high pass filter, showing contrast variations mapped as intensity variations. Black pixels represent increased blood flow. Adapted from Briers *et al.* (1982).[46]

Digital acquisitions and processing methods are being developed since the 1990s. Briers *et al.* (1996), in order to achieve a real-time performance, introduced the digital acquisition and processing technologies.[40,49] The contrast was digitally computed under a method named LASCA that is similar to LSCI and can represent false-color images.[48,50,51] This allows the creation of blood flow a map which is correlated with the blood perfusion.[41,52–54]

3.6.2 Theoretical Background

LS is an interference pattern produced by the light that is reflected and scattered from different parts of the illuminated rough surface. The surface is rough when the height variations are greater than the used light wavelength. The light, reflected from the surface, travels different optical paths until it reaches the image plan. In this plan, it is observed the superposition of the waves. The white spots are resulting of the waves that arrive in phase, causing a maximum in the intensity. Black spots are resulting of the cancellation of the waves, which means zero intensity.[43,49]

The speckle pattern changes when the surface moves. If the object carries out small movements, the speckle pattern has few changes, so the speckle patterns remain correlated. Nonetheless, when the speckle changes completely, the speckle decorrelated. This occurs in a fluid motion, when the light is scattered by many scatterers. The speckle decorrelation along time is called decorrelation time (τ_c).[49]

The speckle pattern is recorded with a camera, which does the speckle time integration according to the used exposure time. As it was stated in section 3.6.1, the exposure time must be long enough to create a blurring effect in the areas where the speckle decorrelates.[42] Figure 3.3 presents the optical set-up scheme of LSI.

The next step is to compute the contrast. The speckle contrast, C, is defined as the ratio of the standard deviation of the intensity, σ, to the mean intensity, $\langle I \rangle$, of the speckle pattern:[43]

$$C \equiv \frac{\sigma}{\langle I \rangle}. \tag{3.1}$$

In ideal conditions, for a static speckle pattern, with highly coherent light, the standard deviation equals to the mean intensity, leading to maximum contrast, $C_{max} = 1$. However, in dynamic speckles, when change of the speckles occur, the speckle decorrelation increases, leading to a blurred image which means lower standard deviation. Analysing the Equation 3.1, we can conclude that the speckle contrast image is reduces.[42,49] The other cause that usually cause the C_{max} to be lower than 1 is the failure of the Nyquist sampling criterion, that need to have a pixel size $\leq \frac{1}{2}$ speckle size.[56]

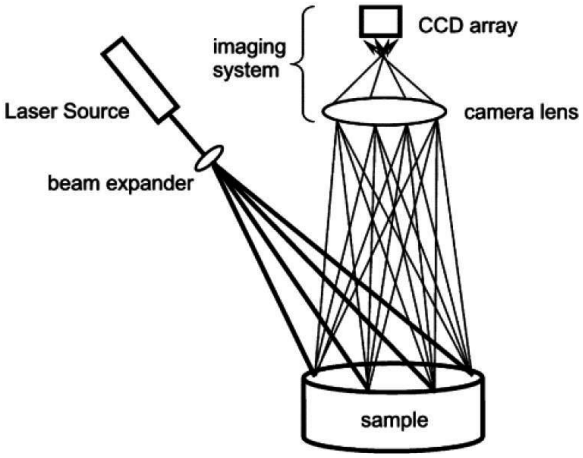

Figure 3.3: The optical scheme set-up of LSI. The sample is illuminated by a laser source and the imaging system records the resulting image. The camera is connected with a computer that allows the visualization of the speckle pattern and the computation of the contrast image. Adapted from Leahy *et al.* (2007)[55]

Flow velocity

The deduction of the flow velocity from the observed speckle contrast and decorrelation time is adapted for different velocity profiles.[41] The Lorentzian model is a homogeneous line profile appropriate only for Brownian motion. In such case, the dynamics of a single particle are representative of the ensemble. Otherwise, the Gaussian model is an inhomogeneous profile which corresponds to a process in which the dynamics are particular to the individual scatterers.[57]

In Figure 3.4, it is possible to observe the curves that relate the speckle contrast, C and the ratio of the decorrelation time, τ_c, to exposure time, T. The solid curve represents the behaviour of the contrast when we have a Lorentzian velocity distribution. The dashed curve represents the behaviour of the contrast when we have a Gaussian velocity distribution.[49]

The two flow distribution profiles are used in research.[56,58] Assuming that all the scatters have a Lorentzian velocity distribution, the contrast speckle can be described by:

$$C \equiv \frac{\sigma}{\langle I \rangle} = \left(\beta \left\{ \frac{\tau_c}{T} + \frac{\tau_c^2}{2T^2} e^{\left(\frac{-2T}{\tau_c} \right)} - 1 \right\} \right)^{\frac{1}{2}}, \tag{3.2}$$

where T is the exposure time, β is a constant introduced to account for the loss of correlation related with the ratio of the detector size to the speckle size and to the light polarization.[49] Researchers in this field have obtained β by a linear system correlation of speckle contrast curves.[39] Using multi-exposure time acquisitions, it is possible to

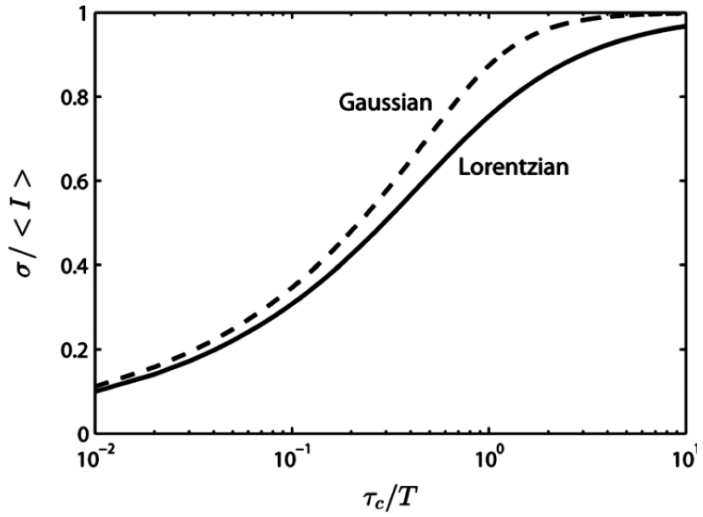

Figure 3.4: Theoretical relationship between speckle contrast and τ_c/T, assuming a Lorentzian and a Gaussian velocity distribution. Adapted from Briers *et al.* (2013).

obtain τ_c, decorrelation time, with some precision through several points of contrast $C(T)$ which allows the fitting of the non-linear curve.[56]

The flow velocity can be estimated from the decorrelation time of intensity fluctuations over a predetermined time duration. According to the literature, the decorrelation velocity, v_c is related to the decorrelation time, by the equation:[41,46,59]

$$v_c = \frac{\lambda}{2\pi\tau_c}, \tag{3.3}$$

where λ is the laser wavelength. For fast moving speckle, the decorrelation time is small, as v_c and τ_c are inversely proportional. Since the number and the direction of the moving scatters are unknown, the computed blood flow is only a relative measure and not absolute.[41,47]

Depth discrimination studies

LSI has the problem of the reduced sampling depth. This technique gives only information about the superficial layer. Doherty *et al.*, in 2009, estimated that the sampling depth of laser speckle perfusion imaging was about 300 μm.[59]

He *et al.* (2012) presented a laser speckle technique for deeper assessment. This technique is based in a sample scanning with a linear laser, while the image acquisition system remains static. Different source-detector separations cause the photons to reach different depths due to the 'banana-shaped' effect. Deeper tissues can be assessed when longer source-detector distances are used.[60]

Bi *et al.* (2013) made their contribution in the study of the deeper perfusion by

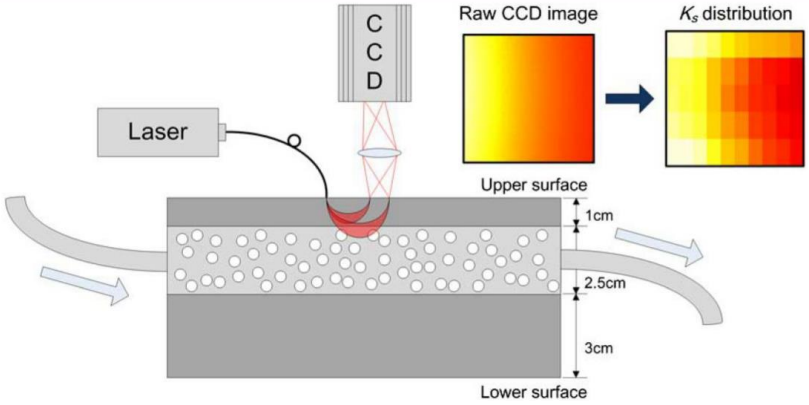

Figure 3.5: Schematic of light flux in the tissue. The first square represents the laser speckle imaging collected and the second, the image after processing in order to obtain the speckle contrast image. Adapted from Bi *et al.* (2013)[38]

presenting the diffuse speckle contrast analysis (DSCA). This method uses the principle of the 'banana-shaped' trajectory (Figure 3.5), where the laser illuminates a point of the sample, contrary the LSCI that uses a beam expanded to test an area. In DSCA, the laser is directed to the sample with a given angle, this allows the multiple scattering. In the detector, a CCD camera, the photons which travelled in the superficial layer are detected in the area close to the laser and the photons which reached the deeper medium are detected further away from the laser. In this study they used a source-detector separation of 1.8 cm.[38]

About light sources, the lasers used in LSI techniques have typically wavelengths of 633 nm,[40,56,61] 660 nm,[62] 680 nm[63] and 785 nm.[38,51] Their optical powers varying from 5 mW,[63] 40 mW,[40] 70 mW,[51] 100 mW[38] and 130 mW.[62]

3.6.3 Practical Concepts

In LSCI methods there are several parameters which define the quality of the final speckle contrast. Speckle size, camera exposure time and the computation window size are the main factors.

A. Speckle size

The speckle size depends on the imaging system. It can be determined by Equation 3.4:

$$d = 1.2\lambda(1 + M)f_{\#}, \tag{3.4}$$

where d is the diameter of the speckle spot, λ is laser wavelength, M is the magnification of the imaging system and $f_{\#}$ is the camera F-number. The F-number is the ratio of

lens focal length to the aperture diameter (effective aperture).[41,48] The speckle size should not have a diameter below the camera pixel size, otherwise the contrast will be degrade. However, very large speckle sizes also reduces the spatial resolution.[64]

B. Camera exposure time

The camera exposure time is the main parameter that contributes to the blurring effect in the areas where the particles are moving. Exposure time needs to be a finit value for imaging. This parameter must be high enough to allow an adequate number of accumulated photons, creating blurring effect, and low enough to maintain the speckle contrast. High exposure times eliminate the signal, deteriorating the final image. Thus there must be a compromise between these two factors. Exposure times between 1 - 50 ms are suggested to maintain a good relation of the contrast to noise ratio.[41,64]

C. Contrast window size

LSCI methods are based in the computation of the contrast (C) in pixel windows across the images. If the window size is large, the accuracy of the speckle contrast estimate is high, but the spatial resolution is reduced.[48] For a small window size the estimate of local contrast is statistically erroneous. Causing noise in the final image.[64]

Previews works, recommend that the window size, used to calculate the speckle contrast, must be of 3 x 3, 5 x 5 or 7 x 7 pixels. This is a reasonable trade-off between spatial resolution and uncertainty in the speckle size estimation.[40,41,48,49]

3.6.4 Different Methods of Laser Speckle Contrast Imaging

The LSCI techniques are classified in temporal and spatial domains.[41] LSCI algorithm computes the speckle contrast (Equation 3.1) in a given window size (square volume of pixels) and assigns this value to the central pixel of the window. The final image represents the information of contrast speckle in all the spatial pixels.[40] The literature is unclear in the definitions of the existing methods. So we define the methods used hereinafter according to their domain of application. They are the spatial LSCI (sLSCI), temporal LSCI (tLSCI) and spatiotemporal LSCI (stLSCI).[64]

Spatial LSCI

The sLSCI is a method that performs the contrast calculus in the spatial domain. In Figure 3.6 (a) it is possible to observe the scheme of sLSCI. Using sLSCI method, the computation of the contrast in a pixel, $C(i, j, t)$, with a window size, w, can be

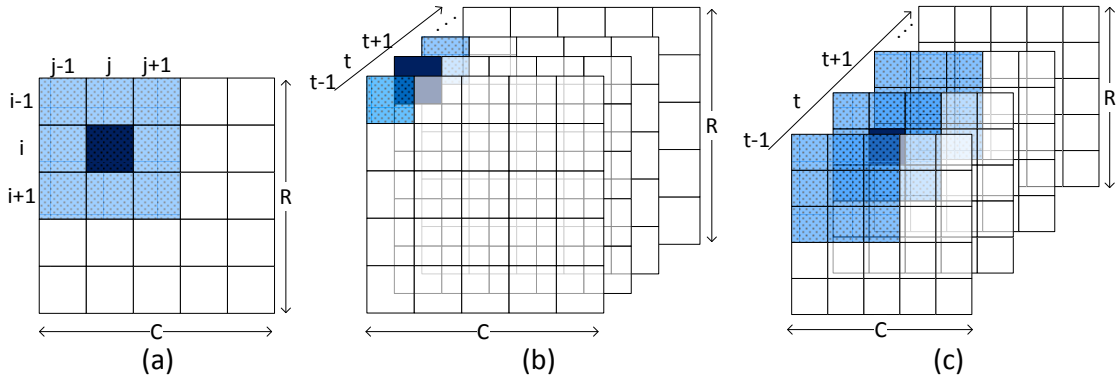

Figure 3.6: Schematic diagrams of LSCI methods. (a) sLSCI, spatial statistics (b) tLSCI, temporal statistics (c) stLSCI, spatiotemporal statistics. $C \times R$ pixels in each sub figure represents a frame of the original speckle image. The blue pixel in each method is the pixel where the contrast is calculated. The cyan pixels that are around the central pixel, blue, represent the window that contribute to the contrast speckle computation.

described by:

$$C(i,j,t) = \frac{\sigma_{(i-\frac{w-1}{2}:i+\frac{w-1}{2},j-\frac{w-1}{2}:j+\frac{w-1}{2},t)}}{\left\langle I_{(i-\frac{w-1}{2}:i+\frac{w-1}{2},j-\frac{w-1}{2}:j+\frac{w-1}{2},t)} \right\rangle}, \tag{3.5}$$

where i, j and t are the position of the pixel, raw, column and frame, respectively. The contrast window is further displaced along the image with full overlap.

This technique provides the highest temporal resolution, while compromising on spatial resolution.

Temporal LSCI

The principle of tLSCI is the same of the sLSCI, however it is applied in the temporal domain. In Figure 3.6 (b) it is possible to observe the scheme of tLSCI. In this algorithm the contrast is determined in a sequence of speckle images over a single pixel, $1 \times 1 \times W$.[64] In tLSCI, the computation of the contrast in a pixel, $C(i,j,t)$, with a window size, w, can be described by:

$$C(i,j,t) = \frac{\sigma_{(i,j,t-\frac{w-1}{2}:t+\frac{w-1}{2})}}{\left\langle I_{(i,j,t-\frac{w-1}{2}:t+\frac{w-1}{2})} \right\rangle}, \tag{3.6}$$

where i, j and t are the position of the pixel, raw, column and frame, respectively.

The tLSCI has a high spatial resolution, however the temporal resolution is impaired. Several studies has shown that tLSCI, compared with the sLSCI, reduces the undesired effects that occurs in the speckle image due to the presence of static scatters.[64]

Spatiotemporal LSCI

This technique is the combination of sLSCI and tLSCI.[64] In the literature, this technique is also called laser speckle flowgraphy (LSFG).[41] The stLSCI determines the contrast using voxels of pixels, $w \times w \times w$ pixels, in the temporal and spatial domain, as shown in Figure 3.6 (c).[64] This method can be described by:

$$C(i,j,t) = \frac{\sigma_{(i-\frac{w-1}{2}:i+\frac{w-1}{2},j-\frac{w-1}{2}:j+\frac{w-1}{2},t-\frac{w-1}{2}:t+\frac{w-1}{2})}}{\left\langle I_{(i-\frac{w-1}{2}:i+\frac{w-1}{2},j-\frac{w-1}{2}:j+\frac{w-1}{2},t-\frac{w-1}{2}:t+\frac{w-1}{2})} \right\rangle}, \tag{3.7}$$

where $C(i,j,t)$ is the contrast in a specific pixel, i, j and t is the position of the pixel, raw, column and frame, respectively.

The stLSCI must be used having into account a trade-off between temporal and spatial resolutions and the contrast accuracy.[64] This technique is usually applied for fast-changing perfusion levels.[42]

3.6.5 Advantages and Drawbacks

In many publications, the advantages of using laser speckle technique are recognized.[41,45,49,65,66] LSI is a non-invasive method and is carried out in real-time. The technique is easy to implement and the processing is simple. Comparing with LDF, LSI provides high temporal and spatial resolution images and a excellent reproducibility.

The acquisition of data is fast and is released without scanning, necessary in LDI. In LSI a single shot allows to obtain the blood velocity map in a skin region. To release the acquisition of speckle images pattern, is required only standard hardware.

Although many advantages, LSI has some limitations and drawbacks. Also in others methods, the blood perfusion obtained by the processing, is a relative data and not an absolute value. The ability to discriminate many layers in a single acquisition is a limitation that needs to be overcome. This will make this method a tool with a great potential.

About measuring depth is necessary more studies. Currently, when a wavelength of 780 nm is used the explored depth is $\approx$ 300 μm. LSI is used to test the nutrition supply. However, it would be interesting to collect the speckle pattern in several depths and to discriminate the layers using the correlation calculation.

Finally, there are many factors that are an influence in the LSI acquisitions. For example, the speckle pattern is sensible to the air movement above 2.8 m/s and the

light should always be kept as stable as possible.

3.6.6 Applications

LSI techniques allow blood flow imaging in span hands, tissue types and diseases with high-resolution required. Their importance is recognized by researchers as a tool to use in the microcirculation assessment. In literature many applications are described and studies are made using the speckle contrast methods.[65,67]

The assessment of cutaneous microcirculation is the biggest application of LSI. Briers *et al.* (1996) demonstrated that LSCI techniques can be used to obtain information of microcirculation in the hand. The method consisted in acquiring the hand speckle images after some subjects lay hands in cold and warm water. Then, the contrast of speckle images was computed for two cases. The result showed that on the 'warm' hand the contrast was lower than the contrast obtained on the 'cold' hand, indicating increasing movement of the scatters. They used the Lorentzian model to obtain the flow velocity. The flow velocity of 'warm' hand increased $10 - 50\,\%$, comparing with the 'cold' hand. Furthermore, they proved the increasing and decreasing of flow velocity by contrast variations for rub skin, burn skin and when the blood flow is occluded in a finger.[40]

Forrester *et al.* (2004) compared LSI techniques with LDI techniques. They assess the cutaneous microcirculation at various levels of pigmentation. The results proof that LSI instrument responses to changes in red blood cell concentration similar to LDI.[54]

This tecnique can be interesting to allow the monitorization or diagnostic of diseases, such as the Raynaud syndrome or the diabetes, where it is possible to identify occluded regions. It also can be used in pharmacological tests[41,49,65]

In the brain blood flow imaging, Boas *et al.* (2010) have developed techniques in order to quantify the changes in speckle contrast at each pixel as an indication of the relative cerebral blood flow. The brain function activation can be observed using the speckle contrast changes during a stimulus. Another application in this area is to investigate migrains.[48]

Dunn *et al.* (2001) used LSCI to map the rat cerebral blood flow (CBF) and simultaneous measure the blood perfusion using a laser Doppler probe. Using this method, dynamic images of the CBF changes during cerebral ischemia were obtained. The speckle images demonstrated variations of CBF, so the speckle method allows the

spatial and temporal characteristics of the CBF response to be imaged in studies of functional activation, cerebral pathophysiology, and therapeutic effects of drugs.[68,69]

In the retinal, Tamaki *et al.* (1994) proved that the monitoring of blood flow is possible. They acquired speckle images of rabbit retinal and computed the normalized blur (ratio of average of speckle intensity to speckle intensities difference for successive scans). This method was compared with an other method, the microsphere technique. The results of retinal blood flow show a high correlation between both methods.[50] The retinal blood flow is an indicator to ophthalmological states, it is also used to test the reaction in eye to a given pharmacological agent.[48,70]

Chapter 4

Prototype and Bench Tests

LSI systems are based in a light source (laser), which illuminates the sample, creating a speckle pattern. The speckle fluctuations along time are recorded with a video camera. In this work, LS was used with two distinct goals. The first one is related with the evaluation of the macrocirculation. In this case, a phantom, based in silicon membranes, was designed in order to develop techniques for longitudinal motion identification. The second goal, is related with the use of LS for microcirculation assessment. In this case, an acrylic phantom was used to mimic the blood flow in a blood vessel.

The chapter 4 describes the prototype assembly with the discrimination of hardware and software used for the LS system. It is important to refer that the hardware study and selection was done in previous works using existent materials of the investigation centre where this research is being developed.[2]

4.1 Prototype Assembly

To obtain laser speckle images is necessary to define an hardware and optical configuration which allows a high stability and reliability during acquisition.

4.1.1 Hardware

The necessary hardware to build a LS prototype can be divide into 3 main modules. These modules are: the image acquisition system; the light sources; and the optical configuration. All components used in bench tests were fixed in an optical bench to reach the required stability.

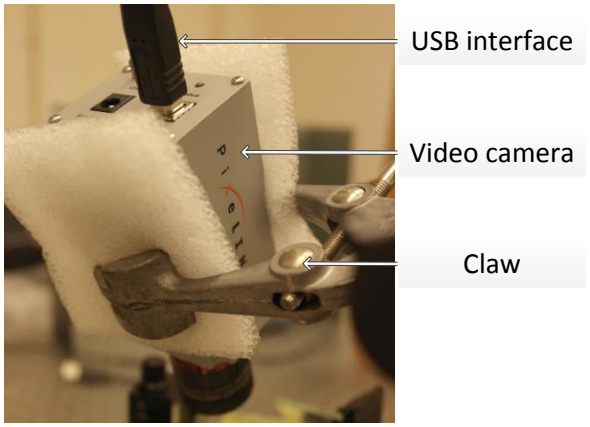

Figure 4.1: Video camera Pixelink PL-B741EU.

Image Acquisition System

The image acquisition system was composed by a Pixelink PL-B741EU video camera (Figure 4.1). It is a monochrome camera with a CMOS sensor and 1.3 megapixels of maximum resolution. It allows a digital output with high performance and responsivity from 700 nm to 1000 nm. Associated with the camera two lens were used. The first with a focal length (f) of 25 mm and a F-number from 1.4 to 16. The second one has a focal length of 50 mm and a F-number from 2.0 to 22. Both lens are from Edmund Optics company.

The lens with $f = 25\,mm$ was used for macrocirculation assessment. Meanwhile, the other lens was used for microcirculation assessment. The reason is that the created speckle, when is used the phantom, had not a size enough. So, for increase the speckle size, a way, is to increase f. When f increases, the F-number increases also. F-number is equal to the f divided by D, where D is the diameter of the entrance pupil. Furthermore, in the microcirculation tests, the used exposure times reach high values. Since the lens of $f = 50\,mm$ reaches higher F-numbers, the hypothesis of the image does not saturate, when are used high exposure times, increases.

It is important to refer that in the acquisitions there are two main camera parameters which must be controlled, the exposure time and the F-number since they interfere in the speckle size and in the blurring effect.

Light sources

Three different light sources were selected to perform this study (Figure 4.2). Due to the required light coherency all the sources were lasers. Their optical and electrical properties are presented in Table 4.1. According to the skin optical properties, the green laser will be absorbed in skin surface meanwhile the IR laser is absorbed in

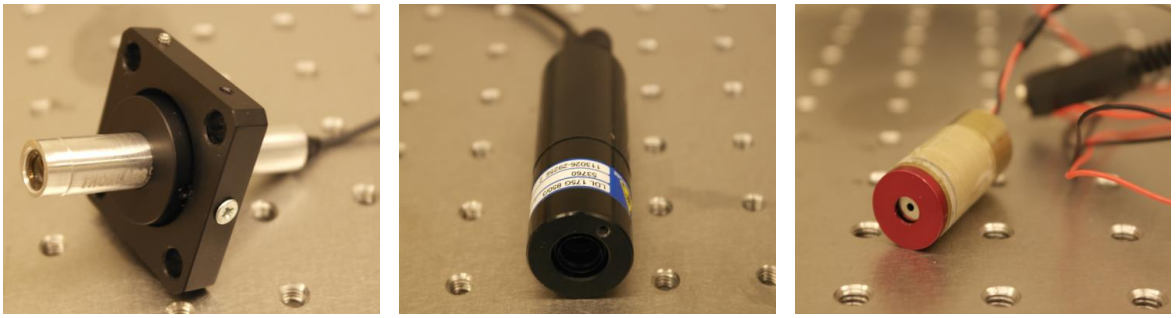

Figure 4.2: Laser lights used in bench assembly. (a) Green laser. (b) Infrared Laser. (c) Red Laser.

deeper layers (Section 3.1).

In the same table the maximum permissible exposure (MPE) are presented for each laser. The MPE was computed when the laser irradiates the skin for long exposition times (10 to 3.10^4 seconds). According to the MPE calculus table, in this case, MPE is $0.2C_A$, where C_A is a laser wavelength constant dependent.[71]

Table 4.1: Optical table and electrical properties of the lasers.

	IR (infra-red laser)	R (red laser)	G (green laser)
Model	LDL175G	-	CPS532
Company	Global lasers	Coherent Inc.	Thorlabs
Wavelength (nm)	850	635	532
Optical power (mW)	3	5	4.5
Laser cross-section (mm^2)	3.14	0.95	9.62
Maximum laser irrandiance (W/cm^2)	0.095	0.526	0.047
C_A	2	1	1
MPE (W/cm^2)	0.4	0.2	0.2

Comparing MPE with maximum laser irradiance obtained, the infra-red and green lasers can be used *in vivo* if the exposure time do not exceed the 8 hours. Since the red laser reaches irradiances greater than the MPE, was used a beam expander to increase the cross-section. Thereby the maximum laser irrandiance decreases.

The light beam created by the lasers have small dimension, insufficient to assess the target area. In order to increase the beam, it were used a beam expander. A beam expander composed by a diverging lens to expand the light beam and a converging lens for the beam to be coherent (Figure 4.3) was used for red and green lasers. However, when is used the infra-red laser, the beam expander is not used due to its low optical power.

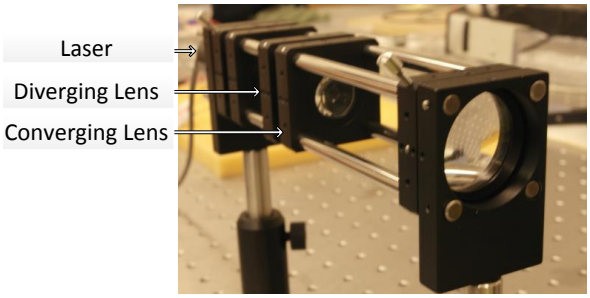

Figure 4.3: Laser and beam expander. Beam expander is composed by a diverging lens and a converging lens.

Optical configuration

The optical configuration of the bench assembly was a milestone during the work. A different optical configuration was used for each application (macro and microcirculation). In order to maintain the optical scheme defined in Figure 3.3 was configured two similar bench assembly. The first one, for macrocirculation assessment, consisted in an horizontal sample illumination that was vertically positioned in front of the light source. The camera was placed along with the illumination axis to record the reflected pattern. It was fixed with a lab claw, close to the sample, doing a certain angle in relation with the laser direction. For microcirculation, the configuration is similar, however, a mirror which reflect the laser beam downwards at an angle of 90° was used. Thus the sample was positioned under the mirror, and the speckle pattern is originated there. The camera was connected with the computer for data storage. In order to avoid any interference of room light, all acquisitions were done with the lights off.

4.1.2 Software

The communication of the video camera with host computer was performed thought a standard USB interface of Pixelink and a proprietary software, 'PixeLINK Capture OEM'. Furthermore, the acquisition control was also done by a Python script, developed by MSc Pedro Vaz, that uses the 'openCV' library. This program allows the video encoding, frame rate and allowing external triggers. The Figure 4.4 shows the software block diagram in order to understand the process.

The first step acquisition is to open the camera interface 'PixeLINK Capture OEM'. In the basic controls the user selects the camera and different parameters, such as the exposure time (ms), the frame rate (fps) and the resolution (pixels). The next step is to open the Python script in idle mode to define the resolution, the frame rate and the acquisition time in seconds. All parameters must be selected according the parameters

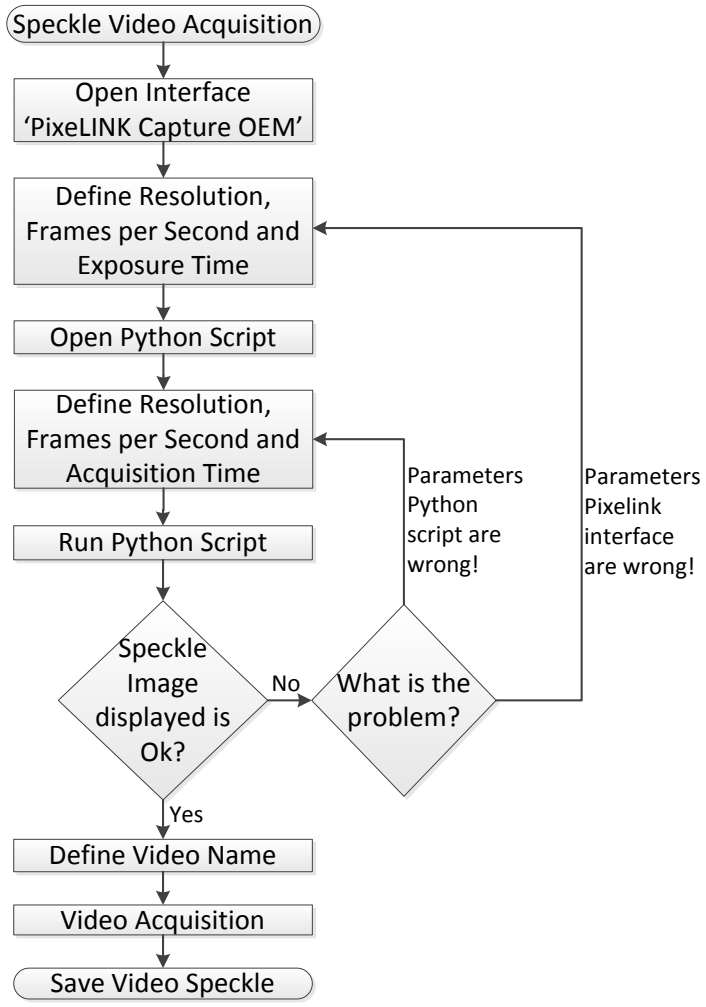

Figure 4.4: Flow chart of the acquisition process.

selected in the camera interface to prevent conflicts. After the parameters selection, the program show an image preview to the user. If the image is as expected, the user give permission to the script to start the acquisition, otherwise the program is aborted and the parameters are modified. Finally, the video with the speckle information is saved without any type of compression.

4.2 Macrocirculation Set-up

4.2.1 Bench Test

The bench assembly for macrocirculation tests aims to reconstruct fine longitudinal moves of diffuse objects, like arteries distension during blood circulation. Using basic principles of imaging, these movements are difficult to identify and to segment, because

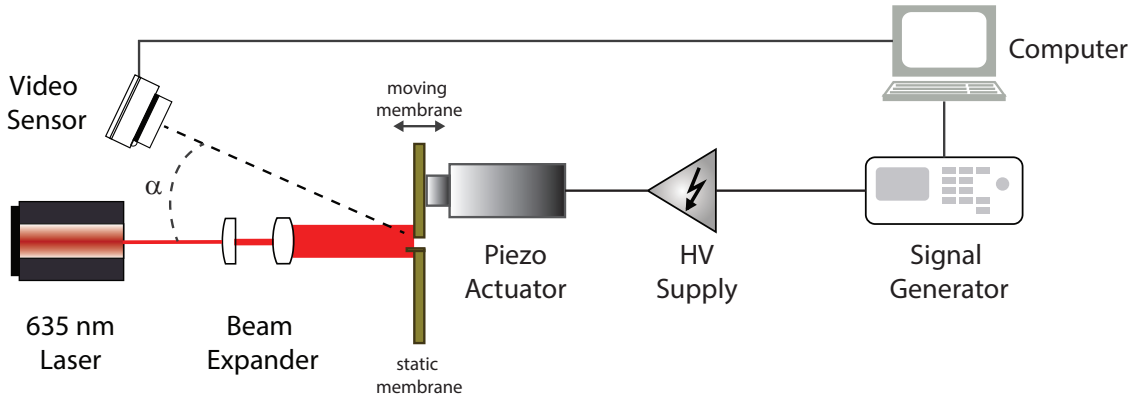

Figure 4.5: Schematic diagram of the bench test set-up for macrocirculation.

occur in a longitudinal direction and are very small. In order to solve this issue, a bench test, using speckle illumination, was constructed (Figure 4.5).

The set-up constructed has, as sample, a double membrane of silicon splitted by a gap of ≈ 3 mm. The membranes present a thickness of 2 mm. One of the membranes was connected to the piezoelectric actuator, PZA (Physik Instrumente GmbH P-287), which describes a sinusoidal movement in the longitudinal direction. The other membrane is statics and has a flap to prevent interferences by the light reflected by the moving membrane. The sinusoidal wave described by PZA is controlled and generated by a voltage signal generator, VSG (Agilent 3322A). The VSG is connected to a high voltage source, HVS (Physik Instrumente GmbH E-580), where the signal was electrically amplified to drive the PZA.

The laser light which passes through a beam expander and directly illuminates the membranes, creating a speckle pattern that varies during the membrane movement. The camera (video sensor), controlled by the host computer, records the speckle pattern in an angle, α, of $\approx 29°$.

The sinusoidal movements reproduced by the PZA are defined by its period and amplitude. The selected periods were of 1, 2, 3 and 5 seconds. Regarding the amplitudes, four values were selected, $1V_{pp}$, $2V_{pp}$, $4V_{pp}$ and $6V_{pp}$, where $_{pp}$ stands for peak-to-peak voltage. With these values a total of sixteen acquisitions were performed, one for each possible combination of the values. In the membrane movement these voltages represent four maximum displacements of 93, 187, 373 and 560 μm, respectively. The Equation 4.1 represents the transfer function of the PZA, where the maximum membrane velocity is related with the electrical signal amplitude and period.

$$V_{max}(V_{pp}, f) = \frac{700}{75} \times \frac{V_{pp}}{2} \times (2\pi f). \tag{4.1}$$

Using all possibles combinations of amplitudes and periods, 13 different maximum velocities of the membrane are obtained: 59, 98, 117, 147, 195, 235, 293, 352, 391, 586, 880, 1173 and 1759 $\mu m/s$. The acquired speckle videos, for these tests, have 7 seconds length, a resolution of 1280 x 1024 pixels, 15 frames per second (fps) and 15 ms of exposure time.

4.2.2 *In vivo*

To prove the method reliability, a simple *in vivo* test was performed. For this test, the laser light was directed to the pulse, where the artery distension is easely detected using tact. The arterial waveform corresponds to the arterial distension during blood pulsation, so the goal was obtain the time-varying speckle of this area while the distension occurs. This data was used to calculate the heart rate of the subject.

Two healthy subjects were submitted to the test discribed in Figure 4.6. For each one, three acquisitions were done. The speckle videos are obtained with a resolution of 320 x 240 pixels, 50 fps, 15 ms of the exposure time and were acquired during 20 seconds. The data was further processed and the heart rate was computed. The results were compared with the heart rate obtained by the pulse oximetry method, in order to compare the result obtained with a reliable value.

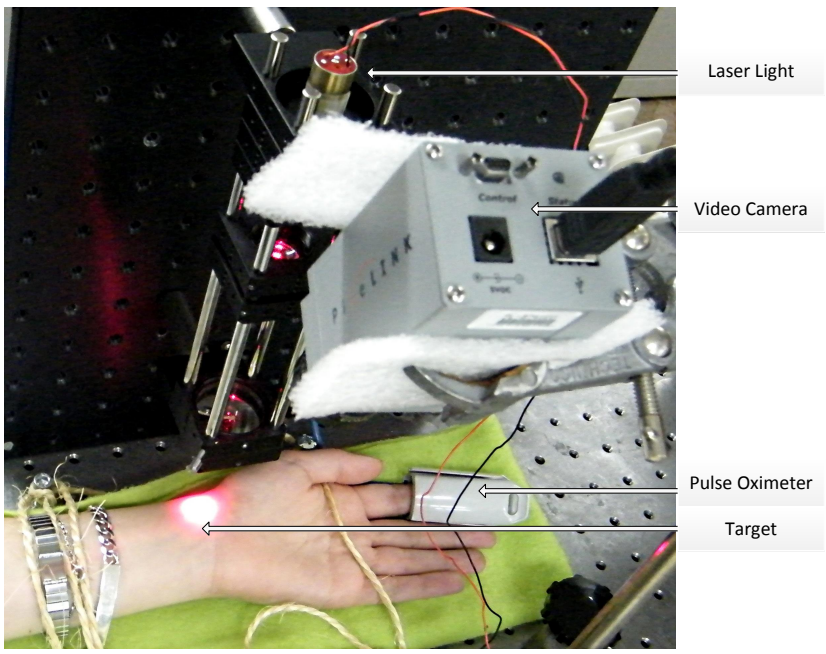

Figure 4.6: Representation of *in vivo* tests. It is composed by the laser light in vertical position, the video camera and the target (the pulse of a given subject). The pulse oximeter was used to measure the heart rate.

Since the biological system is much more complex than the utilized phantom, an increasing of the frame rate was necessary. It was selected 50 fps, in order to obtain the high information. To increase the frame rate, it was necessary to reduce the images resolution.

4.3 Microcirculation Set-up

In order to simulate the blood flow in the microcirculation, a bench assembly was used. The bench was composed by a phantom constructed and tested by Ph.D. Edite Figueiras in the Electronics and Instrumentation Group.[3] The small channel of the phantom allows the liquid to flow in a transversal moving, as occurs in the capillaries.

The distension of the tube is not necessary, like in macrocirculation tests, since only the decorrelation time of the speckle pattern, which occurs in scatter movements was studied. This pattern changing is recorded by a video camera.

Three lasers of different wavelengths, several fluid flows and several exposure times were tested in the acquisitions. After the acquisitions, three different algorithms were implemented in the speckle videos in order to obtain the contrast of them. With this data it is possible to compute the velocity of the liquid.

4.3.1 Phantom Device

The acrylic phantom (Figure 4.7) consists in two acrylic plates glued together with an interior channel with cross section of 5 x 4 mm^2. The channel extremities are connected to the latex tubes. At one end, the fluid enters and at the other end, the fluid exits. The black velvet absorbs the photons which are multi-dispersed beyond the phantom. This allows that the speckle pattern has not information of the elements which are

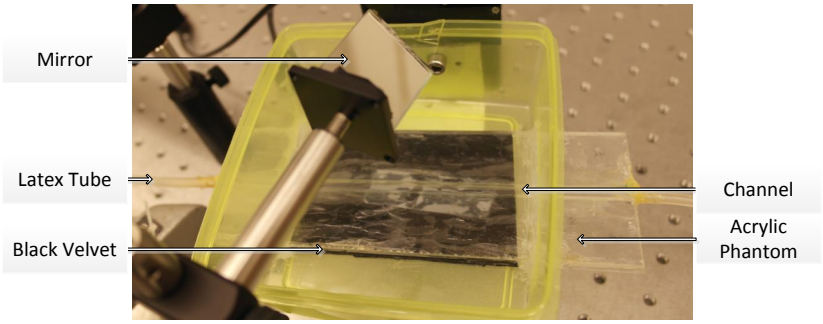

Figure 4.7: Acrylic phantom.

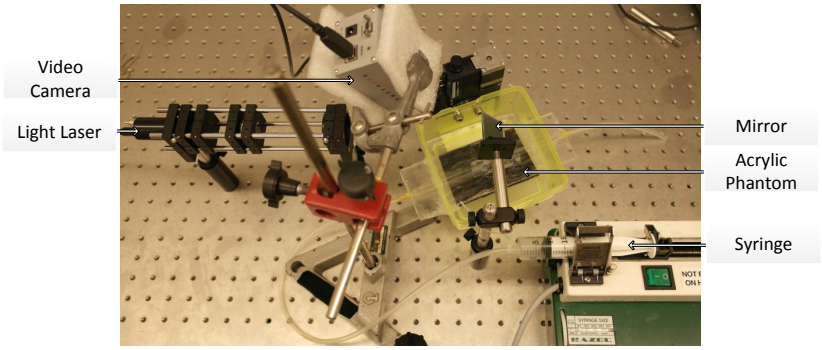

Figure 4.8: Bench assembly for microcirculation assessment.

beyond the phantom. The phantom is fixed in a rotating motor for, in future, to be tested different angles of light incidence.

4.3.2 Bench Assembly

The bench assembly for microcirculation assessment is presented in the Figure 4.8. The bench consists in a laser source, fixed in the support, which is directed to the mirror. The mirror is inclined in $\approx 45°$ (Figure 4.7), in order to the light beam to be directed to the phantom channel. The phantom is placed below the mirror.

The phantom latex tube is connected to the syringe which drains the fluid into a container to collect the waste. The syringe is placed in the syringe pump which reproduces the selected flow rates.

In the area where the laser illuminates, it is created a speckle pattern characteristic of the surface. This pattern varies along time due to fluid flow though the channel. So, when the liquid is stopped, it is expected that the pattern speckle remain the same, unlike when it flows, it is expected that the pattern changes. The camera is fixed with a claw in order to record the phantom surface.

Syringe Pump

In this work, it was used the syringe pump R99 model of the Razel Scientific Instruments. These pumps have a built in wheel style flow chart that has ninety equally spaced pump speeds from 0.25 to 143 mL/h when used syringes from 5 to 50 ml of capacity.[72] The user can select the flow rate from the chart and input the corresponding number using an analogue switch. The corresponding syringe should be placed in the claw to fix it. The top plunger of syringe is placed along the jaws and it is compressed by the movement of the threaded screw (Figure 4.9).[73] After the definition of fluid flow, the infusing can begin.

Figure 4.9: Syringe Pump Model R99-E (Razel Scientific Instruments).

Tests of Microcirculation

In this work part, many experiences were done, in order to improve the acquisitions results. For each case it was defined the laser, the exposure time, the frames per second, the resolution, the F-number and the flow rates to use. Other important point is the fluid that will flow the phantom, it must have disperser elements.

Test #1

In preliminary tests, flow rates that reproduce the velocities close to the velocity of the blood in the capillaries was used and stopped fluid (Brownian motion). The velocity of the blood is approximately 0.1 cm/s, in a capillary of 10 μm of diameter. The flow rate is defined as the volume of fluid that passes through a cross-section, during a period of time. Thus, flow rate is the multiplication of the velocity of the liquid in a compartment by the section of the compartment.

The velocities tested were 0, 0.25, 0.75, 1.00, 1.25 and 1.50 mm/s. Since, the acrylic phantom has a section of 20 mm^2 (5 x 4 mm^2), the flow rates correspondents, to input in syringe pump, are 0, 18, 36, 54, 72, 90, 108 mL/h, respectively. In this step two coherent lights, red and infra-red lasers, were tested. The video camera was set-up with a resolution of 640 x 480 pixels, a time of acquisition of 2 seconds and 20 frames per second. The exposure times were tested for each velocity. Exposure times tested were 5, 10, 15 and 20 ms. The liquid used was milk, because is a liquid very close to the blood, regarding optical properties. It is composed by proteins, minerals and water. The camera diaphragm opening (F-number) was adjusted during the experiment, in order to not saturate the speckle images. In addition, the focusing and defocusing images were tested.

Test #2

According literature, it must be used exposure times from 0.1 to 100 ms,[56] so different exposure times were tested. For the exposure times were selected the values:

0.5, 1, 2, 5, 10, 15, 30, 50 and 75 ms. More than 75 ms causes signal to saturated, even if the aperture was as close as possible. In addition, more velocities were introduced (0, 0.1, 0.25, 0.5, 1, 2, 3 and 5 mm/s). In the flow rates, they correspond to 0, 7.2, 18.0, 36.0, 72.0, 144.0, 216.0 and 360 mL/h, respectively. It was also tested the contrast when the channel is without fluid.

Test #3

In the Test #3 the speckle images were focused. The exposure times selected were 3, 4, 5, 6, 7, 8, 9, 10, 12, 14, 16 and 20 ms. The camera resolution was reduced to 320 x 240 pixels. The time acquisition was 2 seconds and were used 30 frames per second. In this step, behind the red and infra-red lasers was also tested the green laser. The velocities were the same that were used in the Test #2. The F-number also changes to maintain a good speckle pattern.

Test #4

In this stage, the selected F-number must have a value which tolerate all the exposure times, without saturating. For each laser (three lasers), the diaphragm aperture was defined. The condition of the size speckle be higher that a pixel size is fundamental. Since the speckle size is proportional to the F-number, this value was selected in order to increase the speckle size for a better result.

In previous tests, the velocities used were close to blood velocities in capillaries. In this tests the velocities reach higher values. The velocities were 0, 0.25, 1, 2, 3 and 5 mm/s. This correspond of the flow rates of 0, 18, 72, 144, 216 and 360 mL/h. The other case is with the empty core.

The exposure times have new values, in an exponential range. The exposure times values were 1.0, 1.3, 1.6, 2.0, 2.6, 3.4, 4.3, 5.5, 7.0, 8.9, 11.3, 14.4, 18.3 and 23.4 ms. More than these values there are not a F-number to cover the exposure time range without saturation of the speckle images.

The phantom was modified. In this step, a thin silicon membrane was placed upon the phantom. This allows to have a translucent element and that simulates the skin.

Chapter 5

Data Processing

This chapter presents the algorithms developed for data processing. The processing goals for the macrocirculation and microcirculation are different, so different data processing algorithms were developed to respond to the two necessities. The first one needs an algorithm that segments the speckle data obtained during the longitudinal moves of the targets. While, the microcirculation needs a data processing for speckle data obtained during a transversal movement of scatters.

5.1 Macrocirculation Data Processing

The algorithm developed uses the entropy computation to segment the speckle images, evidencing the moving spots. In the *In vivo* case, the used method is the same, but a second stage of processing was added to obtain the arterial pressure waveform and correspondent cardiac frequency.

5.1.1 Segmentation Algorithm

The developed algorithm, for temporal segmentation of speckle images, consists in two main steps: the computation of the images entropy and the its segmentation. Four different methods of entropy computation were tested.

The Figure 5.1 is a diagram of the developed algorithm, in order to understand the process that will be described. The data processing was implemented in Matlab (R2013a).

After the data acquisition of the 14 velocities of the membrane, the videos were

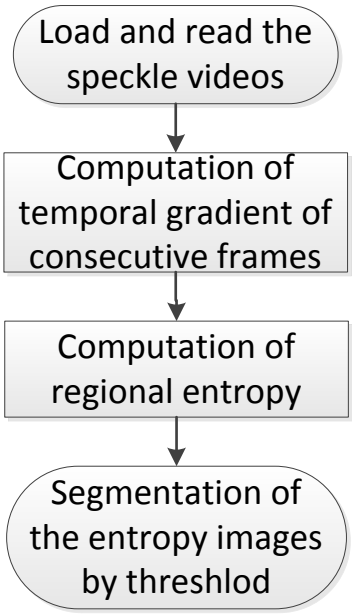

Figure 5.1: Block diagram of speckle segmentation algorithm applied in images with longitudinal motion.

load and read in Maltab. As the images are in grayscale, all RGB channels have the same value. To simplify the computation, two of the RGB channels of the matrix were eliminated. Then, the temporal gradient is computed pixel-by-pixel between two consecutive frames. In practice, the application of this gradient filter corresponds to the subtraction of two consecutive frames. This is equivalent to perform a temporal derivative, as is demonstrated in the Equation 5.1:

$$\Delta_t mov[x, y, t] \; = \; mov[x, y, t] \; - \; mov[x, y, t-1], \tag{5.1}$$

where $\Delta_t mov[x, y, t]$ is the temporal gradient obtained for a given pixel. After the gradient application, the intensities differences between the frames are evidenced. This is the effect of the application of a high-pass filter. In this step the temporal resolution is maintained, but one frame is lost, the first one.

The next step is the computation of the regional entropy of the obtained gradient images. The entropy consists in a measure of the system "disorder". A certain system has a high entropy level if its "disorder" is high.

The regional entropy (RE) of a frame is computed by selection windows (image sub-regions). Thus, for a given window size, the RE is computed by associating the entropy value to the central pixel of the window. The image overall entropy map is achieved by overlapping these windows. In each window, the correspondent histogram is computed, this mean that, a sum of the times which the intensity appears, C_{bin}, is

obtained for each gray bin. The gray bins varying between 0 to 255 bins. Then, the histogram is "normalized", *i.e.*, each C_{bin} value is divided by number os pixels of the window. The result is the probabilities distribution (P_{bin}) of gray levels (the some of P_{bin} for all bins is 1), where the RE was computed. Finally the RE is obtained by the calculus described in Equation 5.2,

$$RE = -\sum_{bin=1}^{256} P_{bin} \times \log_2(P_{bin}). \tag{5.2}$$

The RE was computed in all the gradient images and 4 windows size were tested in order to determinate the best method. The windows sizes were 3×3, 9×9, 27×27 and 81×81 pixels.

After the pre-processing stage, the images segmentation is achieved by applying a fixed threshold. The pixels where the entropy has a value above the defined threshold, are considered as motion spots (1). Contrary, the pixels with values under the threshold, are designed as stationary spots (0).

A training data-set was constructed using 12 images pairs of taken from acquired videos, 11 corresponding to the different membrane velocities and one of the static case. The described algorithm, including the 4 window sizes, were applied in this data-set, with a threshold range between 0 to 6, with steps of 0.05. The goal of this data-set was to select the best threshold.

The classification compares the pixels values given by algorithm with a manual segmented binary mask. For example, if the algorithm classifies a pixel as a moving spot, value 1 and, in the mask, this pixel is in the moving area the classifier evaluates it as a right classification, true-positive (TP). If the algorithm classifies a pixel as a moving spot, but the pixel is static in the binary mask, value 0, the classification is wrong, which leads a false-positive (FP). Other case is when a pixel, that is classified as a static spot, is also considered static in the mask, leading to a true-negative (TN). Finally, if the pixel is classified as static but in the mask the pixel is in moving area, it is evaluated as false-negative (FN). All the possibilities can be simplified by the bitwise operation:

$$\begin{aligned}
\text{TP} &= \text{BinaryMask \& AlgorithmOutput;} \\
\text{TN} &= \text{!BinaryMask \& !AlgorithmOutput;} \\
\text{FP} &= \text{!BinaryMask \& AlgorithmOutput;} \\
\text{FN} &= \text{BinaryMask \& !AlgorithmOutput,}
\end{aligned}$$

where '!' stands for logic negation and '&' stands for logic AND.

This classification of the training data-set is performed pixel by pixel for the 12 images of the data-set. The process used to rate quantitatively the classification consists in obtain the specificity (SP), sensibility (SE) and the accuracy (AC) for each image, for each applied threshold and for each window size. This measurement are computed using the sum of the confusion matrix values (TP, TN, FP, FN) along one case. SE, SP and AC are described in Equation 5.3(a), 5.3(b) and 5.3(c) respectively,

$$a)\, SE = \frac{TP}{TP+FN},\ b)\, SP = \frac{TN}{FP+TN},\ c)\, AC = \frac{TP+TN}{TP+TN+FP+FN}. \quad (5.3)$$

The method used to determine the appropriate window size was based in the construction of a receiver operating characteristic (ROC) curve. This curve represents the classifier performance as function of the applied threshold by plotting the number of true positives rate as function of the number of false positive rate, which is the same as 1-SP *vs* SE. The appropriate window size was selected as the one with high area under the ROC curve (AUC).

After the selection of the appropriate size, that method was applied to the training data with the aim to determinate the threshold that maximizes the average accuracy. To validate the obtained threshold, it is applied in the segmentation of the validation data-set which is composed by 4 videos with 4 different maximum velocities. Based on the results of TP, TN, FP and FN, the application of the best threshold is evaluated according to the values of AC, PPV (positive predictive value), NPV (negative predictive value) and MCC (Matthews correlation coefficient). These cases are described in the Equation 5.4,

$$\begin{aligned} a)\, PPV &= \frac{TP}{TP+FP},\ b)\, NPV = \frac{TN}{TN+FN}, \\ c)\, MCC &= \frac{TP \times TN - FP \times FN}{\sqrt{(TP+FP)(TP+FN)(TN+FP)(TN+FN)}}. \end{aligned} \quad (5.4)$$

The MCC measures the quality of the binary classifications, in particular when the classes weight are unbalanced. MCC returns a value between -1 and +1. A coefficient of +1 represents a perfect prediction, 0 represents a random prediction and -1 indicates a total disagreement between prediction and observation.

5.1.2 *In vivo* Improvement

Data processing for *in vivo* data is based on the algorithm applied in the bench test. Figure 5.2 explains the developed process.

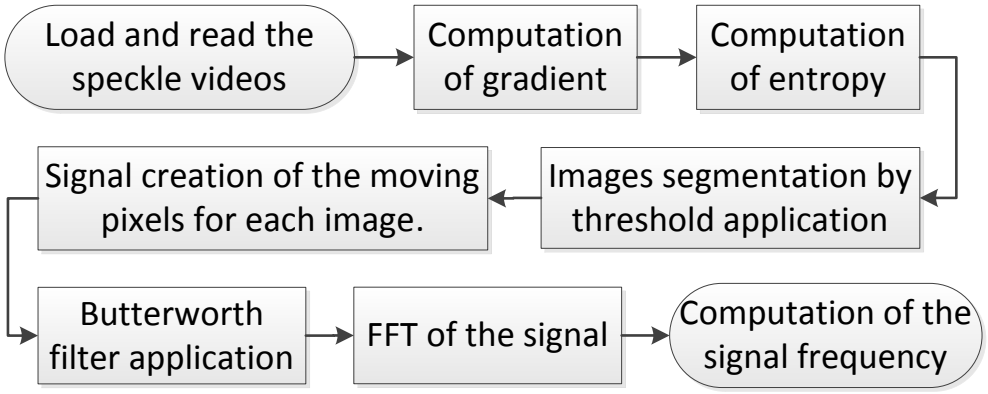

Figure 5.2: Algorithm applied in tests *in vivo* for longitudinal motion.

The best threshold was applied for entropy images computed with the selection window size. In this step, the images, that show more moving spots, have more white pixels (pixels with value 1). Thus, to know the variation of moving spots along the images of a video, the sum of white pixels is done for each image.

It was applied a butterworth filter in the obtained signal. This is a bandpass digital filter, thus allows that above some value, as well as, above a certain value, the signal is attenuated. The extreme values possibles of the heart rate, without any health complication for a subject with 25 years-old are 30 and 195 beats per minute (bpm).[8] Regarding this condition, the cutoff frequencies selected were 0.5 and 3 Hz. In minutes, these frequencies are described by 30 and 180 bpm.

In next step it was computed the fast Fourier transform (FFT) of the signal filtered, in order to obtain the the signal frequency. The FT predominant frequency corresponds to the heart rate.

5.2 Microcirculation Data Processing

The data microcirculation processing has two main steps: the video segmentation and the application of the LSCI algorithms. The segmentation allows, mainly that, when the data be processed with the algorithms, the computational effort be lower and to select regions of interest.

The applied algorithms have the goal to obtain the speckle contrast of the videos.

It were applied an algorithm of spatial contrast (sLSCI), an algorithm of temporal contrast (tLSCI) and one that combining both, the algorithm of spatial and temporal contrast (stLSCI) (Section 3.6.4).

5.2.1 Video Segmentation

The processes to do the video segmentation consists in the creation of a mask, a rectangle, and apply it, in all video frames (Figure 5.3). After the segmentation, all the frames are only composed by the area which corresponds to the region where moving scatters exist.

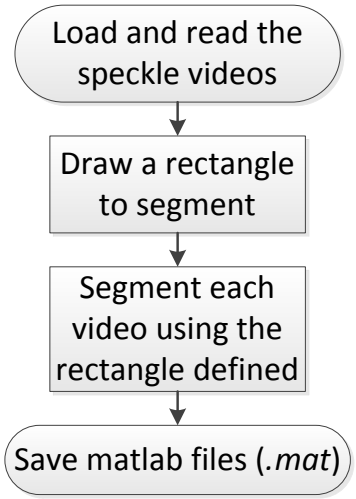

Figure 5.3: Video segmentation process.

Since the images are in grayscale, the three RGB channels have the same value. Thus, is only used one of the RGB channels.

Then, an aleatory frame is showed and the user draws a rectangle of interest, in order to select an area where is only present the illuminated phantom channel by the laser. This step is done for each laser. This procedure is necessary because the lasers illuminate different areas, although the optical configuration be the same. So, if it was used the same rectangle positions would be probably that the interest zone does not match. For each laser data the rectangle positions is defined and the segmentation is applied in the speckle videos. The segmented videos files are saved in matlab format (*.mat*).

Before the application of the LSCI algorithms it was considered to do a preprocessing of the segmented videos. According literature, it was suggest the application of high pass filters in order to eliminate some noise, increasing the performance of the contrast methods.[74] The Canny, Prewitt, Sobel, Roberts, LOG and Laplacian filters

were implemented in speckle videos for the data preprocessing. However, the contrast results with preprocessing were not satisfactory. The filters skewing the contrast values for high values. Since important information was eliminated the application of this filters was dropped.

5.2.2 Speckle Contrast Algorithms

The application of the LSCI algorithms, it the next step of processing. In the Figure 5.4 it is presented the flow chart of the process of implementation of the three methods to compute the contrast of speckle images: spatial LSCI (sLSCI), temporal LSCI (tLSCI) and spatial and temporal LSCI (stLSCI). The sLSCI method was tested with window sizes of 3 x 3 and 5 x 5 pixels, the tLSCI method was tested with window sizes of 1 x 1 x 3 and 1 x 1 x 5 tested and the stLSCI was tested with window sizes of 3 x 3 x 3 and 5 x 5 x 5 pixels (Section 3.6.4).

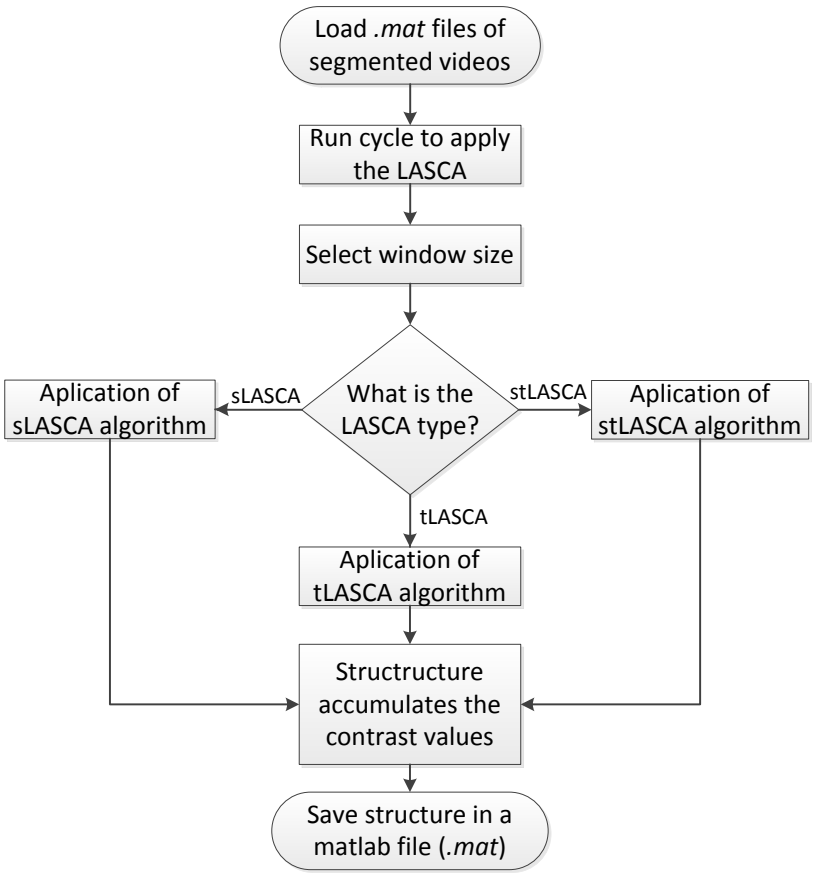

Figure 5.4: Scheme of script development for algorithms application.

The average of the contrast image was added in a structure, as well as the information about the flow rate, the laser, the exposure time, the LSCI type and the window size.

Chapter 6

Results and Discussion

Chapter 6 presents the results obtained for macrocirculation and microcirculation tests. In the macrocirculation case, the results of the bench tests and the results of the *in vivo* case are showed. A discussion and some considerations of the microcirculation tests are also presented.

6.1 Macrocirculation

6.1.1 Bench Tests Results

The Figure 6.1 shows two consecutive frames of a video acquired in bench tests with the double-membrane phantom. When the images are observed, the differences between them are not instantaneously visible. However, if temporal differences exist, the temporal gradient will show them. The Figure 6.2 (a) presents the gradient between the frames of the Figure 6.1. The existence of non zero values prove that the variation of the speckle pattern can be enhanced using the temporal gradient which evidences the zone of the left membrane. It is also possible to observe a small image coefficient in the right membrane zone, maybe due to the mechanical interference of the PZA in the membranes support or light reflection.

The Figure 6.2 (b) is the result of the regional entropy computation of the image gradient (Figure 6.2 (a)) where it was used a window size of 27 x 27 pixels. As expected, the regions where the membrane is moving show higher entropy compared to the static zone, where the entropy is lower. The entropy image showed in pseudo-color allows the variations visualization with better perception.

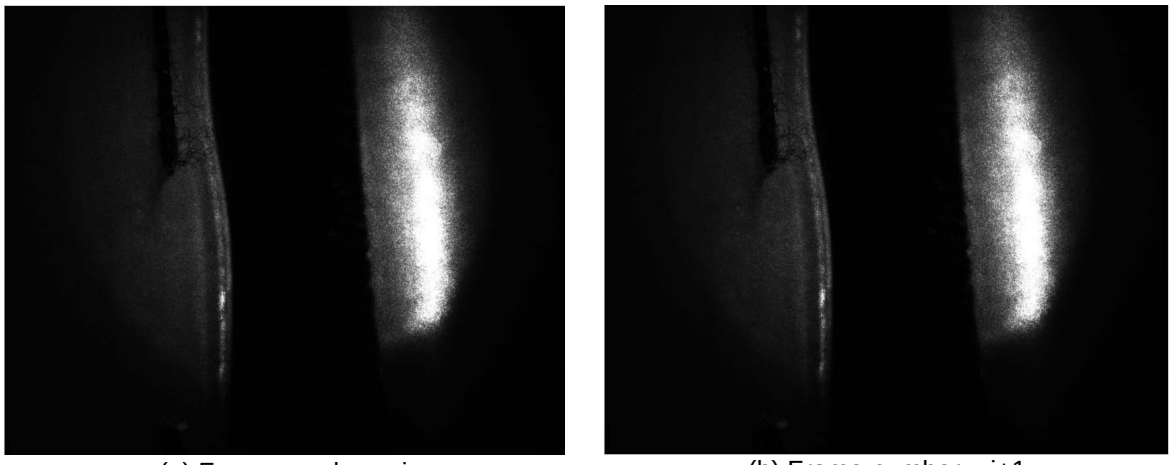

(a) Frame number = i (b) Frame number = i+1

Figure 6.1: Speckle images of the double membrane phantom. In these consecutive images, the left membrane is moving with the velocity of 59 μm/s with a sinusoidal movement of 1 second period and 1 V_{pp} amplitude. In each image, in the left is the moving membrane and in the right is the static membrane.

It is important to refer that, ideally, the entropy in the left membrane should be higher in all moving zone, but the laser light is not uniform along it. The laser light is directed to the two membranes, but cover only the image centre, as it is possible to observe in the original images of Figure 6.1. Other important point is the absence of speckle effect in the separation of the membranes. This happens because the background material (black fibre) absorbs the photons.

In the training, it data-set was used 12 speckle videos corresponding to 12 different maximum membrane velocities of 0, 59, 98, 117, 147, 195, 235, 293, 352, 586, 880 and 1763 $\mu m/s$. The entropy was computed for each image using 4 distinct methods: different windows sizes. The binary segmentation was achieved using a numerical threshold. For the classification evaluation, it was drawn a manual binary mask (Figure 6.3 (a)), corresponding to the moving zone, that was compared, pixel-by-pixel, with the classification obtained during segmentation. Figure 6.3 (b) shows the output segmentation of the algorithm applied to the image of the Figure 6.2 (b), when a threshold of 2.95 was used. The white points are the pixels classified as moving spots, in contrast with the black pixels, which represent static points.

The manual binary mask (Figure 6.3 (a)) was drawn taking into account the non uniformity of laser illumination over the membrane and the vertical line in left membrane, visualized in entropy image (Figure 6.2 (b)). This line corresponds to the fixation material of the membrane, which was considered as a stationary spot, due to its light absorbence properties.

The Receiver Operating Characteristic (ROC) curves were computed to find which

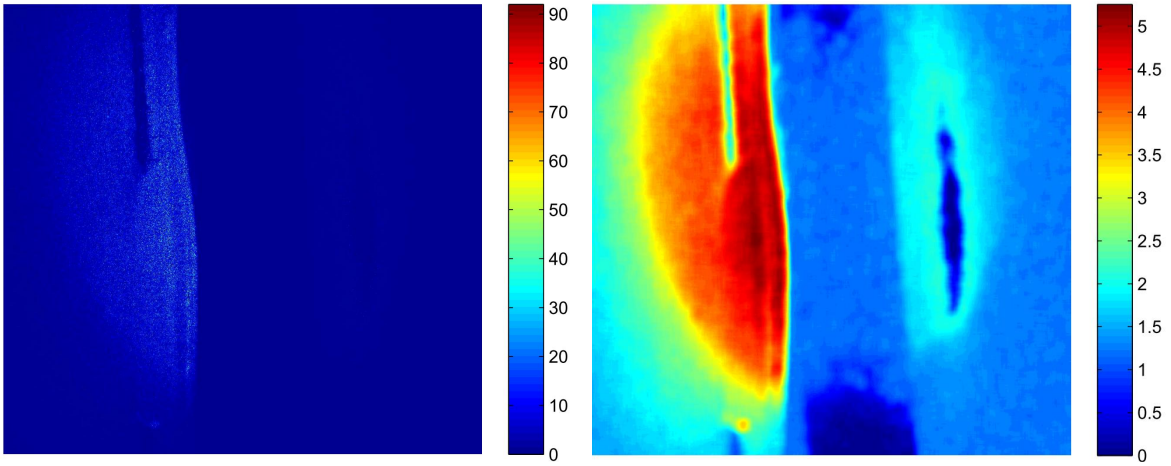

(a) Temporal Gradient (b) Entropy Image

Figure 6.2: Pre-procesing of the speckle images of the double membrane phantom presented in Figure 6.1. (a) Application of temporal gradient. (b) Computation of regional entropy with a windows size of 27 x 27 pixels, represented in pseudo-color.

one is the best window size. The graphic results of the ROC curves, obtained for each method, are present in Figure 6.4. The blue, black, green and red lines are the ROC curves for the methods where the regional entropy is computed using the windows sizes of 3 x 3, 9 x 9, 27 x 27 and 81 x 81 pixels, respectively. When the threshold is 6, no pixels are considered as moving spots, so the sensitivity is zero. In this case, the specificity is maximum (SP=1) because there are not statics pixels considered as moving pixels. Contrary, when the threshold is 0, all the pixels are classified as moving points, so the sensibility is maximum (SE=1), but the specificity is zero, because any static pixel is considered as such.

The performance of the four regional entropy computation methods is obtained by computing the area under the ROC curves (AUC). The results are presented in the Table 6.1. All methods are above 0.90, so the four windows sizes used are excellent methods to perform the laser speckle image classification. The best method is the #4, of 81 x 81 pixels, where an AUC of the 0.9901 was achieved.

Table 6.1: Results of the AUC of the 4 entropy computation methods.

Method #	Window Size	AUC
1	3 x 3	0.9286
2	9 x 9	0.9779
3	27 x 27	0.9879
4	81 x 81	0.9901

The computational effort of the methods is a feature important to consider. The computational effort considering the windows size, can be expressed by the relation

(a) Manual Binary Mask. (b) Algorithm Classification Output.

Figure 6.3: Binary images of the scene. (a) Manually segmented moving zone (binary mask). (b) Result of the application of segmentation algorithm, of Figure 6.2 (a), with the threshold of 2.95.

n^2, where n is the window length. Thus the method #4 is nine times longer than the method #3.

Despite of the method #4 presents a better performance, the computational effort of the entropy algorithm is very high. The difference in the performance between this two methods, 0.0022, does not justifies the computational effort required to the method #4. By this reason, the method #3 was considered the more appropriated one.

Using the best method (#3), it was selected the best threshold from 0 to 6. In Figure 6.5, it is represented the accuracy obtained for the application of a given threshold, in the 12 training images pairs, corresponding to 12 different maximum velocities (represented with different colors line). For each threshold, it was calculated the average of the accuracy obtained for the 12 velocities (thicker blue line). The threshold that maximize the mean accuracy was 2.95, with the value of 95.8%.

The complete identification and segmentation algorithm (method #3, threshold, 2.95), was applied in the validation data-set, composed by 4 videos with distinct membrane velocities. The results of the evaluation metrics to validate the method are present in Table 6.2. The results of AC range from 92% to 97%. This small range shows that the classifier is balanced.

The data classes are unbalanced, there are 118 millions of negative points (stopped) and 25 millions of positive points (moving), approximately. Thus MCC is a better method to evaluate the performance of the classifier. It varies between 0.72 (data #1) to 0.91 (data #10). Despite of small number of videos used to validate the method,

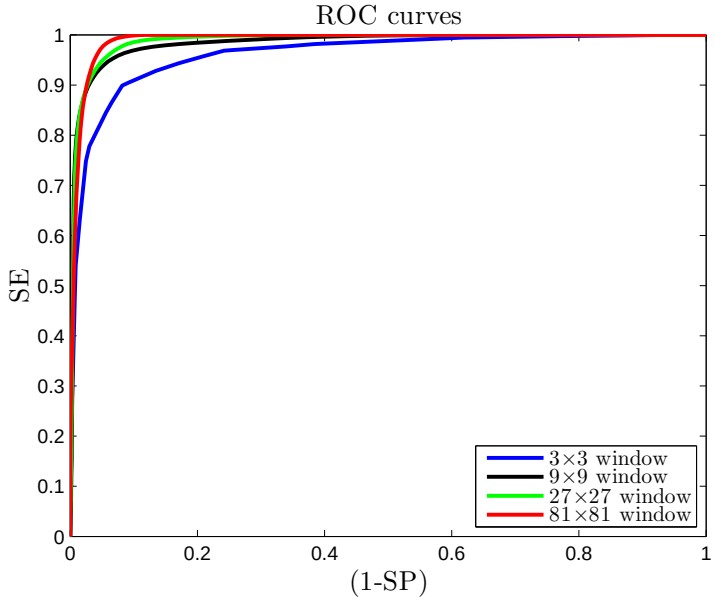

Figure 6.4: ROC curves for best method identification. SE is the sensibility and SP the specificity of the method.

it is possible to observe the tendency for better classifications of videos with slowest movements (the best result was for the velocity of 391 $\mu m/s$), with the exception of data #1, where the velocity is the smallest. This happens due to the necessity of increase the frame rate of the acquisitions when the moving object has a higher velocity.

Table 6.2: Results of data-set validation for windows size 27 x 27 pixels and the threshold of 2.95.

data #	AC (%)	PPV (%)	NPV (%)	MCC	V_{max} ($\mu m/s$)	Frame Number
1	91.82	74.99	95.49	0.72	293	16
10	97.01	88.19	99.22	0.91	391	46
3	94.83	78.24	99.55	0.85	586	31
12	93.33	70.56	99.92	0.80	1173	16

The PPV and NPV results show that the NPV has always higher values. This means that there are more cases of a correct classification of a static pixels than a correct classification of moving pixels. Thus, a negative class (0) classification is more reliable that a positive class (1) classification. About NPV the results shows a stable performance for lower and higher velocities. Again, the data #1 is an exception which lead us to the conclusion that this videos was acquired with miss alignment.

It is difficult to define the limits of the moving area. So, as default, it was considered a small area, excluding all static points of this area. This does an underestimation of the moving spots. When this is done, it is normal that all static pixels are correctly classified, which means that the mask does not include all of the moving points. A

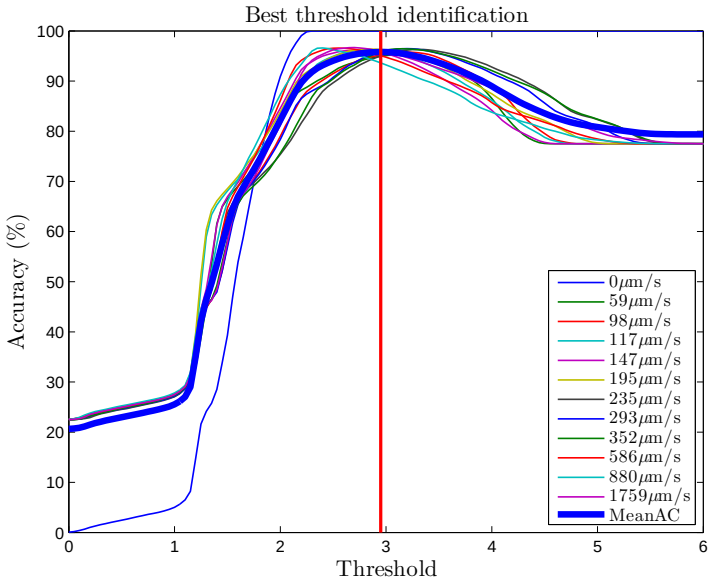

Figure 6.5: Best threshold identification for the training data-set, using 27 x 27 pixels in entropy computation for each velocity. The accuracy is represented according the threshold used. Red vertical line intersects the maximum of the accuracy average line (thicker blue line), this point represents the best obtained threshold, 2.95.

correct determination of the mask will increase the true positives, improving the results of AC, PPV and MCC.

6.1.2 *In vivo*

For the acquisitions *in vivo*, two persons (3 times each one) it was used the best method and the best threshold obtained in the bench tests. The segmented videos allowed to observe a variation of the motion area (white area), that is repeated in time. The solution to determinate this time period is to sum the number of white pixels presented in each video frame. The sum along the time, can be visualize as a signal (Figure 6.6 (a))). If there is a period, the FT of this signal will present a dominant frequency, which represents the heart rate.

In Figure 6.6, it is showed the result for the person #2, in the 3^{rd} trial. The Figure 6.6 (a) presents the signal of moving pixels count during the acquisition. The periodicity is easily visible in this signal. A very interesting point is the arterial pressure waveform, that is perceptible in some regions of the signal. In the Figure 6.6 (b) it is shown the FFT correspondent to the signal. The dominant frequency, in this case, is 1.1 Hz, which corresponds to 66 beats per minute.

The results of heart rate obtained in six acquisitions are presented in Table 6.3. In

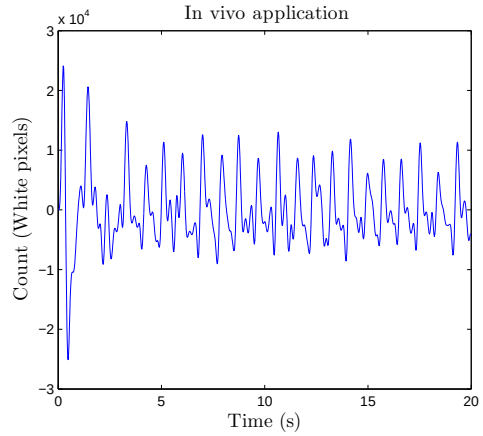

(a) Signal of moving pixels counting during acquisition.

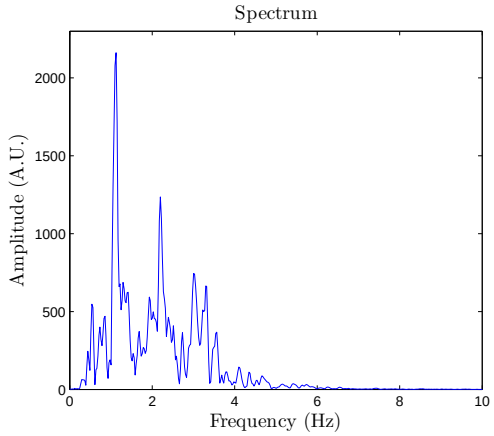

(b) FT correspondent to the signal.

Figure 6.6: Signal and FT of the 3^{nd} *in-vivo* trial of the Subject #2.

the same table, it is presente the difference of the obtained and expected results.

Table 6.3: Theoretical and obtained results of Heart Rate (HR).

	Subject #1			Subject #2		
	Trial #1	Trial #2	Trial #3	Trial #1	Trial #2	Trial #3
Real HR (R) (bpm)	62.26	64.09	65.92	62.20	67.75	67.75
Estimated HR (E) (bpm)	30.76	57.13	65.92	61.52	67.39	67.39
Difference (R-E) (bpm)	31.50	6.96	0.00	0,68	0.36	0.36

Observing the results, the acquisitions of the Subject #2 have the heart rate (HR) with less error comparing with the Subject #1. The maximum difference of HR obtained was 31.5 bpm for Data #1 of the Subject #1. Between six acquisitions, this is the single discrepant result.

The best result was obtained for the Trial #3 of the Subject #1, the difference between the heart rates was lower than the lower scale (0.01 bpm). This suggests that the developed method has a high performance and very satisfactory results.

6.2 Microcirculation

The speckle images were precessed in order to obtain the contrast of the speckles images and, consecutively, compute the velocity. The graphic results, are only presented for a few velocities in order to simplify the visualization.

The preliminary testes, Test #1 and Test #2, allowed to achieve some important considerations about the acquisitions. It is better to acquire the speckle images using focused images. When focused images are used, the visualization of the anatomical structures is more easy. This was also observed when speckle images were acquired with the channel phantom.

The contrast (C) decreases when the exposure time (T) increases because there is an integration of the received photons during the image acquisition. So, when the integration time is long, the image becomes more blurred. According to this principle it is expectable that the curve of the C *vs* T to be descending. In Test #2, it was tested T until 75 ms. The results showed that for exposure times above 20 ms, approximately, the contrast remains constant. Thus, T above it, does not give information for velocity computation, when this hardware and optical configuration is used.

In the Test #3, the exposure times range from 3 to 20 ms, the number of acquisitions increased in order to have more information in this range. The Figure 6.7 shows the graphic results of C *vs* T. In this case, it was applied the sLSCI method with a window size of 5 x 5 pixels. It is presented the contrast speckle when the channel is empty (V=-1), when the liquid is static (V=0) and when it has a velocity of 1 mm/s (V=100). The results for all tested velocities are present in Figure A.1.

Observing the Figure 6.7, the results obtained are not according with the theory. In certain values of T, the contrast increases instead of decrease. However, for the three laser types, it is notorious a profile of the velocities curves. All of them increasing in the same T. It was verified that the T values where the contrast increases coincide with the acquisitions in which F-number was changed, in order to decreasing the diaphragm aperture. In practice, when we decrease the diaphragm aperture, we are reducing the number of photons that reach the detector. If a frame is created by less photons, the blurring effect decreases, so the contrast increases and the specle size is changed.

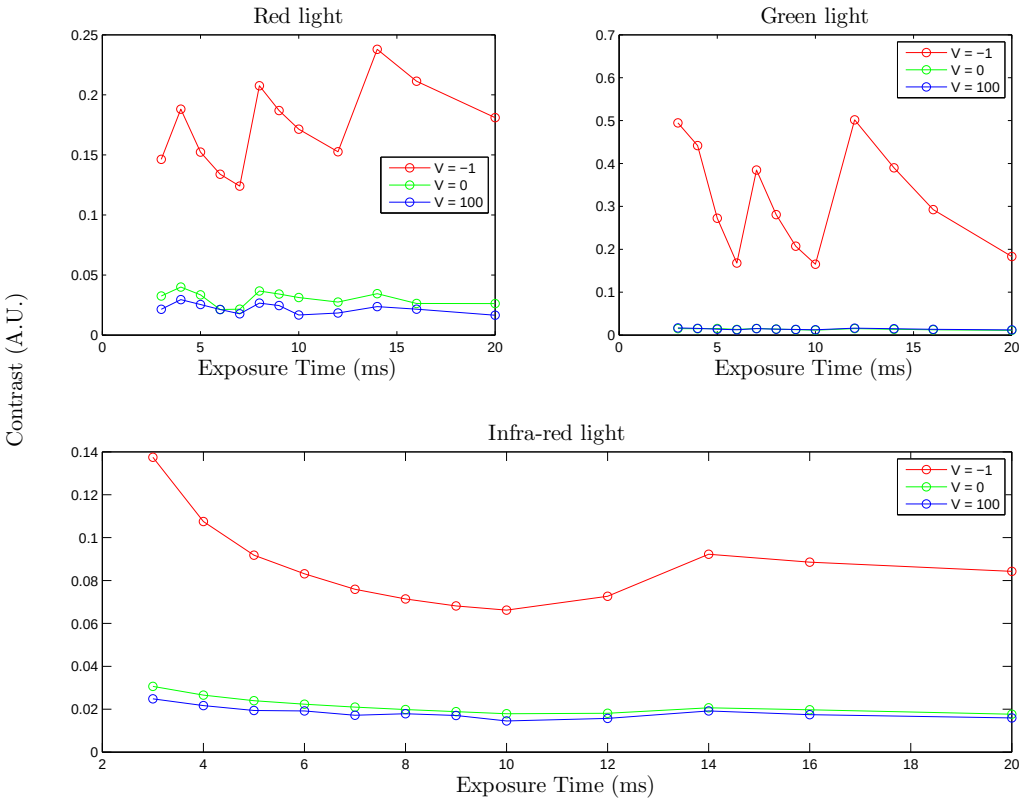

Figure 6.7: Graphic results of microcirculation, Test #3. *C vs T* for the 3 lasers used, when is applied the sLSCI method with a window size of the 5 x 5 pixels.

Regarding the velocities, the high contrast obtained when the channel is empty (V=-1) is notorious, compared with the contrast obtained when the channel has the liquid. This is explained by the lack of scatteres elements to contribute for image blurring. Furthermore, when the velocity increases the contrast deceases. This is applied in the analyse of the red and infra-red lasers. Still, in the green laser, this is not true. The V=0 reaches values lower than some velocities and it has values very close to the V=100.

Using the same parameters that were used in the test #3, in Figure 6.8, the relation of speckle contrast with the velocities, for three exposure times, 3, 8 and 20 ms is presented. The results for all exposure times are presented in Figure A.2.

In the results it is possible to confirm the decreasing of the contrast when the velocity increases. Regarding the exposure times, it is expected that higher exposure times reach lower contrasts. This is more clear when the IR laser is used. In the others lasers, there are fluctuations in relation of the expectable.

In the Test #4 a fixed F-number was applied. So, it was necessary to find the better

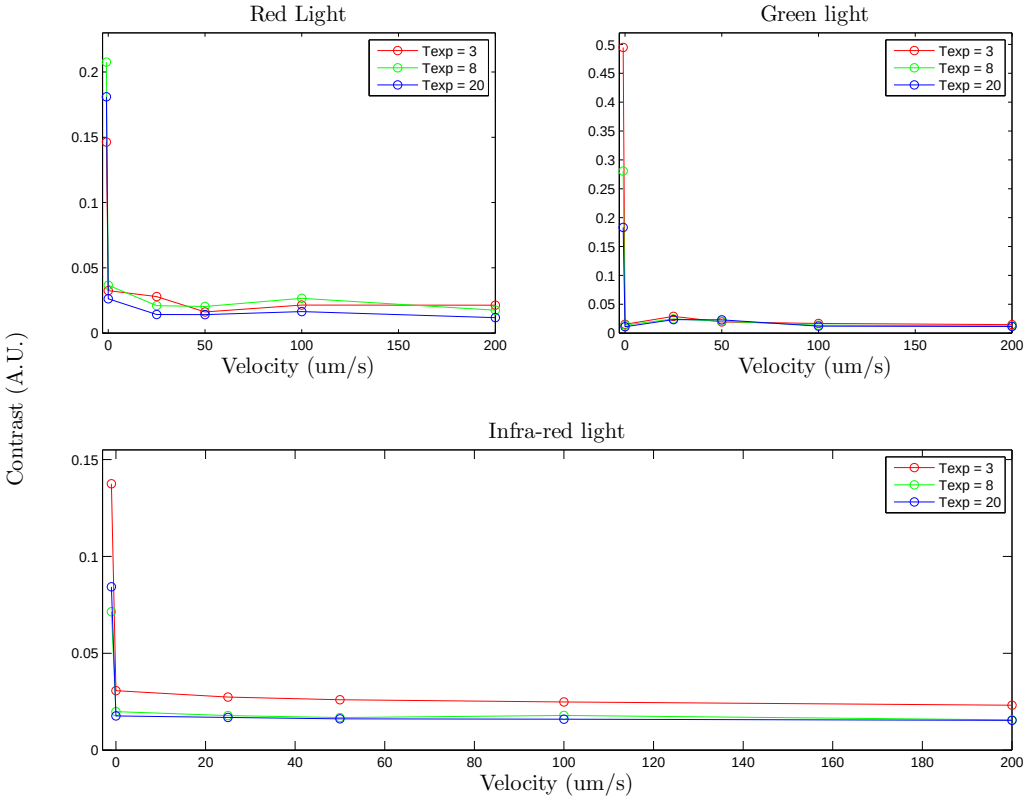

Figure 6.8: Graphic results of microcirculation, Test #3. *C vs V* for 3 exposure times. The Contrast was computed by sLSCI method with a window size of 5 x 5 pixels.

F-number to use for each laser. It need to cover the T range, without the speckle image saturation. By observation, a F-number of 16, was selected as suitable for all lasers.

The obtained results in this test were analysed graphically. It was intended to compare the C for the three LSCI methods when the windows sizes of 3 x 3 or 5 x 5 pixels were used. Once, this mean to have many graphs, in the chapter only the C *vs* T for sLSCI, the C *vs* V for sLSCI and the C *vs* T for the 3 LSCI methods when the contrast were used. The velocities presented are for is empty channel (V=-1), when the liquid is stopped (V=0) and when the liquid is moving with 200 mm/s (V=200).

The Figure 6.9 shows the graphic results of the C *vs* T when the sLSCI method using the window size of 3 x 3 pixels is applied. For the same case, it is presented in the Figure 6.10 the graphic results when a windows size of 5 x 5 pixels is used. It is expectable that the behaviour of the curves being the same, however the C obtained is different. Observing the results, when it is applied a larger window size, the C values increase. This results of the contrast computation with higher neighbour, increasing the probability of there are higher differences between the pixels. So the standard

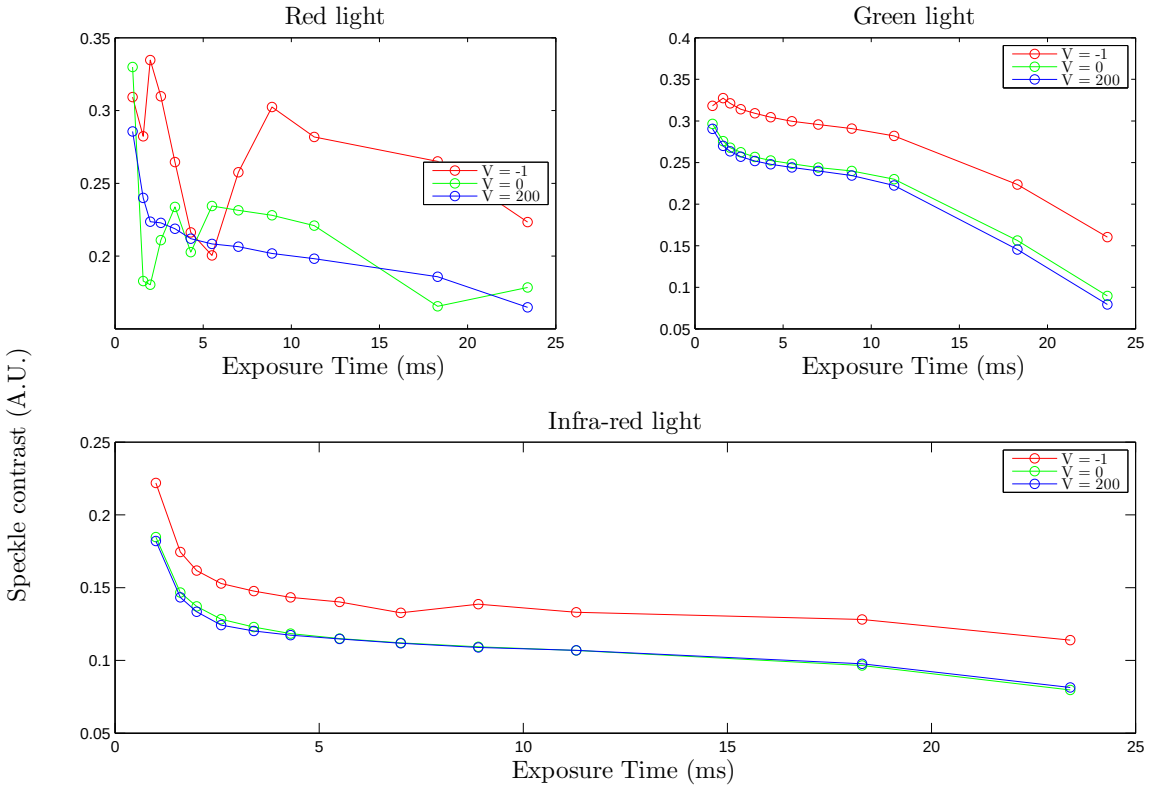

Figure 6.9: Graphic results of microcirculation, Test #4. C *vs* T for the 3 lasers used, when it is applied the sLSCI method with a window size of the 3 x 3 pixels.

deviation increases and the resultant C value increases.

In the Figure 6.11, it is presented the C evolution, for the three exposure times, when the velocity increases. The contrast was obtained by the sLSCI method, using a windows size of 5 x 5 pixels. Although there are some oscillations, the results show a decreasing of the C when the velocity increases. For higher T, the C decreases due to the increasing of the blurring effect. It was expectable that the decreasing curve was uniform, but the results suggests that, when the liquid is stopped (V=0), the contrast is lower than the contrast when the liquid is moving.

In the Figures 6.12 and 6.13 are presented the graphic results of C *vs* T when the contrast is computed by the tLSCI and stLSCI methods, respectively, using a window size of 5 x 5 pixels or 5 x 5 x 5 pixels for the stLSCI case. Comparing these techniques and the sLSCI (Figure 6.10) for the three lasers is possible to do several comments.

The presented peaks in certain T values, in Test #3, are no more in this tests. This proves the requirement to maintain the same F-number during acquisitions in order to achieve conclusions about T variations. The relation C *vs* T is according the theory. The C decreases when T increases, this is clear in this graphs.

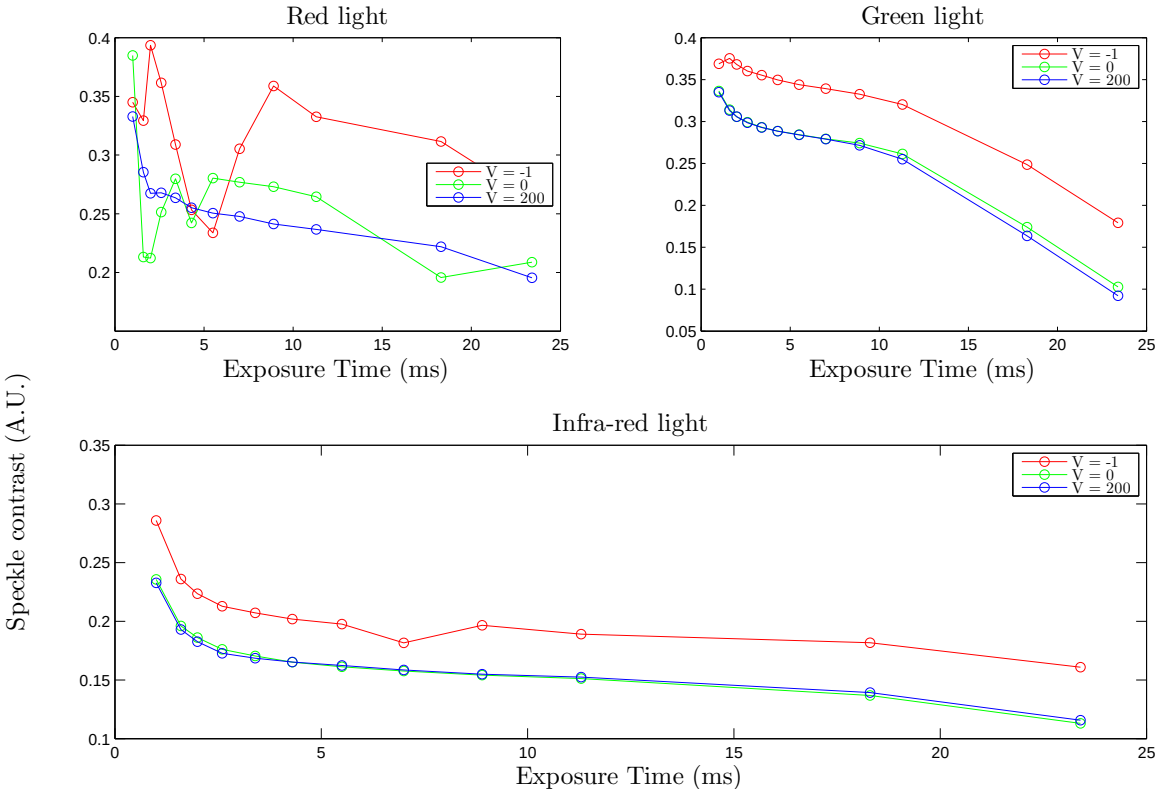

Figure 6.10: Graphic results of microcirculation, Test #4. *C vs T* for the 3 lasers used, when is applied the sLSCI method with a window size of the 5 x 5 pixels.

The sLSCI and stLSCI methods have a similar pattern, in contrast with the tLSCI. When the tLSCI method is applied, the results have the expected behaviour, a constant curve. However, when the channel is empty (V=-1), the contrast achieves the lower results of the C, comparing with other velocities. The reason is that, during the acquisitions of V=-1, the detected photons are only scattered by the phantom structure. Once, there is not time varying speckle, the pixels have the same value in all the frames, so the standard deviation is close to the zero and C decreases. The C values, obtained for V=0, have maximums close to the 0.25, 0.12 and 0.14 A.U. for red, green and infra-red lasers, respectively.

The sLSCI and stLSCI patterns, when the channel is empty (V=-1), the obtained C values are above of the other velocities, so they have higher C. However, when the sLSCI and stLSCI methods are applied, the results of red laser fluctuate greatly. When the sLSCI method is applied, the C values, obtained for V=0, have maximums close to the 0.4, 0.4 and 0.3 A.U. for red, green and infra-red lasers, respectively. When the stLSCI method is applied the obtained values are close to the 0.5, 0.48 and 0.42 A.U. for red, green and infra-red lasers, respectively. Observing the results, the method which reaches higher C values is the stLSCI, contrary the tLSCI which achieved very low contrasts. Between lasers, the red laser presents higher C values.

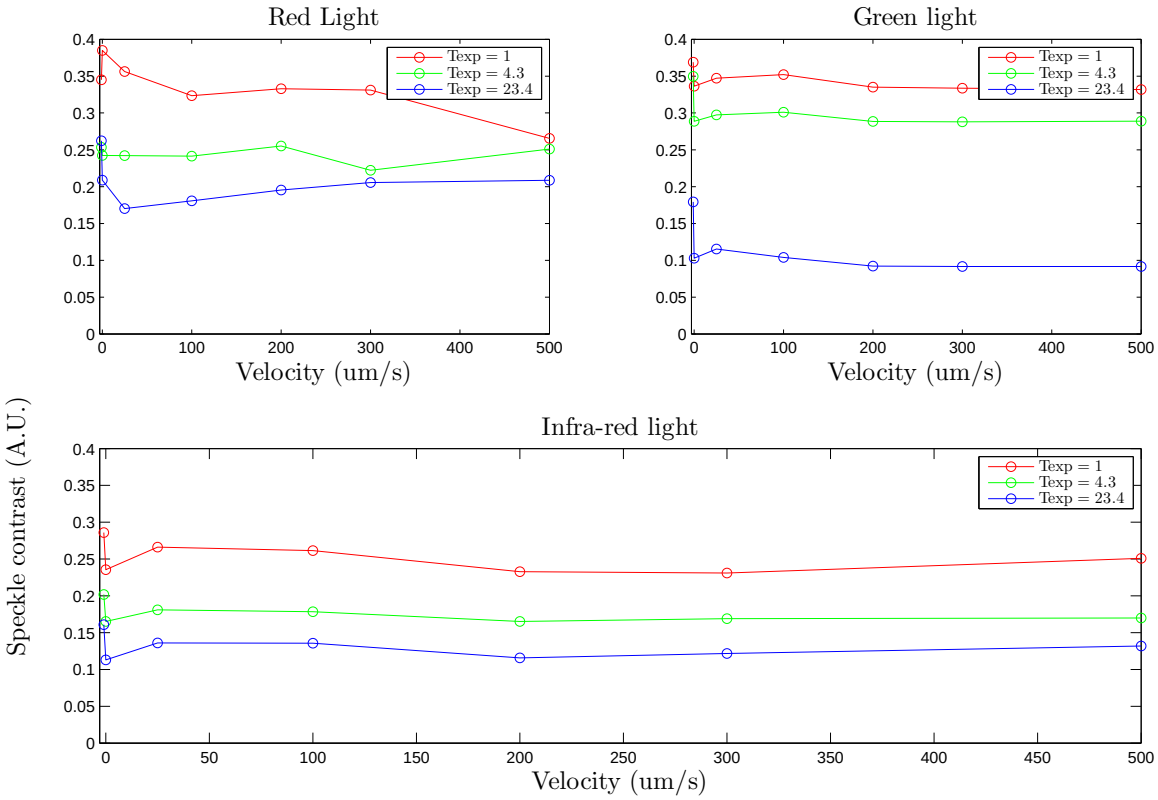

Figure 6.11: Graphic results of microcirculation, Test #4. C *vs* V for the 3 lasers, when it is applied the sLSCI method with a window size of the 5 x 5 pixels.

There are not a justification that explains the C fluctuations, in V=0 and V=-1 for the red laser, when C is computed using sLSCI or stLSCI methods. A hypothesis was formulated. The red laser is very unstable, when the laser is turned on, it needs some time for the speckle pattern to stabilise, however until the laser warm up some unwanted speckle variations are observed. This is due to some noise type that we can not identify, however somehow, the tLSCI is more immune to it. The fluctuations are visible for lows exposure times, this suggest that there is variability of the signal-to-noise ratio and that it is dependent of the exposure time. When the exposure time is low, less light is detected, so the noise overlaps the signal. When the exposure time increases, the detected light also increases leading to a better signal-to-noise ratio. In addiction, the comparison with the other lasers, for this question, it is not viable because they have different optical powers and it is not known how the membrane interacts with the different wavelengths of light.

Several considerations are important to do. The green laser would be the laser with the higher contrast and the infra-red would have the one with lower contrast. The 3 lasers reach different depths, for lower depths the photons scattering effect is lower, so the blurring effect is also lower. Still, the polarization, coherency and the maximum

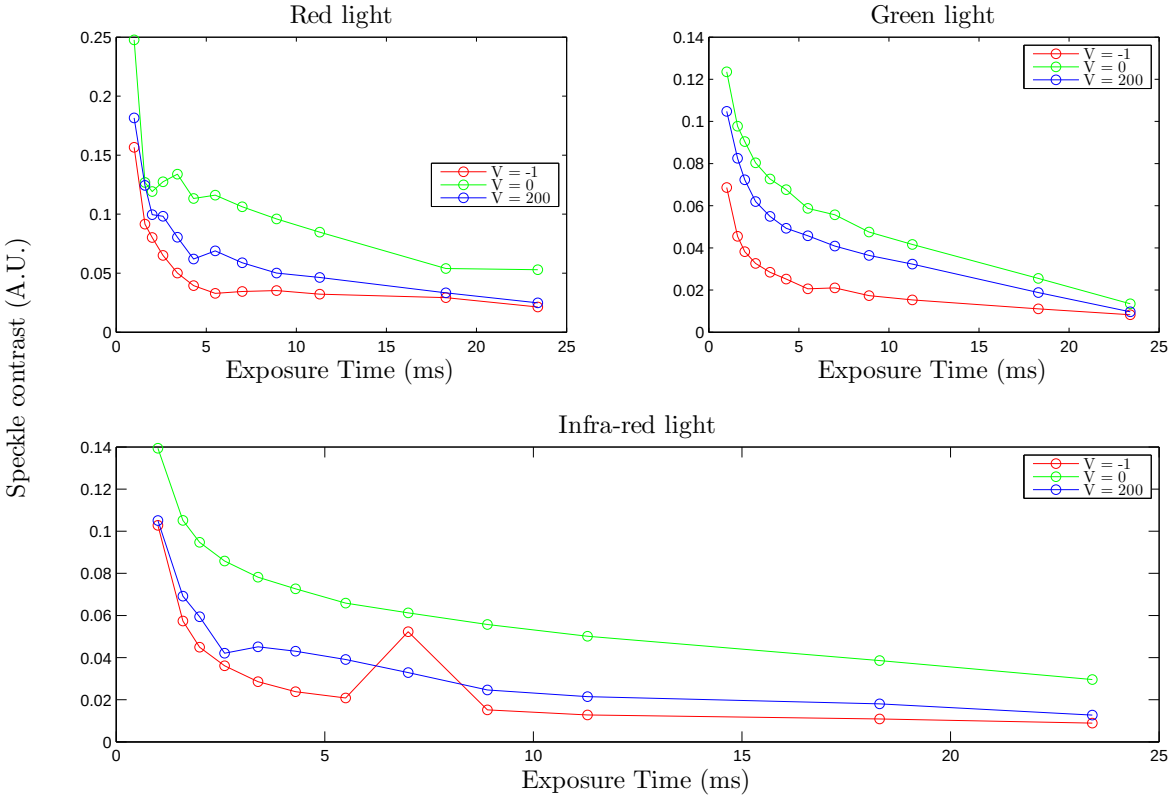

Figure 6.12: Graphic results of microcirculation, Test #4. *C vs T* for the 3 lasers used, when is applied the tLSCI method with a window size of the 5 x 5 pixels.

laser irradiance between the lasers are different. This does not allows to reach relevant comparisons. However, it is notorious the better results when the green laser is used.

It is important to refer that the fluctuations of the speckle pattern during acquisitions, due to the lasers heating. This was more visible during red laser acquisitions. Furthermore, not all of acquisitions were done in the same day, consecutively the laser alignment was different.

To obtain the velocities of the liquid the Equations 3.2 and 3.3 must be used. Since the results were not reliable, the application of the velocity algorithm will be applied in the future. It is necessary to improve the actual method and the acquisitions. Regarding this issues, the 3 methods only will be evaluated in a next step.

The completed graphic results of the microcircultation tests are present for consulting in appendix. In the Figures B.1 and B.2 are present the obtained C values of all velocities, when the sLSCI method, using the window size of 3 x 3 pixels is applied . In the Figures B.3 and B.4 the obtained C values of all velocities, when it is applied the sLSCI method, using the window size of 5 x 5 pixels are present. In the Figures B.5 and B.6 the obtained C values of all velocities, when it is applied the tLSCI method, using the window size of 3 x 3 pixels are present. In the Figures B.7 and B.8 the obtained

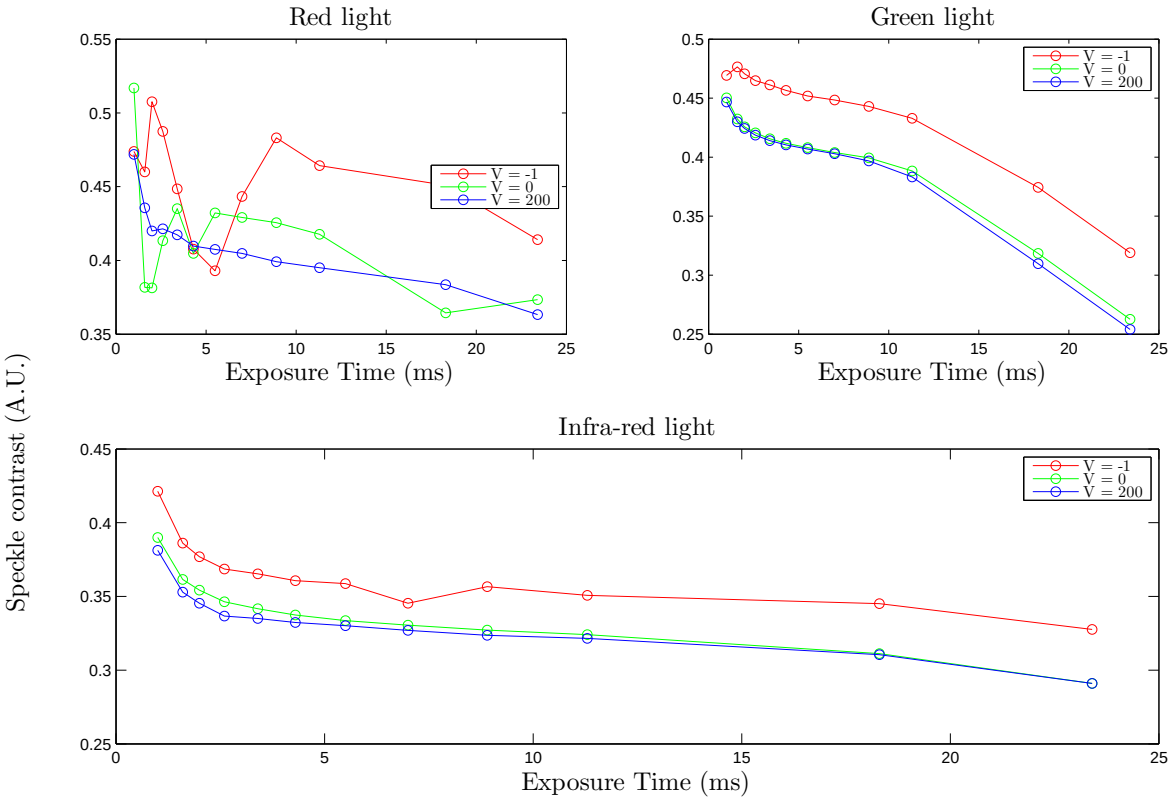

Figure 6.13: Graphic results of microcirculation, Test #4. C *vs* T for the 3 lasers used, when is applied the stLSCI method with a window size of the 5 x 5 x 5 pixels.

C values of all velocities, when it is applied the tLSCI method, using the window size of 5 x 5 pixels are present. In the Figures B.9 and B.10 the obtained C values of all velocities, when it is applied the stLSCI method, using the window size of 3 x 3 x 3 pixels are present. In the Figures B.11 and B.12 the obtained C values of all velocities, when it is applied the stLSCI method, using the window size of 5 x 5 x 5 pixels are present.

Chapter 7

Conclusions

In this project a methodology based on speckle effect to extract hemodynamic parameters that allows the assessment of the macro and microcirculation was developed.

In the macrocirculation, the system of optical configuration and the algorithm developed works well, either in bench tests or *in vivo*. In the bench tests a bidimensional segmentation was done by applying a regional entropy computation of the speckle images. The more appropriate method for regional entropy computation is the method #3 (27 x 27 pixels). The best threshold for the segmentation is 2.95 with a accuracy of 95.8 %. The validation of this method obtained a maximum accuracy of 97 %. Once, the classes are unbalanced, the best indicator to assess the method is the MCC index. The maximum MCC obtained is 0.91, for data #10, where the maximum velocity is 391 μm/s. This result is very satisfactory, it mean that the majority points were predicted very well.

For the *in vivo* trials two healthy subjects were assessed. In this videos, the heart rate was identified easily. The algorithm applied in bench tests was also applied in *in vivo* tests with the selected method and threshold as being the best parameters for longitudinal moving segmentation. The signal extracted from segmentation allowed to compute the heart rate, using a simple filter, very close of the heart rate obtained with the oximeter. Furthermore, the arterial pressure waveform is identified clearly in some signal fragments.

In the microcirculation tests the results are not as satisfactory. The goal of the fluid velocity computation was not accomplished. The graphics do not present a good behaviour to compute the velocity and to assess the methodology implemented in this project part. The experiences allowed to verify the relation between the C and T as well as with the V. When the T increases the C decreases as was expectable, this also

is verified when the velocity increases. It was also observed a T range of the 1 to 23.4 ms, favourable to do the acquisitions without image saturation and, for the high T, it is realized the C stabilization.

The diaphragm aperture influencing the speckle contrast. When it is increased, the contrast increases, so must be used a F-number fixed for each laser. The window size has a limited influencing. As was observed the behaviour of the curves is the same, either when a window size of 3 x 3 or 5 x 5 pixels are used. The red laser has a problem of optical power stability. The best results were obtained when the green laser are used.

Lastly, the signal is sensible to the noise, when is applied the spatial processing methods (sLSCI and stLSCI), in speckle images obtained from red laser. The tLSCI presents more stable data, however was noted the low C when the channel is empty. This is due to the constant speckle signal that will have a standard deviation of zero along the time.

This project allowed to achieve the know-how about optical techniques and image processing necessary to develop the algorithms to extract information in speckle images. Moreover, during experiences it was necessary to redefine the optical configuration to solve the found issues.

Future Work

Although the achieved results of macrocirculation are very satisfactory, should be done some improvements. In the data processing *in vivo* the filter cutoffs can be enhanced at the possible frequencies range. The maximum frequency used, is 3 Hz (180 beats per minute), but in real, this maximum frequency can be reached high frequencies, as 3.25 Hz (195 beats per minute for a subject with 25 years-old). The algorithm must be improved in order to extract an arterial pressure waveform more feasible. This will allow to assess also the wave according its form, which gives information about the arteries state. Furthermore, more acquisitions will be done to prove the algorithm performance and to allow its validation.

In the microcirculation, the performance of the algorithms can be improved and, mainly, the hardware and phantom device. The phantom channel must have a lower cross-section, like occurs in the microcirculation. The lasers used are not very stables, in particular, the red laser. This commits the results. Along the acquisitions the lasers warm up, so in the future must be used a lasers thermal stabilizer to correct the

artefacts arising out of the overheating of lasers. The red laser data presents a high sensibility to the noise, for the developed hypothesis validation must be used a new red laser with a high stability for comparison of the results.

In addiction, the results can be enhanced removing the noise from the camera 'dark current', this is a small current created by the electrical noise in the photodetector device when there are not light in the room. To correct this one, a image without light is acquired during a certain time, a minute, for example. To remove the 'dark current', this image is subtracted to the all speckle video frames. During acquisitions the camera warm up, changing its photons sensibility, so the use of a camera thermal stabilizer is a correct solution.

The other point is the comparison of these results when is used this syringe pump and an other one. There are some variations of curves that occurs for all velocities, this can to represent some variability in syringe pump sensitivity.

The main goal is to acquire the velocities and to compare with the real velocity of the syringe pump, to describe the relation between them. However, this only can be performed when the video speckle acquisitions are good. In the next step, will be tested the lasers incidence angles and the different depths. For this purpose will be placed, upon the phantom, material with stationary dispersers, like agar-agar gel. The thickness of the material will be changed as well as the slope, to create different incident angles.

Appendices

Appendix A
Microcirculation Test #3

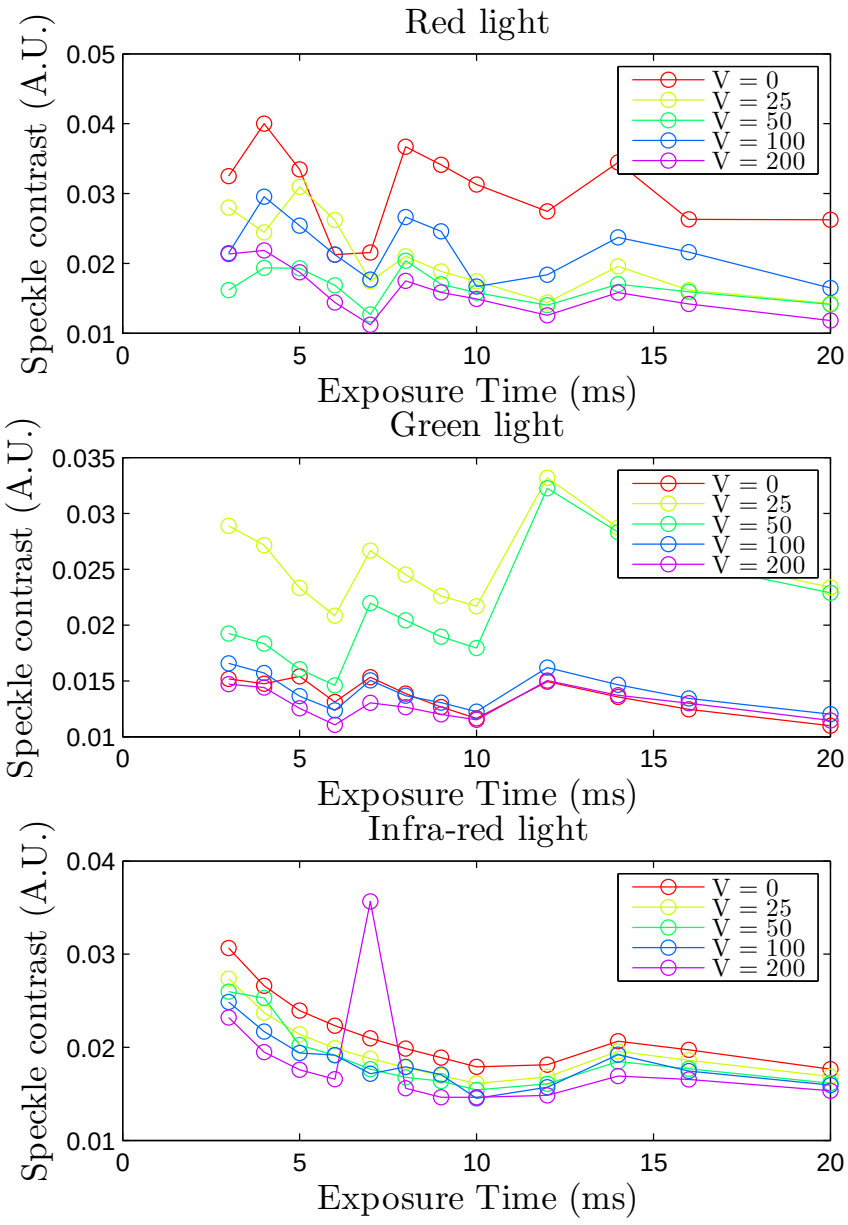

Figure A.1: Contrast (K) by Exposure Times (T). Contrast was computed using sLSCI with a window size of 5 x 5 pixels.

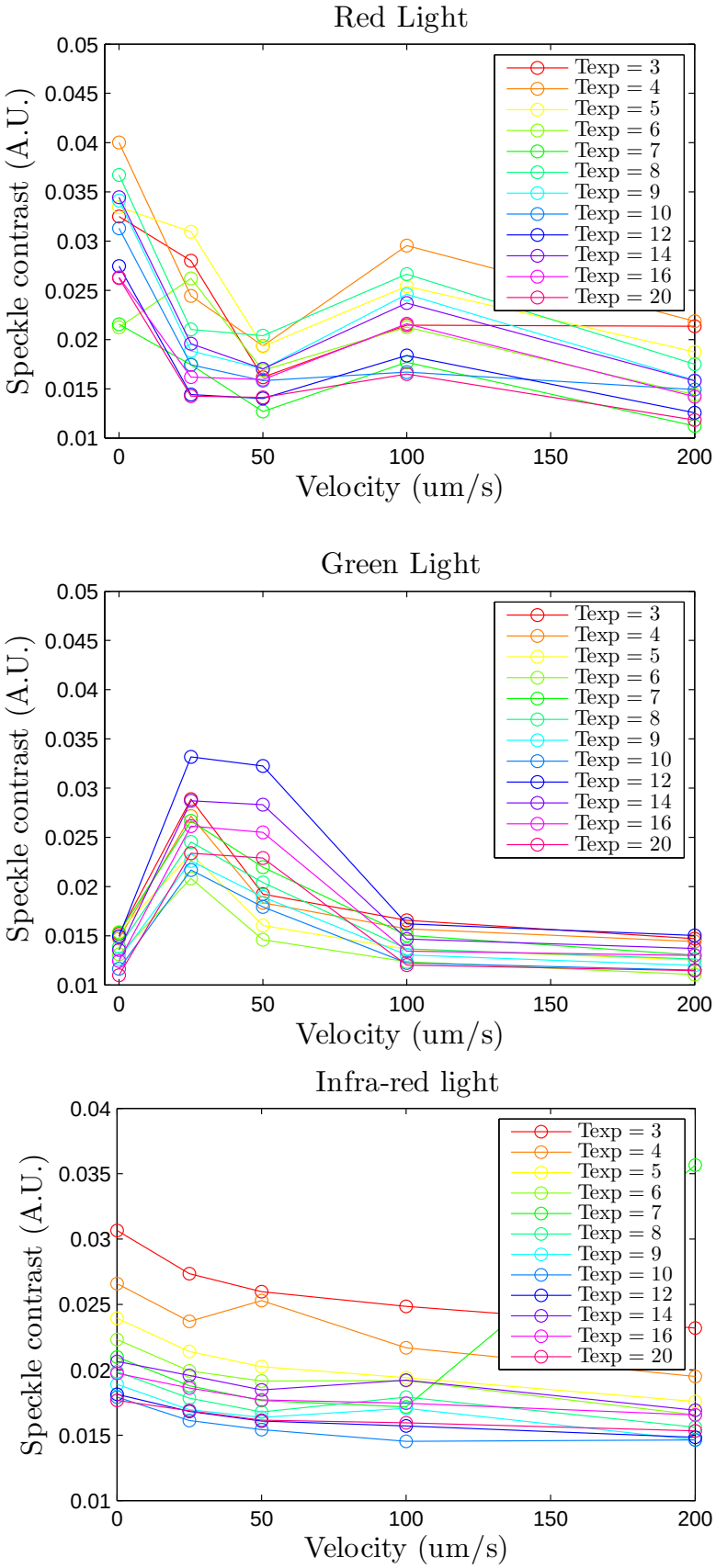

Figure A.2: Contrast (K) by Exposure Times (V). Contrast was computed using sLSCI with a window size of 5 x 5 pixels.

Appendix B
Microcirculation Test #4

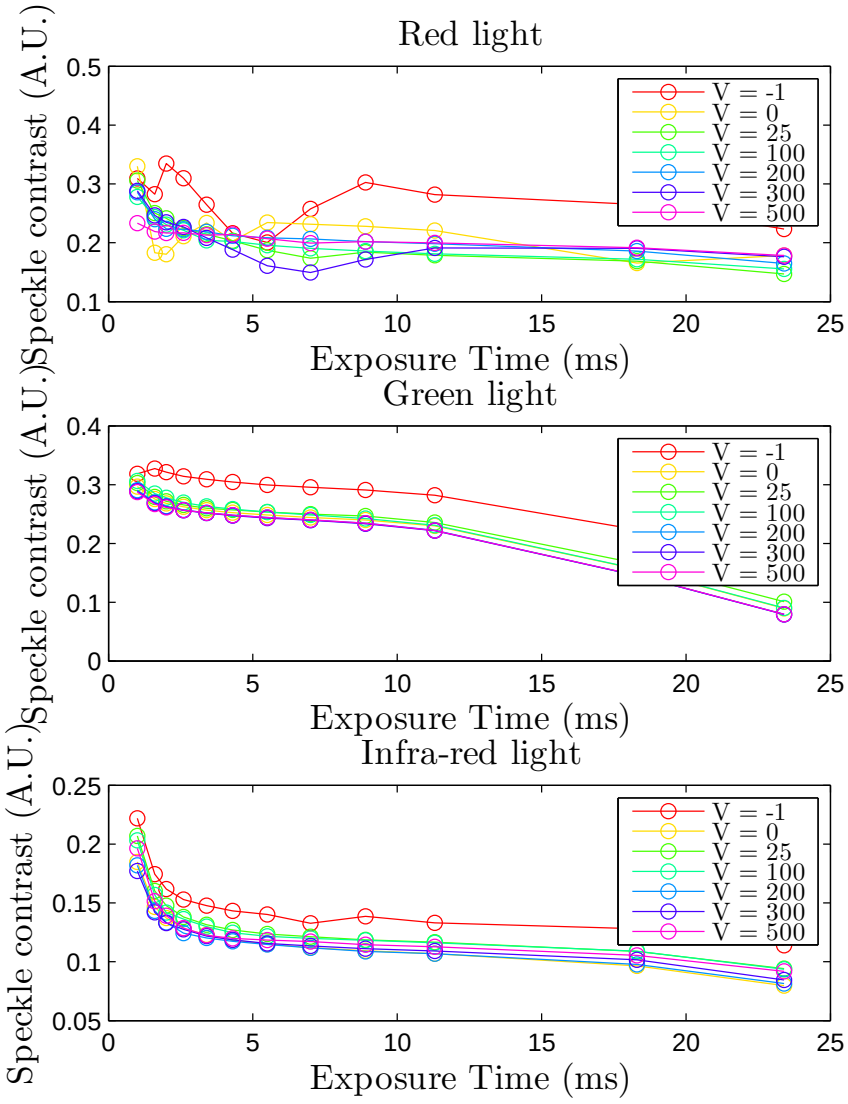

Figure B.1: Contrast (K) by Exposure Times (T). Contrast was computed using sLSCI with a window size of 3 x 3 pixels.

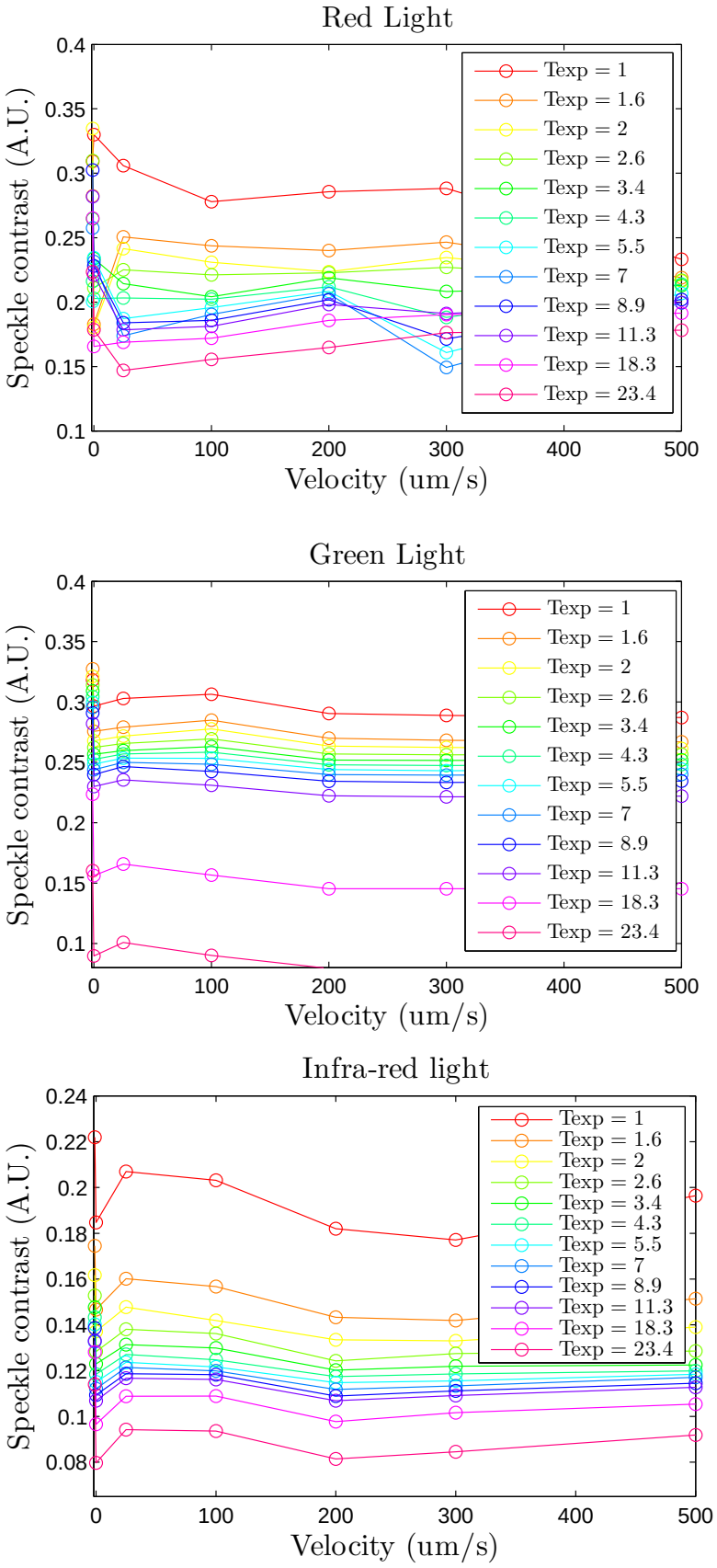

Figure B.2: Contrast (K) by Exposure Times (V). Contrast was computed using sLSCI with a window size of 3 x 3 pixels.

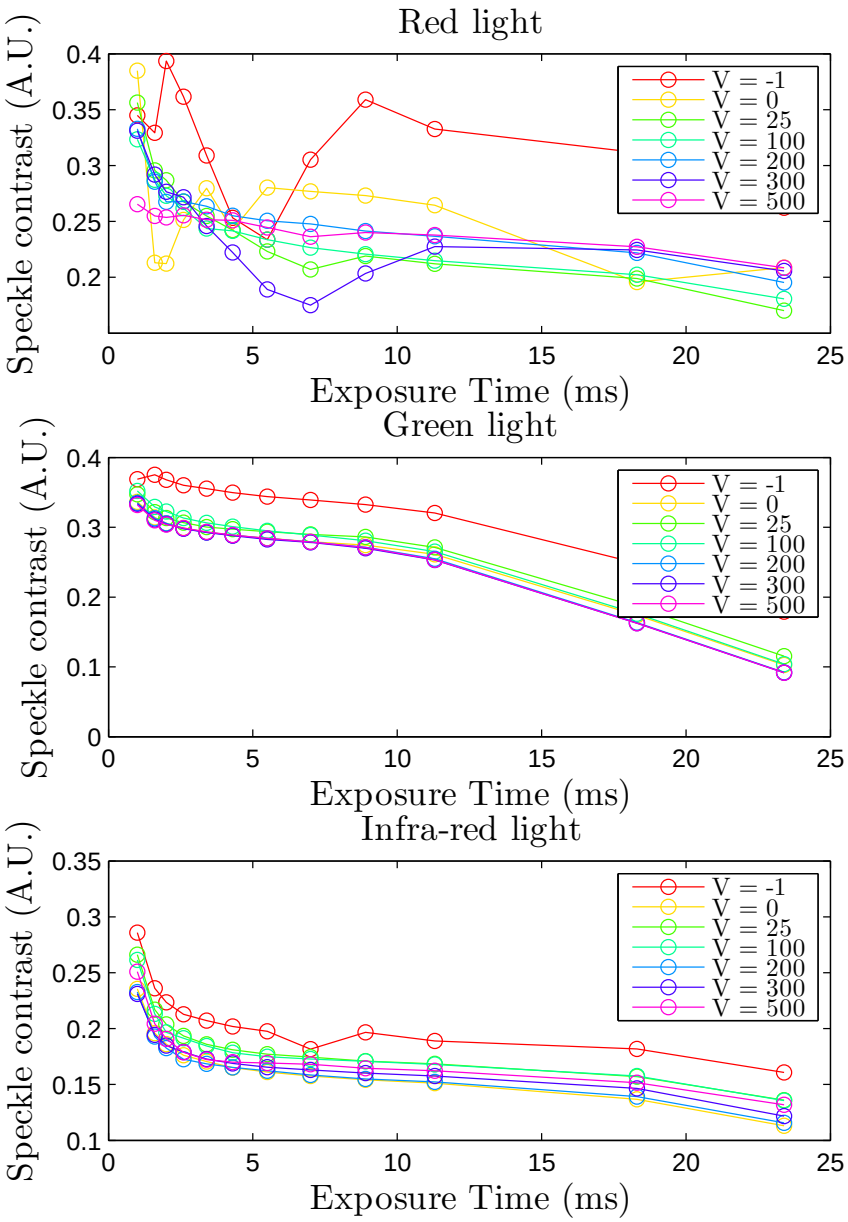

Figure B.3: Contrast (K) by Exposure Times (T). Contrast was computed using sLSCI with a window size of 5 x 5 pixels.

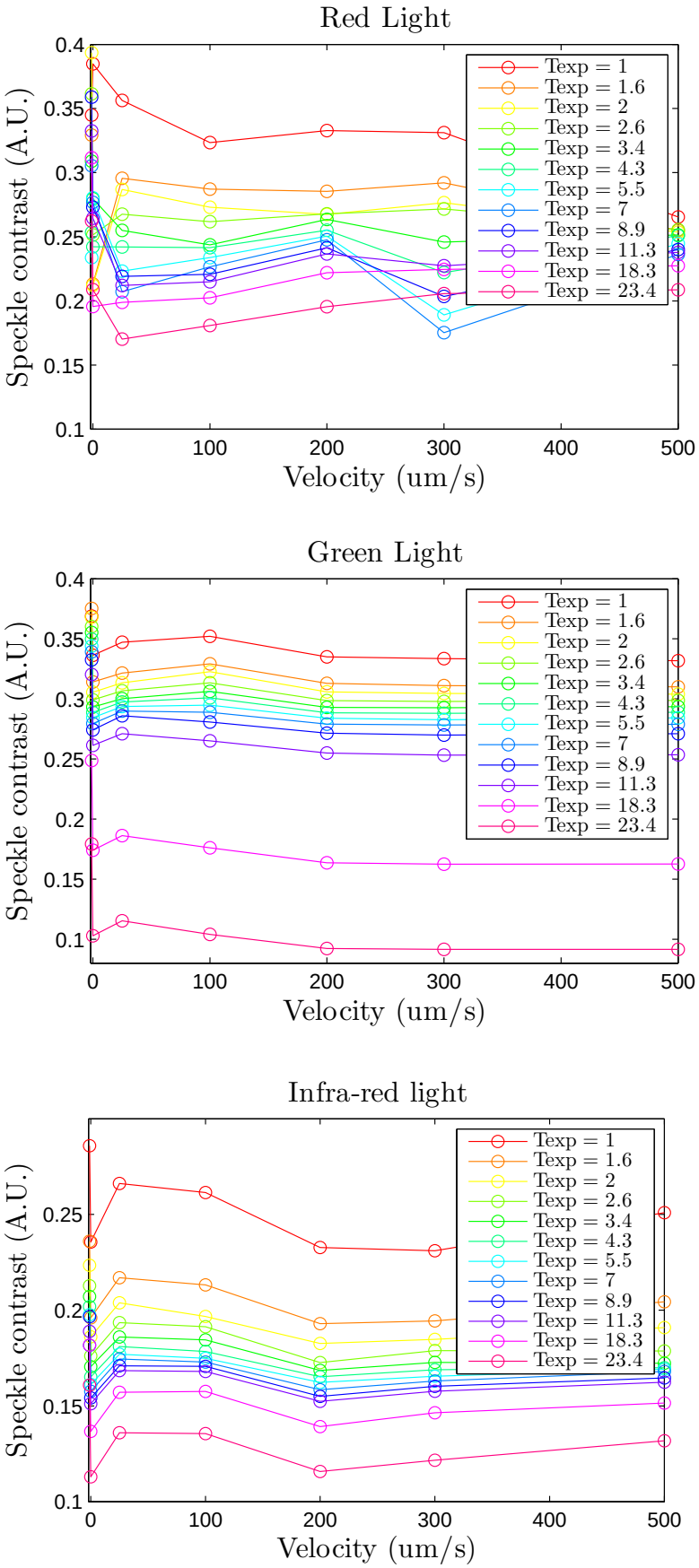

Figure B.4: Contrast (K) by Exposure Times (V). Contrast was computed using sLSCI with a window size of 5 x 5 pixels.

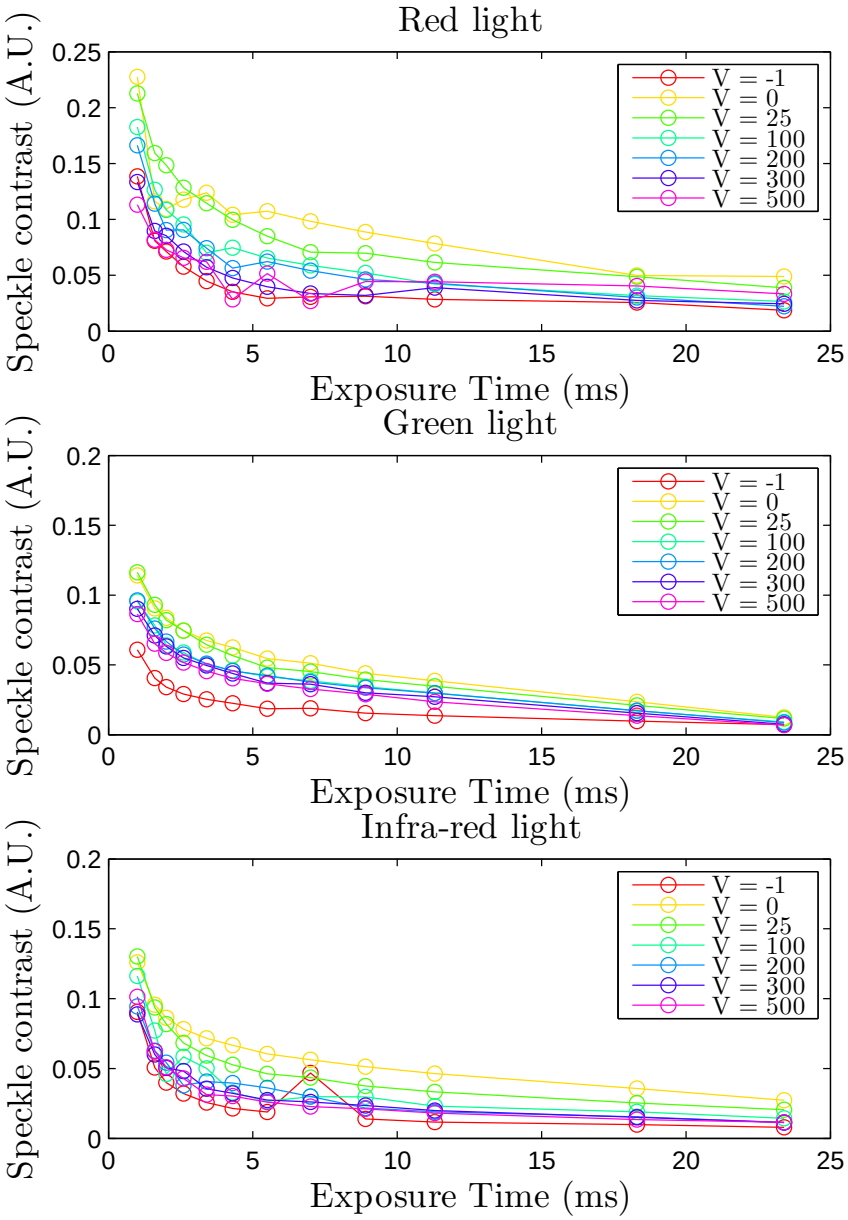

Figure B.5: Contrast (K) by Exposure Times (T). Contrast was computed using tLSCI with a window size of 3 x 3 pixels.

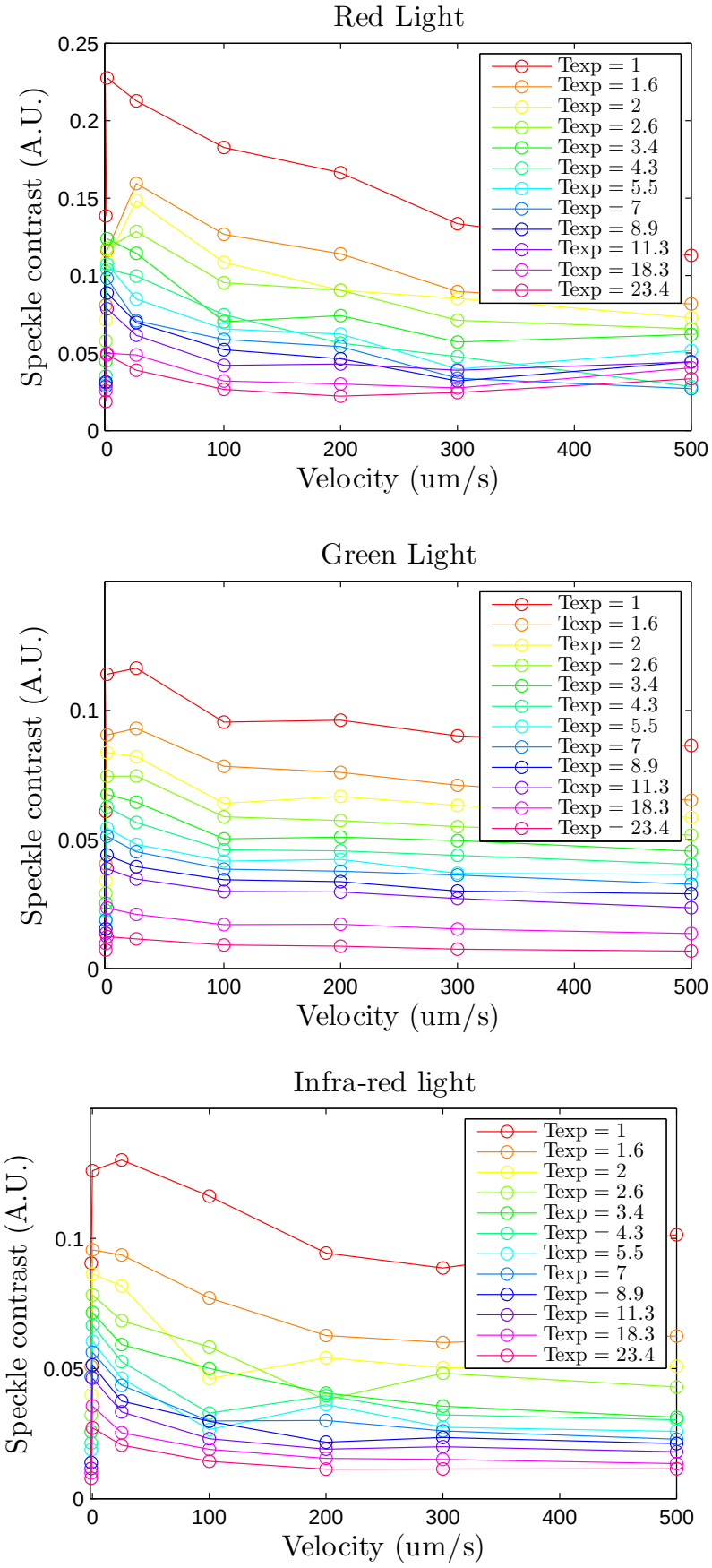

Figure B.6: Contrast (K) by Exposure Times (V). Contrast was computed using tLSCI with a window size of 3 x 3 pixels.

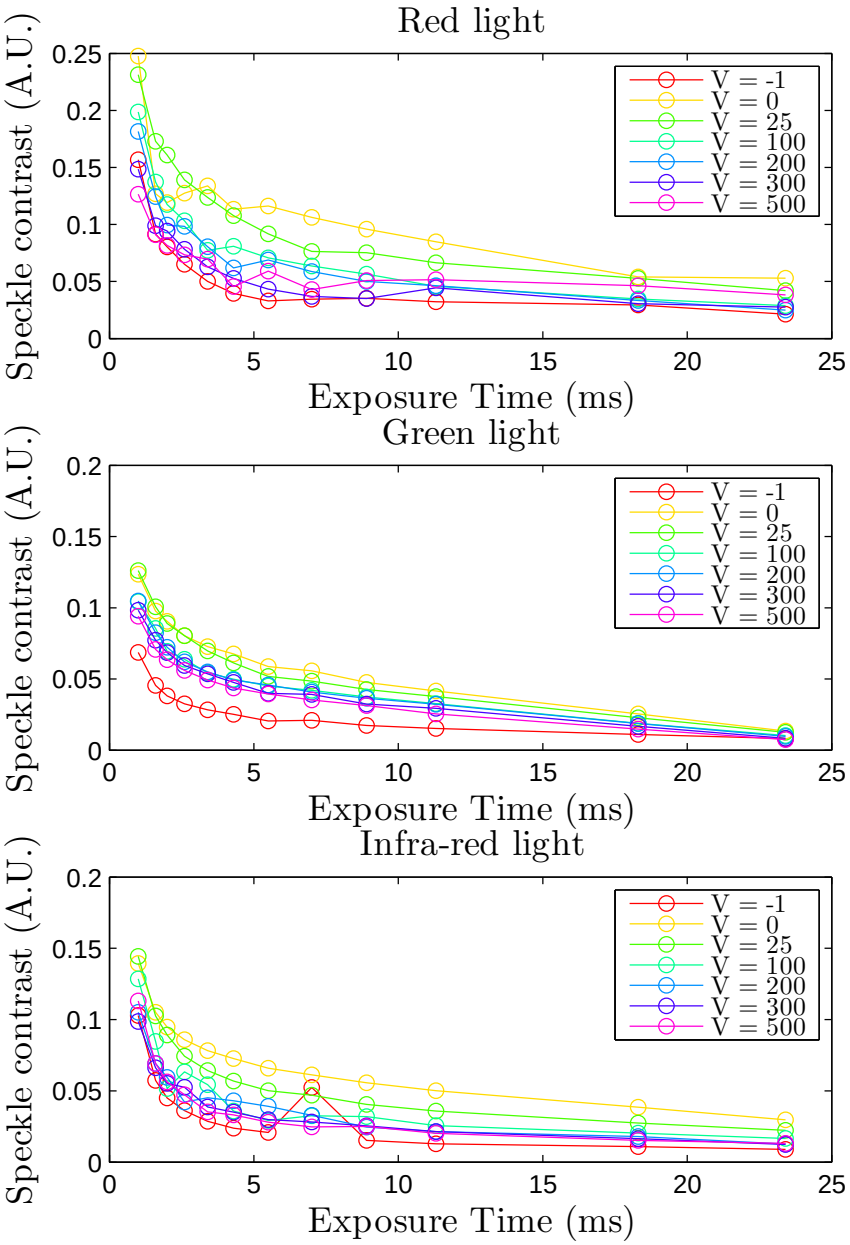

Figure B.7: Contrast (K) by Exposure Times (T). Contrast was computed using tLSCI with a window size of 5 x 5 pixels.

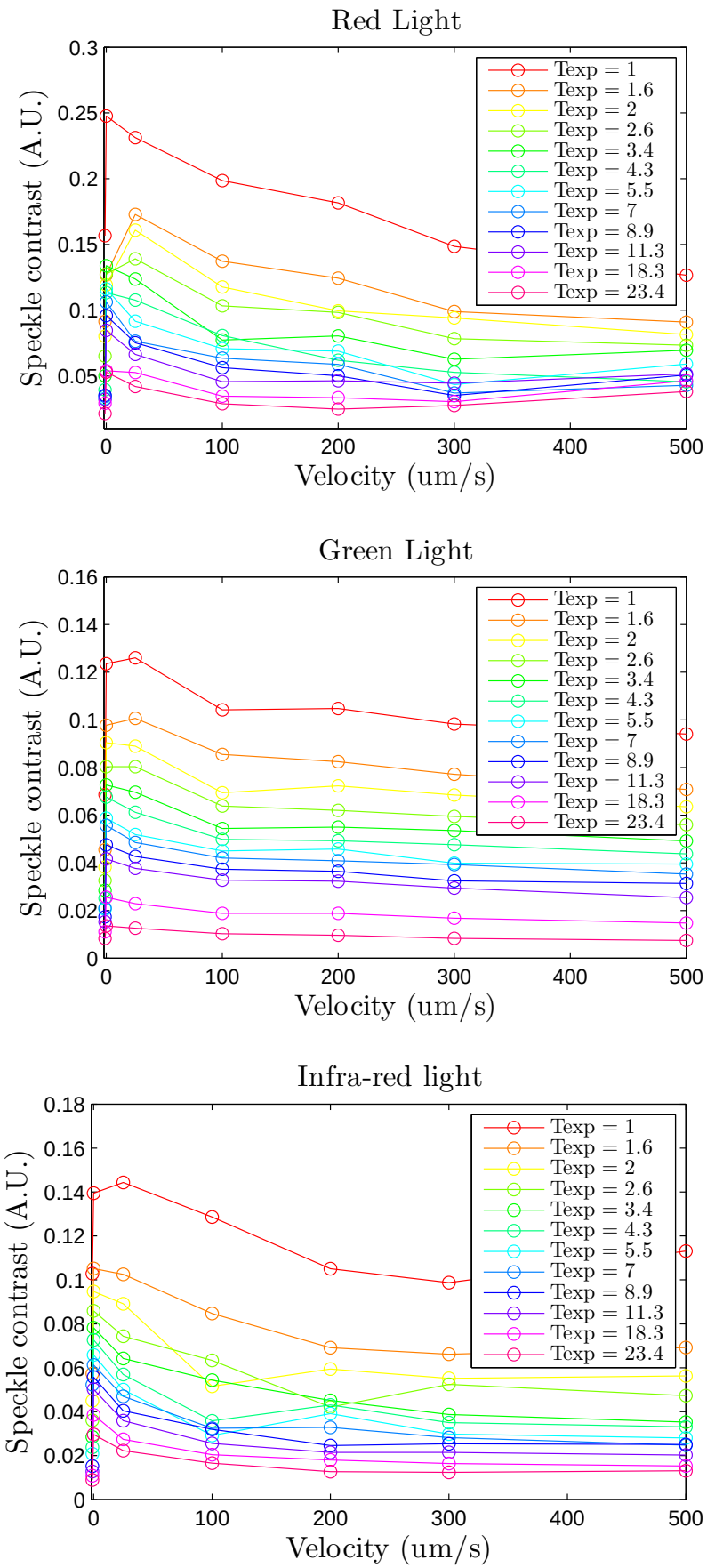

Figure B.8: Contrast (K) by Exposure Times (V). Contrast was computed using tLSCI with a window size of 5 x 5 pixels.

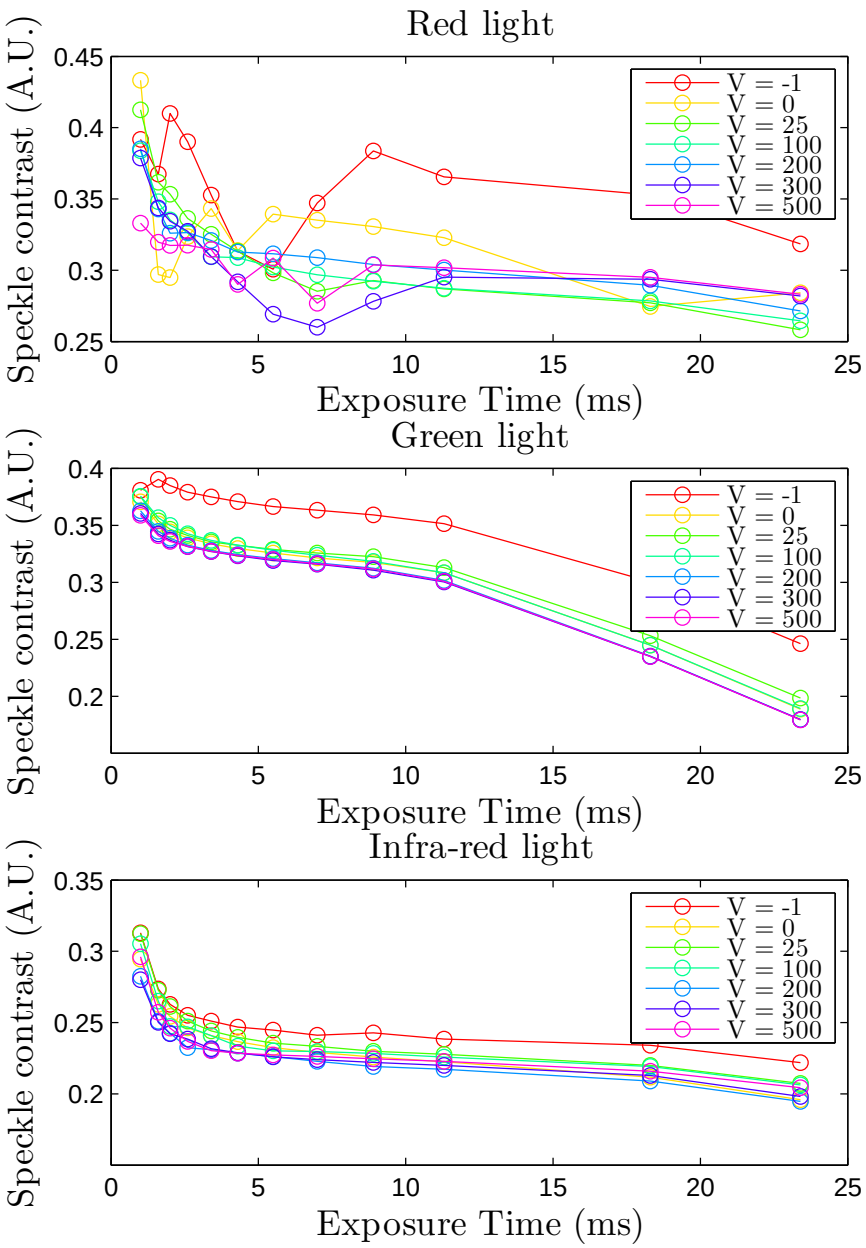

Figure B.9: Contrast (K) by Exposure Times (T). Contrast was computed using stLSCI with a window size of 3 x 3 x 3 pixels.

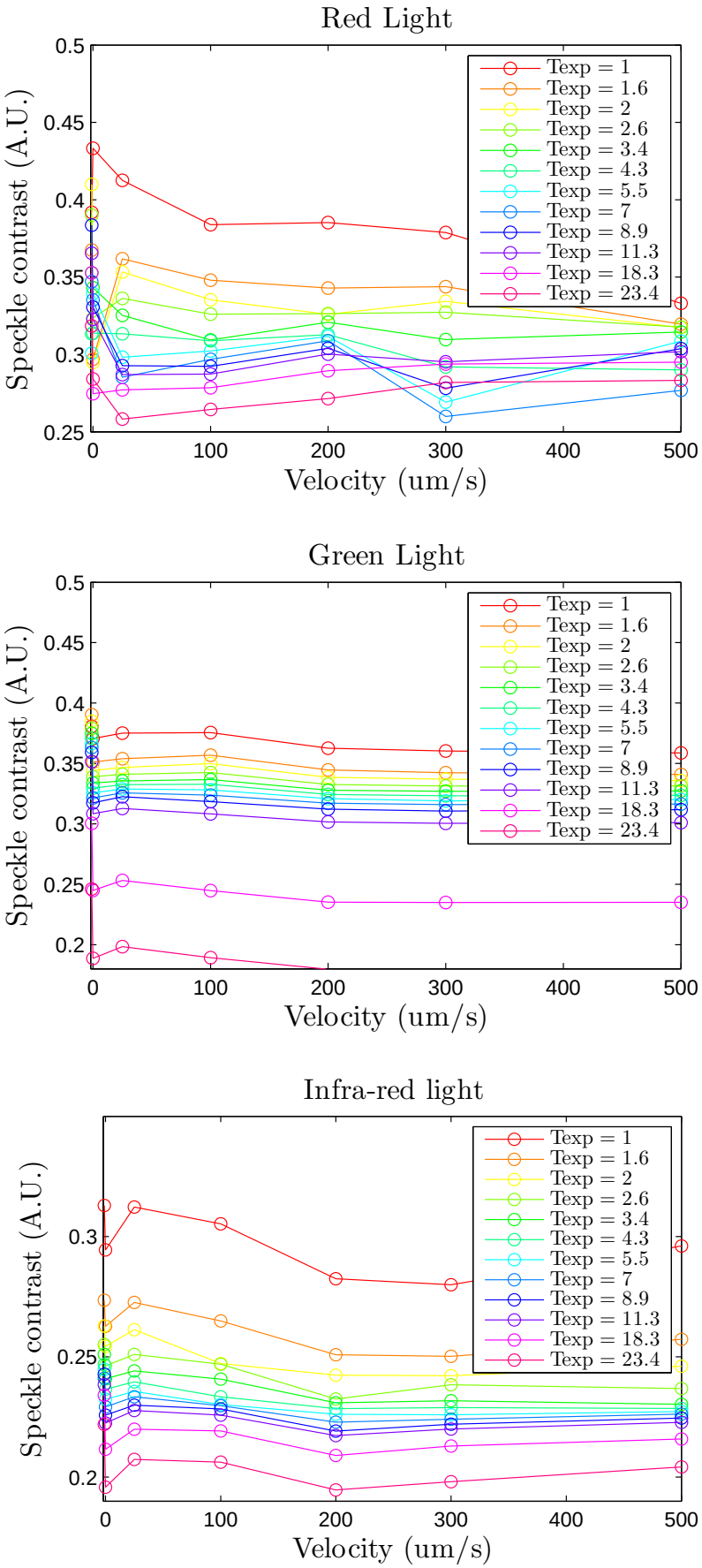

Figure B.10: Contrast (K) by Exposure Times (V). Contrast was computed using stLSCI with a window size of 3 x 3 x 3 pixels.

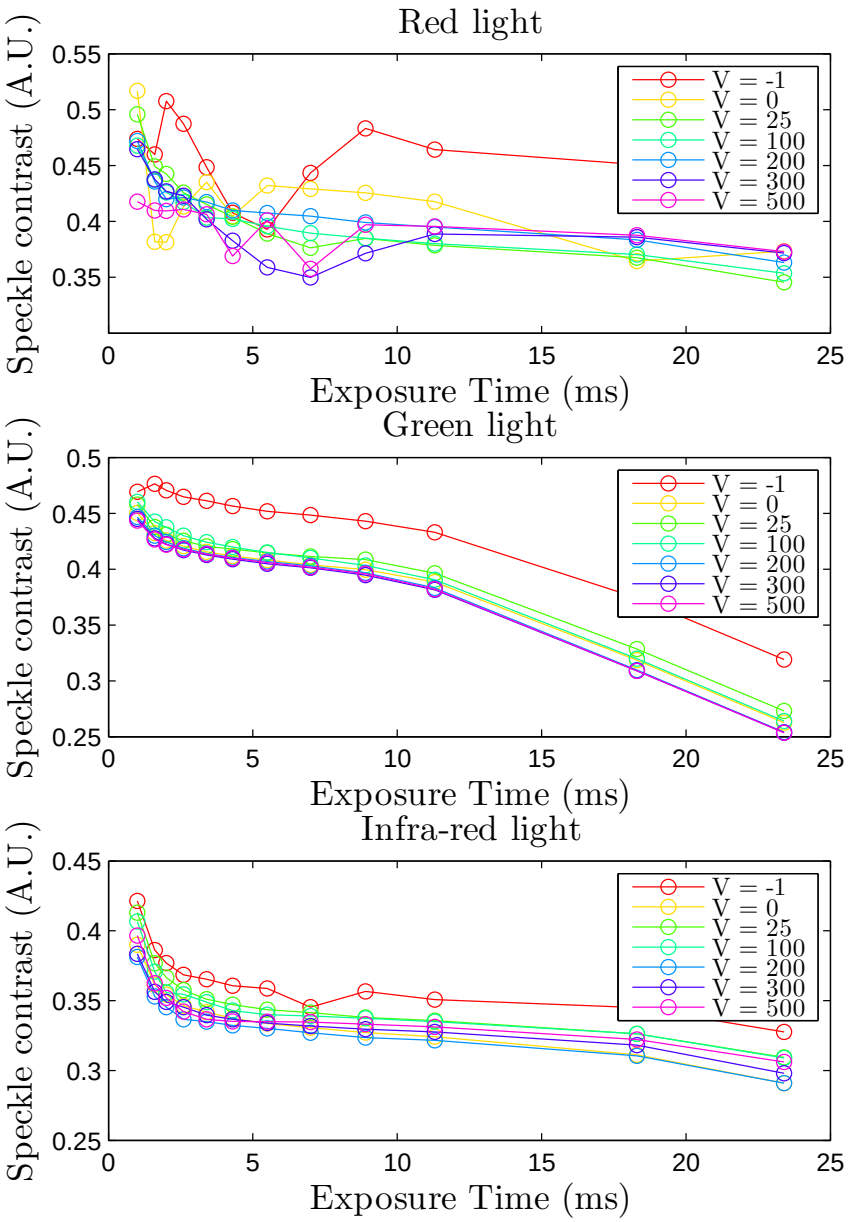

Figure B.11: Contrast (K) by Exposure Times (T). Contrast was computed using stLSCI with a window size of 5 x 5 x 5 pixels.

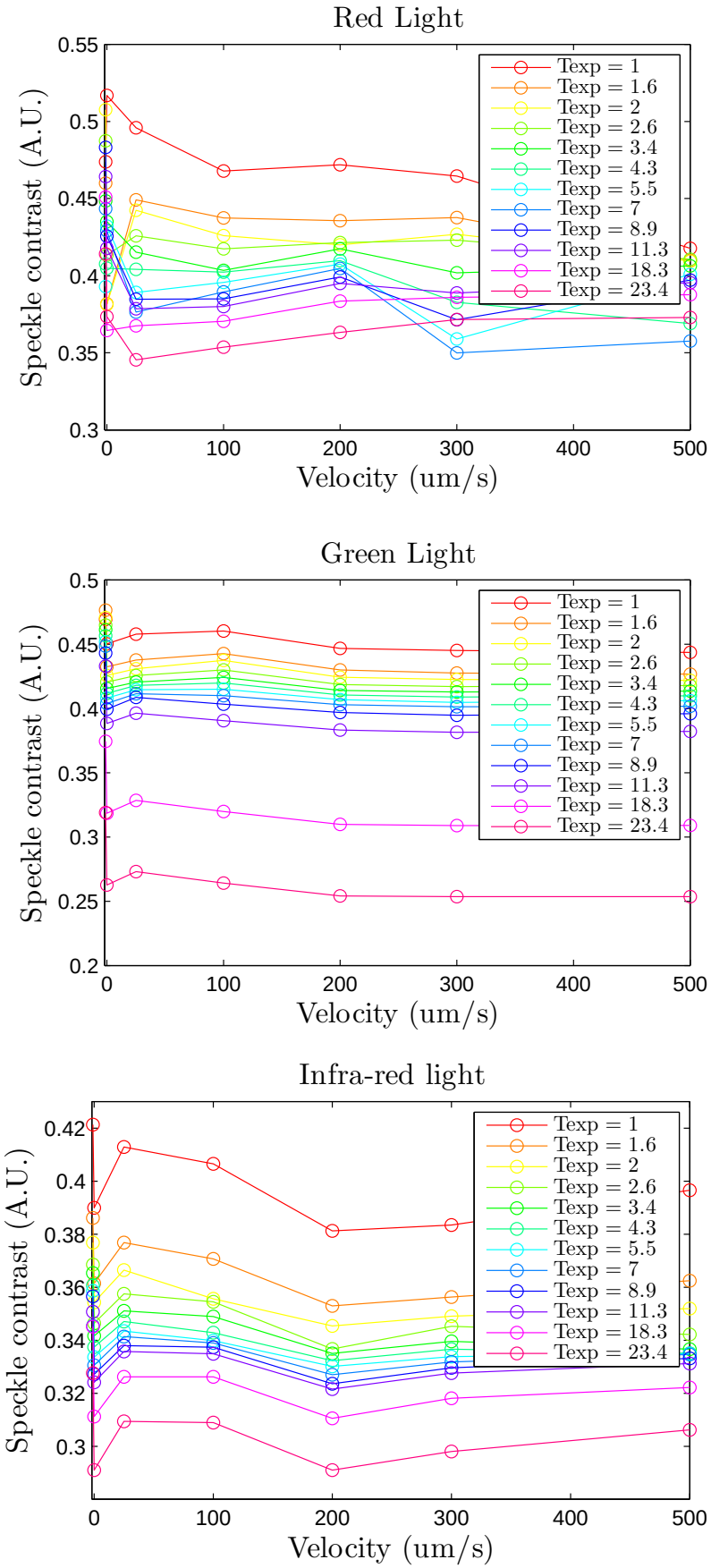

Figure B.12: Contrast (K) by Exposure Times (V). Contrast was computed using stLSCI with a window size of 5 x 5 x 5 pixels.

Bibliography

[1] M. O. Carrageta, "Fundação Portuguesa de Cardiologia," 2014. [Online]. Available: http://www.fpcardiologia.pt/

[2] P. Vaz, "Depth discrimination of microcirculation using laser speckle technique," PnD thesis proposal, University of Coimbra, Coimbra, 2013.

[3] E. Figueiras, "Métodos e instrumentação para fluxometria laser : aplicações à microcirculação sanguínea," Ph.D. dissertation, Universidade de Coimbra, 2012.

[4] T. Pereira, P. Vaz, and T. Oliveira, "Empirical mode decomposition for self-mixing Doppler signals of hemodynamic optical probes." *Physiological measurement*, vol. 34, no. 3, pp. 377–90, Mar. 2013.

[5] J. Júnior, "Sistema para Medição da Velocidade de Células Vermelhas Sanguíneas na Microcirculação Utilizando a Técnica de Correlação Cruzada," MSc dissertation, Rio de Janeiro, 2006.

[6] W. Boron and E. Boulpaep, "Medical Physiology." Ohio: Elsevier, 2009, pp. 800–920.

[7] R. Seeley, T. Stephens, and F. Tate, "Anatomy & fisiology." New York: McGraw-Hill Companies, 2003, pp. 652–763.

[8] G. Tortora and B. Derrickson, "Principles of anatomy and physiology." Hoboken: John Wiley & Sons, 2008, pp. 174–826.

[9] "Circulatory System Part II: Blood Vessels." [Online]. Available: http://www.mhhe.com

[10] J. Prothero and A. Burton, "The physics of blood flow in capillaries. I. The nature of the motion." *Biophysical journal*, vol. 1, no. 2, pp. 565–79, Sep. 1961.

[11] M. Corrêa, "Caracterização das flutuações do sinal laser Doppler do fluxo microvascular," Ph.D. dissertation, Universidade de São Paulo, 2011.

[12] F. Morales, "Improving the clinical applicability of laser Doppler perfusion monitoring," Ph.D. dissertation, University of Groningen, 2005.

[13] A. Murray, R. Gorodkin, and T. Moore, "Comparison of red and green laser doppler imaging of blood flow." *Lasers in surgery and medicine*, vol. 35, no. 3, pp. 191–200, Jan. 2004.

[14] L. Figueiredo, E. Silva, and T. Corrêa, "Macro and micro-circulatory hemodynamics evaluation in sepsis," *Revista de medicina (São Paulo)*, vol. 87, no. 2, pp. 84–91, 2008.

[15] M. Roustit and J. Cracowski, "Non-invasive assessment of skin microvascular function in humans: an insight into methods." *Microcirculation*, vol. 19, no. 1, pp. 47–64, Jan. 2012.

[16] "Diabetes: Facts and Figures," 2013. [Online]. Available: http://www.idf.org/worlddiabetesday/toolkit/gp/facts-figures

[17] D. A. Boas, D. H. Brooks, and E. L. Miller, "Imaging the body with diffuse optical tomography," *Ieee signal processing magazine*, no. November, pp. 57–75, 2001.

[18] P. Öberg, "Optics in Optical sensors in medical care," *Sensors Update*, vol. 13, no. 1, pp. 201–236, 2003.

[19] T. Vo-Dinh, "Biomedical photonics handbook." Tennessee: CRC Press, 2003, pp. 1–40.

[20] D. Lide, *CRC Handbook of Chemestry and Physics*, 84th ed., ser. CRC HANDBOOK OF CHEMISTRY AND PHYSICS. Taylor & Francis, 2003.

[21] V. Almeida, "New methods for hemodynamic evaluation: a multi-parametric approach," Ph.D. dissertation, University of Coimbra, 2013.

[22] V. Almeida, H. Pereira, and T. Pereira, "Piezoelectric probe for pressure waveform estimation in flexible tubes and its application to the cardiovascular system," *Sensors and Actuators A: Physical*, vol. 169, no. 1, pp. 217–226, Sep. 2011.

[23] J. L. Cracowski, F. Gaillard-Bigot, and C. Cracowski, "Skin microdialysis coupled with laser speckle contrast imaging to assess microvascular reactivity." *Microvascular research*, vol. 82, no. 3, pp. 333–8, Nov. 2011.

[24] F. L. Sax, R. O. Cannon, and C. Hanson, "Impaired Forearm Vasodilator Reserve in Patients with Microvascular Angina," *New England Journal of Medicine*, vol. 317, no. 22, pp. 1366–1370, Nov. 1987.

[25] E. Figueiras, V. Loureiro, L. Requicha Ferreira, and A. Humeau, "Some reasons to build a new laser Doppler flowmeter to monitor microvascular blood flow," *IFMBE Proceedings, World Congress on Medical Physics and Biomedical Engineering*, vol. 25/IV, pp. 1865–1868, 2009.

[26] G. Holloway and D. Watkins, "Laser Doppler measurement of cutaneous blood flow," *Journal of Investigative Dermatology*, vol. 69, no. 3, pp. 306–309, 1977.

[27] R. J. Gush, T. a. King, and M. I. Jayson, "Aspects of laser light scattering from skin tissue with application to laser Doppler blood flow measurement." *Physics in medicine and biology*, vol. 29, no. 12, pp. 1463–76, Dec. 1984.

[28] R. Oliveira, S. Semedo, and E. Figueiras, "Laser Doppler flowmeters for microcirculation measurements," *1st Portuguese Meeting in Bioengineering, IEEE EMBS*, pp. 1–4, 2011.

[29] S. M. Monstrey, H. Hoeksema, and R. D. Baker, "Burn wound healing time assessed by laser Doppler imaging. Part 2: validation of a dedicated colour code for image interpretation." *Burns : journal of the International Society for Burn Injuries*, vol. 37, no. 2, pp. 249–56, Mar. 2011.

[30] Perimed, "PeriFlux System 5000 - laser Doppler and transcutaneous oxygen," Sweden. [Online]. Available: http://www.perimed-instruments.com/products/instruments/laser-doppler-monitors/periflux-system-5000

[31] DTI, "OxyLab LDF and OxyFlo." [Online]. Available: http://www.dti-biotech.com/ProductBlood.htm

[32] V. v. Erný, Z. Turek, and R. P. A. . Ízková, "Orthogonal Polarization Spectral Imaging," *Physiological Research*, vol. 56, pp. 141–147, 2007.

[33] O. Genzel-Boroviczény, J. Strötgen, and A. G. Harris, "Orthogonal polarization spectral imaging (OPS): a novel method to measure the microcirculation in term and preterm infants transcutaneously." *Pediatric research*, vol. 51, no. 3, pp. 386–91, Mar. 2002.

[34] J. D. Briers, "Laser Doppler, speckle and related techniques for blood perfusion mapping and imaging." *Physiological measurement*, vol. 22, no. 4, pp. R35–66, Nov. 2001.

[35] A. B. Parthasarathy, W. J. Tom, and A. Gopal, "Robust flow measurement with multi-exposure speckle imaging." *Optics express*, vol. 16, no. 3, pp. 1975–89, Feb. 2008.

[36] A. Ponticorvo and A. K. Dunn, "How to build a Laser Speckle Contrast Imaging (LSCI) system to monitor blood flow." *Journal of visualized experiments : JoVE*, no. 45, pp. 2–4, Jan. 2010.

[37] G. Mahé, P. Rousseau, and S. Durand, "Laser speckle contrast imaging accurately measures blood flow over moving skin surfaces." *Microvascular research*, vol. 81, no. 2, pp. 183–8, Mar. 2011.

[38] R. Bi, J. Dong, and K. Lee, "Deep tissue flowmetry based on diffuse speckle contrast analysis." *Optics letters*, vol. 38, no. 9, pp. 1401–3, May 2013.

[39] O. Thompson, M. Andrews, and E. Hirst, "Correction for spatial averaging in laser speckle contrast analysis." *Biomedical optics express*, vol. 2, no. 4, pp. 1021–9, Jan. 2011.

[40] J. Briers and S. Webster, "Laser speckle contrast analysis (LASCA): a nonscanning, full-field technique for monitoring capillary blood flow," *Journal of biomedical optics*, vol. 1, no. 2, pp. 174–179, 1996.

[41] K. Basak, M. Manjunatha, and P. K. Dutta, "Review of laser speckle-based analysis in medical imaging." *Medical & biological engineering & computing*, vol. 50, no. 6, pp. 547–58, Jun. 2012.

[42] M. Draijer, E. Hondebrink, and T. van Leeuwen, "Review of laser speckle contrast techniques for visualizing tissue perfusion." *Lasers in medical science*, vol. 24, no. 4, pp. 639–651, Jul. 2009.

[43] J. Goodman, "Statistical properties of laser speckle patterns," in *Laser speckle and related phenomena*, 1st ed., J. Dainty, Ed. Berlin: Roberts and Company Publishers, 1975, ch. 2, pp. 9–74.

[44] M. D. Stern, D. L. Lappe, and P. D. Bowen, "Continuous measurement of tissue blood flow by laser-Doppler spectroscopy." *The American journal of physiology*, vol. 232, no. 4, pp. H441–8, Apr. 1977.

[45] G. N. Golpayegani and K. Maghooli, "Laser Doppler and Laser Speckle Techniques for Blood Flow Measurement," in *Bioinformatics and Biomedical Engineering, 2008. ICBBE 2008.*, Tehran, 2008, pp. 1555–1560.

[46] J. Briers and A. Fercher, "Retinal blood-flow visualization by means of laser speckle photography." *Investigative ophthalmology & visual science*, vol. 22, no. 2, pp. 255–259, 1982.

[47] J. D. Briers and S. Webster, "Quasi real-time digital version of single-exposure speckle photography for full-field monitoring of velocity or flow fields," vol. 116, no. April, 1995.

[48] D. a. Boas and A. K. Dunn, "Laser speckle contrast imaging in biomedical optics." *Journal of biomedical optics*, vol. 15, no. 1, p. 011109, 2010.

[49] D. Briers, D. Duncan, and E. Hirst, "Laser speckle contrast imaging: theoretical and practical limitations," *Journal of biomedical optics*, vol. 18, no. 6, pp. 1–9, 2013.

[50] Y. Tamaki, M. Araie, and E. Kawamoto, "Noncontact, two-dimensional measurement of retinal microcirculation using laser speckle phenomenon." *Investigative ophthalmology & visual science*, vol. 35, no. 11, pp. 3825–34, Oct. 1994.

[51] S. Yuan, A. Devor, and D. A. Boas, "Determination of optimal exposure time for contrast imaging," *Applied optics*, vol. 44, no. 10, pp. 1823–1830, 2005.

[52] J. D. Pauling, J. a. Shipley, and S. Raper, "Comparison of infrared thermography and laser speckle contrast imaging for the dynamic assessment of digital microvascular function." *Microvascular research*, vol. 83, no. 2, pp. 162–7, Mar. 2012.

[53] K. R. Forrester, C. Stewart, and J. Tulip, "Comparison of laser speckle and laser Doppler perfusion imaging: measurement in human skin and rabbit articular tissue." *Medical & biological engineering & computing*, vol. 40, no. 6, pp. 687–97, Nov. 2002.

[54] K. R. Forrester, J. Tulip, and C. Leonard, "A Laser Speckle Imaging Technique for Measuring Tissue Perfusion," vol. 51, no. 11, pp. 2074–2084, 2004.

[55] M. J. Leahy, J. G. Enfield, and N. T. Clancy, "Biophotonic methods in microcirculation imaging," *Medical Laser Application*, vol. 22, no. 2, pp. 105–126, Oct. 2007.

[56] A. Nadort, R. G. Woolthuis, and T. G. van Leeuwen, "Quantitative laser speckle flowmetry of the in vivo microcirculation using sidestream dark field microscopy." *Biomedical optics express*, vol. 4, no. 11, pp. 2347–61, Jan. 2013.

[57] D. D. Duncan, S. J. Kirkpatrick, and J. C. Gladish, "What is the proper statistical model for laser speckle flowmetry?" *Complex Dynamics and Fluctuations in Biomedical Photonics V. Proc. SPIE*, vol. 6855, no. 2, pp. 685 502–685 502–7, Feb. 2008.

[58] D. D. Duncan and S. J. Kirkpatrick, "Can laser speckle flowmtry be made a quantitative tool?" *NIH Public Access*, vol. 25, no. 8, pp. 2088–2094, 2008.

[59] J. ODoherty, P. McNamara, and N. T. Clancy, "Comparison of instruments for investigation of microcirculatory blood flow and red blood cell concentration," *Journal of Biomedical Optics*, vol. 14, no. 3, pp. 34 013–34 025, 2009.

[60] D. He, H. C. Nguyen, and B. R. Hayes-Gill, "64x64 pixel smart sensor array for laser Doppler blood flow imaging." *Optics letters*, vol. 37, no. 15, pp. 3060–2, Aug. 2012.

[61] P. Miao, A. Rege, and N. Li, "High resolution cerebral blood flow imaging by registered laser speckle contrast analysis." *IEEE transactions on bio-medical engineering*, vol. 57, no. 5, pp. 1152–7, May 2010.

[62] T. Smausz, D. Zölei, and B. Hopp, "Real correlation time measurement in laser speckle contrast analysis using wide exposure time range images." *Applied optics*, vol. 48, no. 8, pp. 1425–9, Mar. 2009.

[63] R. Balamurugan and S. Muruganand, "Digital Image Processing Technique in Laser Speckle Pattern Interferometer for Phase Evaluation," *International Journal of Engineering and Advance Technology*, vol. 2, no. 3, pp. 560–562, 2013.

[64] J. Senarathna, A. Rege, and N. Li, "Laser Speckle Contrast Imaging: theory, instrumentation and applications." *IEEE reviews in biomedical engineering*, vol. 6, pp. 99–110, Jan. 2013.

[65] G. Mahé, A. Humeau-Heurtier, and S. Durand, "Assessment of skin microvascular function and dysfunction with laser speckle contrast imaging." *Circulation. Cardiovascular imaging*, vol. 5, no. 1, pp. 155–63, Jan. 2012.

[66] C. Millet, M. Roustit, and S. Blaise, "Comparison between laser speckle contrast imaging and laser Doppler imaging to assess skin blood flow in humans." *Microvascular research*, vol. 82, no. 2, pp. 147–51, Sep. 2011.

[67] A. Humeau-Heurtier, E. Guerreschi, and P. Abraham, "Relevance of laser Doppler and laser speckle techniques for assessing vascular function: state of the art and future trends." *IEEE transactions on bio-medical engineering*, vol. 60, no. 3, pp. 659–66, Mar. 2013.

[68] A. K. Dunn, H. Bolay, and M. A. Moskowitz, "Dynamic imaging of cerebral blood flow using laser speckle." *Journal of cerebral blood flow and metabolism : official journal of the International Society of Cerebral Blood Flow and Metabolism*, vol. 21, no. 3, pp. 195–201, Mar. 2001.

[69] A. K. Dunn, "Laser speckle contrast imaging of cerebral blood flow." *Annals of biomedical engineering*, vol. 40, no. 2, pp. 367–77, Feb. 2012.

[70] N. Konishi, Y. Tokimoto, and K. Kohra, "New Laser Speckle Flowgraphy System Using CCD Camera," *Optical Review*, vol. 9, no. 4, pp. 163–169, 2002.

[71] "Laser Safety Handbook," Office for Research Safety, Northwestern Universit, 2011.

[72] Razel Scientific Instruments, "Variable Speed Syringe Pumps Model R99-E." [Online]. Available: http://www.razelscientific.com/products-page/variable-speed-syringe-pumps/model-r99-e/

[73] "Razel Syringe Pumps," *Medlines*, no. 9, pp. 7–11, 2009.

[74] R. Tatam, T. Charrett, and L. Waugh, "Speckle velocimetry for high accuracy odometry for a Mars exploration rover," *Measurement Science and Technology*, vol. 21, no. 2, p. 25301, 2010.